

**CLOTHING FLAMMABILITY AND
SKIN BURN INJURY IN
NORMAL AND MICRO-GRAVITY**

A Thesis Submitted to the College of
Graduate Studies and Research
in Partial Fulfillment of the Requirements
for the Degree of Master of Science
in the Department of Mechanical Engineering
University of Saskatchewan
Saskatoon

By

Jane M. Cavanagh

© Copyright Jane Cavanagh, August 2004. All rights reserved.

PERMISSION TO USE

In presenting this thesis in partial fulfilment of the requirements for a Postgraduate degree from the University of Saskatchewan, I agree that the Libraries of this University may make it freely available for inspection. I further agree that permission for copying of this thesis in any manner, in whole or in part, for scholarly purposes may be granted by the professor or professors who supervised my thesis work or, in their absence, by the Head of the Department or the Dean of the College in which my thesis work was done. It is understood that any copying or publication or use of this thesis or parts thereof for financial gain shall not be allowed without my written permission. It is also understood that due recognition shall be given to me and to the University of Saskatchewan in any scholarly use which may be made of any material in my thesis.

Requests for permission to copy or to make other use of material in this thesis in whole or part should be addressed to:

Head of the Department of Mechanical Engineering
University of Saskatchewan
Saskatoon, Saskatchewan S7N 5A9

ABSTRACT

As space exploration has advanced, time spent in space has increased. With the building of the International Space Station and plans for exploration missions to the Moon and Mars, astronauts will be staying in space for longer periods of time. With these increased stays in space comes an increase in fire safety concerns. One area of fire safety interest is flammability. While current flammability test procedures are in place, they are all performed on the ground and may not be representative of flammability in microgravity. In addition to this, limited research into the severity of skin burn injury in a microgravity environment has been performed.

An apparatus was designed to be flown on a low gravity parabolic aircraft flight to assess the flammability of cotton and 50% cotton/50% polyester fabrics and the resulting skin burn injury that would occur if these fabrics were to ignite. The apparatus, modelled after a Canadian General Standards Board standard flammability test, was also used on the ground for experiments in 1-g. Variables examined in the tests include gravity level, fabric type, air gap size, oxygen concentration, apparatus orientation, ignition source, and method used to secure the specimen. Flame spread rates, heat fluxes, and skin burn predictions determined from test results were compared.

Results from test in 1-g indicated that the orientation of the apparatus had a large effect on flame spread rate, heat flux and predicted skin burn times. Flame spread rates and heat fluxes were highest when the fabric was held in the vertical orientation, which resulted in the lowest predicted times to produce skin burns. Flame spread rates and heat fluxes were considerably lower in microgravity than in 1-g, which resulted in higher predicted times to produce skin burns.

ACKNOWLEDGEMENTS

The author wishes to acknowledge the following for their help in the preparation of this thesis:

- Dr. D.A. Torvi for his supervision of this research and Dr. K.S. Gabriel for added support.
- Dr. C.J. Simonson and Dr. J.D. Bugg for their guidance as members of the supervisory committee.
- Dr. G.A. Ruff of NASA Glenn Research Center for providing the opportunity to fly this project, as well as conducting the flight tests with Heather Fantozzi.
- The Department of Mechanical Engineering at the University of Saskatchewan, Zonta International Foundation and the Canadian Space Agency for funding.
- The U of S Engineering Shops for manufacturing the test apparatus.
- Faculty and staff at the U of S Department of Mechanical Engineering for their friendliness and assistance, especially Dave Deutscher whose lab I made smell like burning an awful lot.
- Dr. J.D. Dale, Mark Ackerman, Dr. E.M. Crown, Helena Perkins and Lelia Lawson for making my time spent at the University of Alberta both useful and enjoyable.
- Tony, Peter, Ryan and Todd for making the office a fun place to be, especially on potluck Wednesdays.
- My friends for telling people I'm a rocket scientist – they make me laugh.
- My parents, for their unconditional love and support throughout my entire life.
- Mom and Dad for the trip to Australia and my siblings who kept me entertained while there, namely Ruth who was my laptop partner for much of this writing.

TABLE OF CONTENTS

ABSTRACT	ii
ACKNOWLEDGEMENTS	iii
TABLE OF CONTENTS	iv
LIST OF TABLES	ix
LIST OF FIGURES	x
NOMENCLATURE	xvii
CHAPTER 1 INTRODUCTION	1
1.1 Flammability and Thermal Protection Tests.....	3
1.1.1 Flammability Tests.....	3
1.1.2 Thermal Protection Tests.....	6
1.2 Skin Burn Predictions.....	9
1.2.1 The Structure of Skin	9
1.2.2 Skin Burn Classification.....	10
1.2.3 Stoll Second Degree Burn Criterion	11
1.2.4 Henriques' Burn Integral.....	13
1.3 Heat Flux Sensors.....	14
1.3.1 Copper Disk Calorimeter.....	15
1.3.2 Skin Simulants	15
1.4 Microgravity Fire Safety Research.....	16
1.4.1 Material Testing for the Shuttle and ISS	16
1.4.2 Flame Spread over Thin Solid Fuels in Low Gravity	17

1.4.3 Test Development for Flammability in Microgravity.....	19
1.4.4 Microgravity Research Environments.....	21
1.5 The Spacecraft Fire Safety Facility Test Rig.....	23
1.6 Cotton Flammability and Skin Burn Injury Experiments.....	23
1.7 Scope of Research.....	24
1.8 Overview of Thesis.....	25
CHAPTER 2 EXPERIMENTAL APPARATUS	26
2.1 Spacecraft Fire Safety Facility.....	26
2.1.1 Combustion Chamber.....	26
2.1.2 Sample Holders.....	27
2.1.3 Flow System.....	28
2.1.4 Imaging System.....	29
2.1.5 Data Acquisition System.....	30
2.2 Design of the Sample Holder.....	30
2.2.1 Sample Card.....	31
2.2.2 Specimen Holder.....	33
2.2.3 Heat Flux Gauges.....	34
2.2.4 Sensor Board.....	36
2.2.5 Spacers.....	39
2.2.6 Hot Wire Ignition Source.....	40
2.2.7 Assembling the Apparatus.....	41

CHAPTER 3 EXPERIMENTAL TEST PROCEDURES	44
3.1 Edmonton Tests.....	44
3.2 Saskatoon Tests.....	50
3.3 Cleveland Tests.....	55
3.4 Houston Tests.....	57
3.5 Summary of Tests Performed.....	61
CHAPTER 4 TREATMENT OF DATA	63
4.1 Flame Spread Rates.....	63
4.1.1 Microgravity Flame Spread Rates.....	66
4.2 Heat Fluxes.....	67
4.2.1 Copper Disk Calorimeters.....	67
4.2.2 Skin Simulants.....	69
4.2.3 Effect of Sensor Types.....	70
4.2.4 Issues in Treatment of Data.....	74
4.3 Skin Burn Predictions.....	76
4.3.1 Stoll Second Degree Burn Criterion.....	76
4.3.2 Henriques' Burn Integral.....	78
4.4 Microgravity Heat Fluxes and Skin Burn Injury Times.....	79
CHAPTER 5 RESULTS AND DISCUSSION	83
5.1 Test Fabrics.....	83
5.2 Effects of Changes to Standard Test Apparatus.....	84
5.2.1 Hotwire Ignition vs. Gas Burner Ignition.....	85

5.2.2 Metallic Tape vs. Corner Fastening Pins.....	86
5.3 Observations of Burning Behaviours	88
5.3.1 1-g Burning Behaviour.....	88
5.3.2 Microgravity Burning Behaviour.....	95
5.4 Flame Spread Rates	97
5.4.1 Flame Spread Rates in 1-g.....	97
5.4.2 Flame Spread Rates at Various Angles of Inclination	102
5.4.3 Flame Spread Rates in Microgravity.....	105
5.5 Heat Fluxes	108
5.5.1 1-g Heat Fluxes.....	108
5.5.2 Microgravity Heat Fluxes.....	118
5.6 Predicted Skin Burn Injuries	123
5.6.1 Second Degree Skin Burn Times in 1-g.....	124
5.6.2 Third Degree Skin Burn Times in 1-g.....	129
5.6.3 Second Degree Skin Burn Times in Microgravity.....	131
5.7 Implications on Test Development.....	132
5.8 Summary	134
CHAPTER 6 CONCLUSIONS AND RECOMMENDATIONS	135
6.1 Conclusions	135
6.2 Recommendations	138
REFERENCES	140

APPENDICES	145
APPENDIX A Experimental Procedure for Microgravity Testing	146
APPENDIX B Estimated Heat Flux Calculations	152
APPENDIX C Skin Burn Injury Predictions	160

LIST OF TABLES

TABLE 3.1 Flight Test Matrix	61
TABLE 3.2 Summary of Experiments Conducted	62
TABLE 5.1 Information on Fabrics used for Testing	84
TABLE 5.2 Mass and Thickness of the Test Fabrics as determined by Standard Tests	84
TABLE 5.3 Vertical Flame Spread Times for Pinned and Taped Fabrics	87
TABLE 5.4 Flame Spread Rates at Various Orientations	98
TABLE 5.5 Comparisons of Microgravity and Normal Gravity Flame Spread Rates	107
TABLE 5.6 Maximum Heat Flux Values (kW/m ²) for Each Test Sensor	111
TABLE 5.7 Average Maximum Heat Flux Value for All Fabrics in Various Orientations at 7 mm and 13 mm Air Gaps	112
TABLE 5.8 Estimated Radiation, Conduction and Convection Heat Transfer for Both Air Gaps in All Orientations Based on Four Different Fabric Temperatures	115
TABLE 5.9 Heat Flux Values from the Microgravity Flight Tests	122
TABLE 5.10 Second and Third Degree Burn Times Predicted by Henriques’ Burn Integral for a Constant Heat Flux	124
TABLE 5.11 Microgravity Predicted Skin Burn Injury Times	132
TABLE B.1 Estimated Radiation Heat Flux	153
TABLE B.2 Radiation Heat Flux Estimated for Microgravity	154
TABLE B.3 Estimated Conduction and Convection Heat Transfer	158
TABLE B.4 Critical Air Gap for Transition from Conduction to Convection	159

LIST OF FIGURES

FIGURE 1.1 Various Ignition Techniques for Vertical Standard Flammability Tests	6
FIGURE 1.2 ASTM D4108 Thermal Protective Performance Test Apparatus	8
FIGURE 1.3 Stoll Criterion Time to Second Degree Burn for Various Incident Heat Fluxes on Bare Human Skin	12
FIGURE 2.1 Front View of Sample Card Assembly.....	32
FIGURE 2.2a Specimen Holder	34
FIGURE 2.2b Fabric Specimen on Specimen Holder	34
FIGURE 2.3a Skin Simulant Heat Flux Gauge.....	34
FIGURE 2.3b Copper Disk Heat Flux Gauge.....	34
FIGURE 2.4 Side View of Heat Flux Gauge Mounting Holes in the Sensor Board.....	37
FIGURE 2.5a Front View of Sensor Board	38
FIGURE 2.5b Back View of Sensor Board.....	38
FIGURE 2.5c Schematic Front View of Sensor Board	38
FIGURE 2.6a Sample Card with Spacer.....	42
FIGURE 2.6b Assembled Apparatus Back.....	42
FIGURE 2.7a Mounting Specimen Holder on Sample Card	42
FIGURE 2.7b Assembled Apparatus Front.....	42
FIGURE 2.8 Schematic Side View of the Assembled Experimental Apparatus	43
FIGURE 3.1 Direction of Test Specimens Cut from a Test Sample	46
FIGURE 3.2a CAN/CGSB-4.2 No.27.10 Standard Test Apparatus – Surface Ignition.	47
FIGURE 3.2b CAN/CGSB-4.2 No.27.10 Standard Test Apparatus – Edge Ignition	47
FIGURE 3.3 Schematic of Apparatus used to Measure Flame Spread with a Marker Thread in Edmonton.....	48

FIGURE 3.4 Igniter Wire Attached to Fabric Specimen Prior to Ignition	51
FIGURE 3.5 Heat Flux Gauge and Hot Wire Ignition Locations along the Fabric Specimen Surface	52
FIGURE 3.6 Various Test Orientations for the Experimental Apparatus	54
FIGURE 3.7 Field of View of the Camera on the SFSF.....	57
FIGURE 3.8 The KC-135 Parabolic Flight Trajectory.....	58
FIGURE 4.1 Reference Locations for Flame Spread Rate Measurements in the Vertical and Horizontal Orientations.....	65
FIGURE 4.2 Heat Fluxes Calculated with the Central Difference Approximation and the Five Point Least Linear Squares Approximation	68
FIGURE 4.3 Heat Flux Curves using the Minimum and Maximum Calibrated kpc Values.....	70
FIGURE 4.4 Heat Flux Curves from Two Copper Disk and Two Skin Simulant Sensors for a Horizontal Lightweight Cotton Test at the 7 mm Air Gap	71
FIGURE 4.5 Temperature Curves from Two Copper Disk and Two Skin Simulant Sensors for a Horizontal Lightweight Cotton Test at the 7 mm Air Gap	72
FIGURE 4.6 Constant Heat Flux Curves for the Copper Disk and Skin Simulant Sensors with a 0.1°C Temperature Spike at 10 s and a 0.5°C Temperature Spike at 15 s.....	74
FIGURE 4.7a Copper Disk Heat Flux Data for the Same Test with Data Gathered at Time Steps of 0.18 and 0.54 Seconds	75
FIGURE 4.7b Skin Simulant Heat Flux Data for the Same Test with Data Gathered at Time Steps of 0.18 and 0.54 Seconds	75
FIGURE 4.8 Test Data Being Compared to the Stoll Second Degree Burn Criterion...	77

FIGURE 4.9 Heat Flux Data for Copper Disk #1 and Copper Disk #2 from
Test #1 of Flight #3 – Lightweight Cotton in 25% Oxygen with a
7 mm Air Gap showing Predicted Second Degree Burn Times..... 80

FIGURE 4.10 Heat Flux Measured by a Copper Disk Sensor during the
Microgravity Portion of Test #1 from Flight #3..... 81

FIGURE 5.1 Heat Flux Curves from a Burner and Hotwire Ignition Source Test
for Two Copper Disk Sensors 86

FIGURE 5.2a Vertical Test of the Heavyweight Cotton at a 7 mm Air Gap
17 Seconds after Ignition 90

FIGURE 5.2b Vertical Test of the Heavyweight 50/50 Cotton/Polyester at a 7 mm
Air Gap 10 Seconds after Ignition..... 90

FIGURE 5.3a Horizontal Test of the Lightweight Cotton at a 7 mm Air Gap
76 Seconds after Ignition 91

FIGURE 5.3b Horizontal Test of the Lightweight Cotton at a 13 mm Air Gap
35 Seconds after Ignition 91

FIGURE 5.4a Horizontal Test of the Lightweight 50/50 Cotton/Polyester at a
7 mm Air Gap 28 Seconds after Ignition 92

FIGURE 5.4b Horizontal Test of the Lightweight 50/50 Cotton/Polyester at a
13 mm Air Gap 28 Seconds after Ignition 92

FIGURE 5.5 Flipped Test of the Lightweight Cotton at the 7 mm Air Gap
52 Seconds after Ignition 93

FIGURE 5.6 Various Stages of a Heavyweight Cotton Test in the Flipped
Orientation at the 7 mm Air Gap obtained 42, 95, and 108 Seconds
after Ignition..... 94

FIGURE 5.7a Flipped Test of the Heavyweight 50/50 Cotton/Polyester at a 7 mm Air Gap 26 Seconds after Ignition	95
FIGURE 5.7b Flipped Test of the Heavyweight 50/50 Cotton/Polyester at a 13 mm Air Gap 56 Seconds after Ignition	95
FIGURE 5.8a Flipped Test of the Lightweight 50/50 Cotton/Polyester at a 7 mm Air Gap 44 Seconds after Ignition	95
FIGURE 5.8b Flipped Test of the Lightweight 50/50 Cotton/Polyester at a 13 mm Air Gap 20 Seconds after Ignition	95
FIGURE 5.9 Infrared and Video Camera Views of the Heavyweight Cotton at the 13 mm Air Gap in 25% Oxygen obtained 9, 31 and 41 Seconds after Ignition.....	96
FIGURE 5.10 Flame Spread Rates at Various Angles of Inclination for the Heavyweight Cotton Fabric at a 7 mm Air Gap.....	104
FIGURE 5.11 Microgravity Flame Spread Rates for the Lightweight and Heavyweight Cotton Fabrics at 7 and 13 mm Air Gaps in 21% and 25% Oxygen	106
FIGURE 5.12 Heat Fluxes from All Four Sensors for a Lightweight Cotton Test at the 7 mm Air Gap in the Flipped Orientation.....	109
FIGURE 5.13 Heat Fluxes Measured By Two Copper Disk Heat Flux Sensors for the Lightweight Cotton Fabric with a 7 mm Air Gap in Vertical and Horizontal Orientations	110
FIGURE 5.14a Average Maximum Heat Flux Values for 1-g Tests at Various Orientations for the 7 mm Air Gap.....	117

FIGURE 5.14b Average Maximum Heat Flux Values for 1-g Tests at Various Orientations for the 13 mm Air Gap..... 117

FIGURE 5.15a Heat Flux Curve for the Lightweight Cotton Fabric at the 7 mm Air Gap from the Microgravity Flight Data..... 120

FIGURE 5.15b Microgravity Portion of the Heat Flux Curve for the Lightweight Cotton Fabric at the 7 mm Air Gap from the Microgravity Flight Data ... 120

FIGURE 5.16 Skin Burn Injury Times for the Lightweight Cotton Fabric at the 7 mm Air Gap for Various 1-g Orientations 126

FIGURE 5.17a Average Predicted Second Degree Burn Times for All Fabric Types at the 7 mm Air Gap in the Vertical Orientation in 1-g..... 128

FIGURE 5.17b Average Predicted Second Degree Burn Times for All Fabric Types at the 7 mm Air Gap in the Horizontal Orientation in 1-g 128

FIGURE 5.17c Average Predicted Second Degree Burn Times for All Fabric Types at the 7 mm Air Gap in the Flipped Orientation in 1-g 128

FIGURE 5.18 Predicted Third Degree Skin Burn Injury Times for the Lightweight Cotton at the 7 mm Air Gap for Various Orientations in 1-g 130

FIGURE B.1 Parallel Rectangles 152

FIGURE B.2 Parallel Disks..... 153

FIGURE C.1a Lightweight Cotton Second Degree Burn Times at the 7 mm Air Gap..... 160

FIGURE C.1b Heavyweight Cotton Second Degree Burn Times at the 7 mm Air Gap..... 160

FIGURE C.1c Lightweight Blend Second Degree Burn Times at the 7 mm Air Gap..... 161

FIGURE C.1d Heavyweight Blend Second Degree Burn Times at the 7 mm

Air Gap..... 161

FIGURE C.2a Lightweight Cotton Second Degree Burn Times at the 13 mm

Air Gap..... 161

FIGURE C.2b Heavyweight Cotton Second Degree Burn Times at the 13 mm

Air Gap..... 162

FIGURE C.2c Lightweight Blend Second Degree Burn Times at the 13 mm

Air Gap..... 162

FIGURE C.2d Heavyweight Blend Second Degree Burn Times at the 13 mm

Air Gap..... 162

FIGURE C.3a Lightweight Cotton Third Degree Burn Times at the 7 mm

Air Gap..... 163

FIGURE C.3b Heavyweight Cotton Third Degree Burn Times at the 7 mm

Air Gap..... 163

FIGURE C.3c Lightweight Blend Third Degree Burn Times at the 7 mm

Air Gap..... 163

FIGURE C.3d Heavyweight Blend Third Degree Burn Times at the 7 mm

Air Gap..... 164

FIGURE C.4a Lightweight Cotton Third Degree Burn Times at the 13 mm

Air Gap..... 164

FIGURE C.4b Heavyweight Cotton Third Degree Burn Times at the 13 mm

Air Gap..... 164

FIGURE C.4c Lightweight Blend Third Degree Burn Times at the 13 mm

Air Gap..... 165

FIGURE C.4d Heavyweight Blend Third Degree Burn Times at the 13 mm
Air Gap..... 165

FIGURE C.5a Second Degree Burn Times for All Fabrics in the Vertical
Orientation at the 13 mm Air Gap..... 165

FIGURE C.5b Second Degree Burn Times for All Fabrics in the Horizontal
Orientation at the 13 mm Air Gap..... 166

FIGURE C.5c Second Degree Burn Times for All Fabrics in the Flipped
Orientation at the 13 mm Air Gap..... 166

NOMENCLATURE

Notation

A	area (m^2)
c	specific heat ($\text{J}/\text{kg}\cdot^\circ\text{C}$)
F	radiation view factor (dimensionless)
G	blood perfusion rate (m^3/s per m^3 of tissue)
g	gravitational acceleration ($9.81 \text{ m}/\text{s}^2$)
h	convective heat transfer coefficient ($\text{W}/\text{m}^2\cdot^\circ\text{C}$)
K	loss coefficient ($\text{W}/\text{m}^2\cdot^\circ\text{C}$)
k	thermal conductivity ($\text{W}/\text{m}\cdot^\circ\text{C}$)
L	thickness, separation distance (m)
m	mass (kg)
Nu	Nusselt number (dimensionless)
P	pre-exponential factor (s^{-1})
q"	heat flux (W/m^2)
R	ideal gas constant ($8.314 \text{ J}/\text{kg}\cdot\text{mol}\cdot^\circ\text{C}$)
r	radius (m)
Ra	Raleigh number (dimensionless)
T	temperature ($^\circ\text{C}$, K)
t	time (s)
V	flame spread velocity (m/s)
x	distance (m)
y	distance (m)

Greek symbols

α	thermal diffusivity (m^2/s)
β	coefficient of thermal expansion (K^{-1})
ΔE	activation energy (J/mol)
Δt	time step (s)
δ	air gap width (m)
ν	kinematic viscosity (m^2/s)
ρ	density (kg/m^3)
σ	Stefan Boltzmann constant ($5.67 \times 10^{-8} \text{ W}/\text{m}^2 \cdot \text{K}^4$)
τ	dummy variable of integration (s), thickness (m)
Ω	Henriques' burn integral value (dimensionless)

Subscripts

b	base of insulating block, blood
c	core
conv	convection
cr	critical
f	back of fabric
i	initial, index
j	index
m	time step
o	original
rad	radiation
s	surface of insulating block, surface

CHAPTER 1: INTRODUCTION

Fire safety in space is very important. While internal fires in spacecraft are rare, they are serious enough to cause concern, as astronauts' lives become endangered. An internal fire in the command module during a launch pad test in preparation for the Apollo 1 mission took the lives of all three crew members in 1967. This led to the development of new fire safety measures for space travel and specialized materials for use in space and on earth. Two notable previous fires in space occurred during the Apollo 13 mission in 1970 and, more recently, in 1997 onboard the Russian space station Mir. With prolonged stays in space and the building of the International Space Station (ISS), fire safety in space is becoming increasingly important. Although the probability of a fire occurring in space remains quite low, the attitude is shifting towards it becoming inevitable that at some point in the future another fire in space will occur.

Spacecraft fire safety has three areas of interest, namely prevention, detection and suppression. In an attempt to prevent fires, materials of low flammability are desired for use on spacecraft and the ISS. The flammability of materials in microgravity is different than in earth's gravity. In microgravity, combustion flames are not subject to the natural convection buoyancy seen on earth that causes hot gases in flames to rise. In contrast, in microgravity there is no buoyant force to carry the hot gases away from the combustion region. For this reason, flames can take on a spherical shape as is the case when a candle is lit in zero gravity [1]. With this in mind, certain standard vertical flame spread tests on the ground are used to evaluate spacecraft material flammability, and the

results are assumed to be worst-case scenario for the microgravity environment. However, flammability tests in microgravity have shown that there are situations when flame spread is comparable to normal gravity conditions. It has been found that flammability in microgravity is sensitive to low-level forced convection as well as the oxygen concentration of the environment, therefore assuming ground tests to be worst-case scenario may not be appropriate.

There are various flammability test standards from standards organizations such as the International Organization for Standardization (ISO), the American Society for Testing and Materials (ASTM), and the Canadian General Standards Board (CGSB) to evaluate all kinds of materials used in everyday life and specialized applications on earth. Other standards can rate materials on the thermal protection they are expected to provide. It is known that inherently flame resistant fabrics such as Nomex® provide better thermal protection in normal gravity than non flame resistant fabrics such as cotton. While astronauts wear suits containing Nomex® during the launch and re-entry portions of their missions, they spend the bulk of their time in orbit when they tend to wear the same cotton clothing that they wear on earth.

The bulk of this research was to modify a CGSB standard test and use it to study skin burn injury in microgravity when a sample of clothing fabric is ignited. The results were compared to those obtained in normal gravity (1-g) to see if skin burn injury is more or less severe in microgravity than in 1-g. These findings could be used to indicate whether or not further studies, and possibly new test standards, should be developed. This introductory chapter will outline some relevant test standards, give information on how skin burn injury information is obtained, and discuss past research in this field.

1.1 Flammability and Thermal Protection Tests

There are a wide variety of test standards used to describe the burning behaviour of various materials, including clothing fabrics. Testing the flammability of a material can include measuring properties such as ignition, flame spread, and heat release. Ignition is the initiation of combustion, flame spread is the movement of the flame across the specimen, and heat release refers to the amount of energy released during the combustion process. Flammability is defined as those characteristics of a material that pertain to its relative ease of ignition and relative ability to sustain combustion [2]. Flammability tests are sometimes used to see if a material is flame resistant, which means it acts to hinder or stop flame propagation. Variables in these tests can include fabric orientation, type of heat source, and what is being measured. Thermal protection tests are used to evaluate the ability of a material to protect against skin burn injury. They are generally used on materials that pass flammability tests.

1.1.1 Flammability Tests

Both CAN/CGSB-4.2 No.27.5 [3] and ASTM D1230 [2] are flame spread tests in which the specimen is held at a 45° angle and ignited near its lower end. The ignition process is by means of propane and butane gas burners respectively, with the flame applied to the upper surface of the specimen for one second. Once ignited, the time for the flame to proceed up the fabric a specified distance, such as 127.0 mm (5 in.) in ASTM D1230 [2], is recorded. Results of this test can then be interpreted and the fabrics classified based on their average time of flame spread.

CAN/CGSB-4.2 No.27.4 [4] and ISO 6940 [5] are identical standards to measure the ease of ignition of vertically oriented specimens. CAN/CGSB-4.2 No.27.3 [6] and

ISO 6941 [7] are also identical standards, used for measuring the flame spread of vertically oriented specimens. A small flame from a commercial grade propane gas burner is the ignition source for all four of these standards. They are intended for use on apparel, curtain or drapery fabrics.

ASTM D3659¹ [8] is a vertical flammability test standard used to evaluate the burning characteristics of a fabric partially restrained at the lower corners. The 381 mm long by 152.4 mm wide (15 in. by 6 in.) specimen is exposed to a small flame at the lower edge for three seconds. A timer is started when the flame impinges on the fabric and stopped when the specimen self-extinguishes or burning ceases. The total elapsed time is recorded as the burn time, referring not to skin burn injury time, but rather to the total time the specimen was aflame. The specimen is also weighed before and after the burning to obtain a mass loss value. The rate of area spread of flame and the average destroyed area are determined from the burn time and mass loss information.

ASTM F501² [9] is a vertical test that measures the response of aerospace materials to flame. It uses a gas burner with a 38.1 mm (1½ in.) flame to ignite a 69.85 mm by 304.8 mm (2¾ in. by 12 in.) specimen. Flame time, glow time, drip time, and burn length are all reported. The entire apparatus is enclosed in a draft free cabinet. The lower edge of the specimen is directly above the burner. Flame time is the time the specimen continues to flame after the burner is removed. Glow time is the time the specimen continues to glow after it ceases flaming. Drip flaming time is the time any dripping materials continue to flame after dripping to the floor. Burn length is the distance from the original specimen edge to the farthest evidence of damage.

¹ ASTM D3659 was withdrawn in 2001

² ASTM F501 was withdrawn in 1998

The most comprehensive Canadian vertical flammability test is CAN/CGSB-4.2 No.27.10 [10]. It is used to determine the behaviour of vertically oriented flame-resistant textile fabrics. It can be used for single layer fabrics or multi-layer fabric assemblies. A fabric specimen, 200 mm long by 80 mm wide, is mounted on a vertical frame and ignited using a gas burner. The standard offers two types of ignition: surface and edge, shown in Figure 1.1. In surface ignition, the burner is perpendicular to the specimen, while in edge ignition the burner is at a 30° angle to the vertical, towards the lower edge of the specimen. For both ignition types, the flame is applied to the specimen surface for 12 seconds. The extent of flame spread is characterized in various ways. The first is a visible observation of whether or not the flame reaches any edge of the specimen, while the second uses a weight to tear the damaged area and then measures the tear and calculates a damaged length. Afterflame and afterglow times, damaged area, and burning debris are also reported. Burning debris refers to any portion of the specimen that falls during the test and continues to flame on the floor of the test location.

Other than CAN/CGSB-4.2 No.27.5[2] and ASTM D1230[3], which are 45° angle tests, the standards described in this section are all vertical tests, all ignited with an open flame burner. However, there are three different types of ignition: base, surface, and edge, which are illustrated in Figure 1.1. In the base ignition, the specimen is ignited at its lower end, with the burner mounted vertically directly underneath the vertical specimen. For the surface ignition technique, the burner is positioned horizontally, perpendicular to the vertical specimen. Edge ignition involves tilting the burner 30° from the vertical, and applying it to the fabric surface. The base ignition technique is used for ASTM D3659 [8] and ASTM F501 [9]. Either surface or edge

ignition can be used for CAN/CGSB-4.2 No.27.3 [6], CAN/CGSB-4.2 No.27.4 [4], CAN/CGSB-4.2 No.27.10 [10], ISO 6940 [5] and ISO 6941 [7]. Often surface ignition is used first, with edge ignition only being used if the specimen failed to ignite using the surface ignition technique.

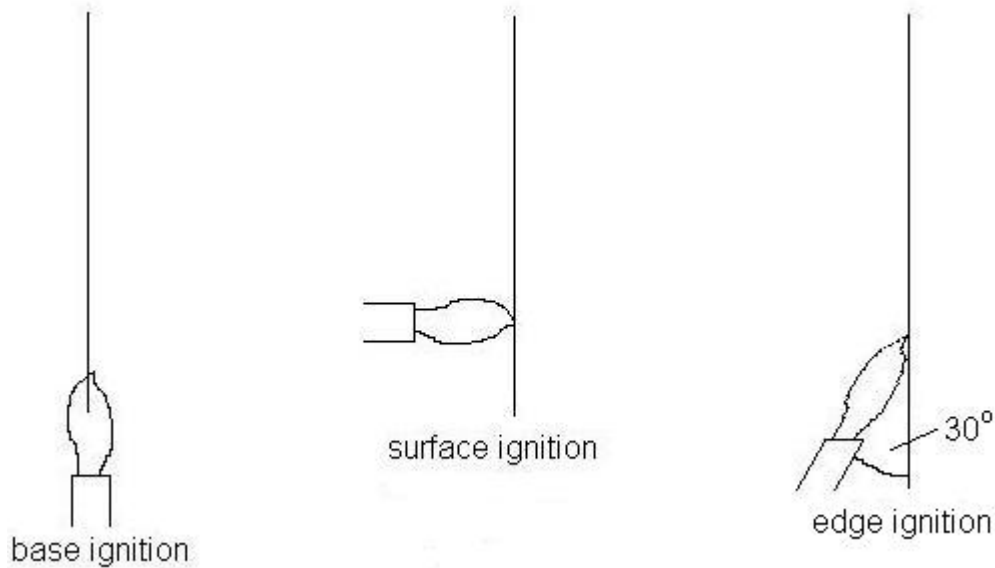


FIGURE 1.1 Various Ignition Techniques for Vertical Standard Flammability Tests

1.1.2 Thermal Protection Tests

Thermal protection tests are intended for use on materials that are not flammable. Each test is designed to evaluate the thermal protection provided by a material when exposed to various heat sources.

ISO 9151 [11] is a test standard to determine the transmission of heat through protective clothing when subjected to a flame. Specimens are placed horizontally, above a vertical propane gas burner with a nominal heat flux of 80 kW/m^2 . This heat flux is typical of a flash fire. Flash fires are of short duration and involve intense heat fluxes. They can result from the release of combustible gas, such as at a petrochemical plant. In

this test standard, the heat transfer through the specimen is measured by means of a copper calorimeter in contact with the back of the specimen. Copper disk calorimeters are discussed later in section 1.3.1. The time for a temperature rise of 24°C in the calorimeter is recorded. The average for three test specimens is then reported as the heat transfer index (HTI). HTI values are used to compare candidate materials.

The thermal protective performance (TPP) test, ASTM D4108³ [12], rates materials for thermal resistance and insulation when exposed to a convective energy level of 2 cal/cm²s (83 kW/m²) for a short duration. The standard defines the TPP rating as the thermal energy input to a fabric specimen over a particular time that is required to result in a heat transfer through the specimen sufficient to cause a second degree burn in human tissue. Both the amount of energy and the exposure time play a role in determining the skin burn injury time. The energy required to cause a second degree burn is obtained from previous work done by Stoll, which is outlined in section 1.2.3. Similar to ISO 9151 [11], the specimen is mounted horizontally with a copper calorimeter behind it, and a burner is used to provide the heat flux. The rate at which the copper calorimeter temperature increases is a direct measure of the total heat received. In this ASTM standard, an air gap can be introduced so the copper calorimeter may be a distance away from the back of the fabric, as opposed to direct contact as in the ISO 9151 [11] standard. The standard calls for a ¼” (6.4 mm) air gap for single layer fabrics and no air gap (sensor in contact with sample) for multilayer fabrics. A schematic of this test apparatus is shown in Figure 1.2.

³ ASTM D4108 was not renewed in 1995

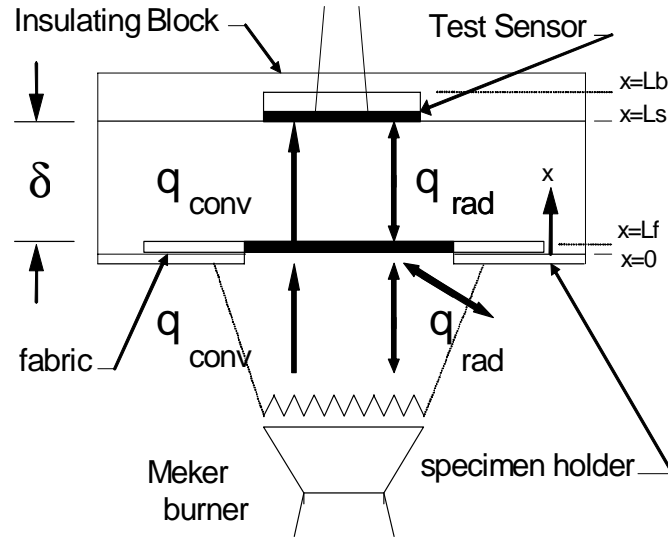


FIGURE 1.2 ASTM D4108 Thermal Protective Performance Test Apparatus

ISO 6942 [13] tests single or multilayer specimens for their protective performance against heat from a radiant source. The radiation source is six silicon carbon rods connected to a 220 V power supply. The rods reach temperatures of up to 1100°C. There are two methods in this standard. In method A, the specimen is exposed to a specific level of radiant heat and changes in appearance are recorded. Method B uses a calorimeter to measure time for temperature rises of 12 and 24°C. This information can then be used to calculate a radiant heat transfer index, which is similar to the heat transfer index (HTI) in the previously discussed ISO 9151 [11] test standard.

ASTM F1939 [14] measures the effect of radiant heat exposure at standard levels of 21 or 84 kW/m² on a fabric specimen. The radiant protective performance (RPP) is calculated. RPP is defined as the amount of exposure energy over a particular time necessary to produce a predicted second degree burn injury behind a test material. Just as in the TPP test, the heat required to cause a second degree burn is obtained from previous work done by Stoll, outlined in section 1.2.3. This test is recommended for

flame resistant fabrics. It has a vertical specimen and uses translucent quartz lamps as a vertical radiant heat source. Heat transfer is measured using a copper calorimeter sensor.

1.2 Skin Burn Predictions

Skin burn prediction has been a subject of research for quite some time. After World War I it was noted that many deaths were due to skin burns from explosions, so researchers became interested in studying skin burn injury. Extensive research was done using pigs or human volunteers as test subjects. This work, which makes predicting skin burn times possible today, will be described in this section. To understand some of this work the structure of the skin and how different skin burns are categorized must first be outlined.

1.2.1 The Structure of Skin

The skin consists of three layers: epidermis, dermis, and subcutaneous tissue. The epidermis is the thin outer-layer of the skin, containing both living and dead cells. It lacks blood vessels and has few nerve endings. The bottom layer of the epidermis is called the basal layer where cells continually divide and move up through the epidermis to replace the old dead cells that fall off the skin surface. The dermis is much thicker than the epidermis. It contains blood vessels, nerves, lymph vessels, hair follicles, and sweat glands. It is held together by a protein called collagen. The subcutaneous layer is a connective tissue layer at the base of the skin. Consisting mostly of fat, it carries major blood vessels and nerves to the overlying skin. More information can be found in an anatomy textbook (e.g., [15]).

1.2.2 Skin Burn Classification

There are different classification systems used to categorize skin burns. The most common classification method is summarized below, with complete information available from Reference [16]. This method clinically classifies burns as first, second, third or fourth degree. Classification is generally based on the depth of skin damage resulting from the burn.

First degree burns damage only the epidermis. Examples of these burns are typical sunburns. They are characterized by redness in the burned region. Discomfort is temporary and healing is rather quick, with no permanent damage.

Second degree burns may also be referred to as partial thickness burns. They destroy the epidermal layers and extend into the dermal layer as well. There is damage to sweat glands and hair follicles. Blisters, severe pain, reddening, and swelling characterize these burns. They can be categorized as either superficial or deep. In superficial cases, a significant amount of the cells at the base of the dermis remain unharmed, so healing can proceed on its own, taking anywhere from 10 to 21 days. A deep second degree burn is more severe, as it indicates that much of the dermal base is lost. In such cases, healing may require medical treatment such as skin grafting.

Third degree, or full thickness, burns destroy all the epidermal and dermal layers. There is tissue damage below the hair follicles and sweat glands into the subcutaneous tissue. The burned area will appear charred or a dry white colour. There is no possibility for spontaneous healing, so skin grafting is required.

When damage occurs to muscle, bone, ligaments, or other structures below the subcutaneous layer, it can be termed as a fourth degree burn. Healing is not significantly

different than that with a third degree burn, however, being more severe, these burns are often life threatening and burned limbs may require amputation.

1.2.3 Stoll Second Degree Burn Criterion

Stoll performed experimental research to estimate the time it takes for second degree burn damage to occur for a given heat flux exposure. Her experiments involved exposing a blackened area of the forearm to radiation of known intensity for certain lengths of time. These exposure time lengths were time to unbearable pain for the test subject, as well as time for blistering to occur [17]. The radiation source used was a 1000 W projection lamp attached to a variable resistor to obtain the desired irradiation. Experimental data was obtained for heat fluxes of 0.1 to 0.4 cal/cm²s (4.2 to 16.8 kW/m²) [18]. These results can be theoretically extended to include heat fluxes from 0.4 to 1.0 cal/cm² (16.8 to 42.0 kW/m²) as well. The Stoll curve showing time to second degree burn for various heat fluxes is shown in Figure 1.3.

This information can be converted to the total amount of energy which must be absorbed by the skin to cause second degree burns for a given exposure time. If the energy absorbed by a test sensor, such as a copper disk, is measured in an experiment, the time for the Stoll criterion to be exceeded can easily be determined. This is the information used to assess time to second degree burn based on the Stoll criterion in test standards such as ASTM D4108 [12] and ASTM F1939 [14]. In these standards, there is a table that has exposure time, heat flux, total heat, and calorimeter equivalent. The exposure time and heat flux come directly from Stoll's work, as this is what is plotted in Figure 1.3. This curve can be represented by the following equation [13]:

$$q'' = 50.123t^{-0.7087} \quad (1.1)$$

where q'' is the incident heat flux in kW/m^2 and t is the time to second degree burn in seconds.

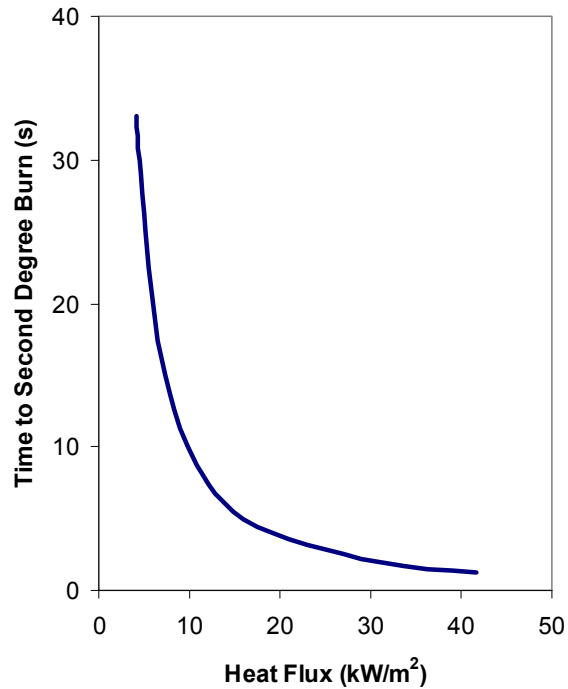


FIGURE 1.3 Stoll Criterion Time to Second Degree Burn for Various Incident Heat Fluxes on Bare Human Skin

The calorimeter equivalent values in the standard tables are again based on Stoll's work and allow the temperature rise of the sensor used in the test, such as an 18 g copper disk calorimeter, to be compared directly with exposure time to determine time to second degree burn. A second degree burn is said to have occurred when:

$$T \geq T_o + (8.871465 \times t^{0.2905449}) \quad (1.2)$$

where T_o is the initial temperature of the sensor.

A few disadvantages of the Stoll second degree burn criterion technique to be aware of are that this criterion is based on limited data obtained using a rectangular heat pulse [18], and that it only yields information on predicted second degree burns.

1.2.4 Henriques' Burn Integral

Henriques was one of the first researchers in the area of skin burn injury. He performed many experiments on pig skin, initially exposing the skin to hot water of varying temperatures and observing the physical changes in the skin [19]. When analyzing the experimental data it was found that skin damage could be represented by a first order Arrhenius rate equation, just like many other chemical and physical rate processes [20]. The rate of tissue damage is given by

$$\frac{d\Omega}{dt} = P \exp\left(\frac{-\Delta E}{RT}\right) \quad (1.3)$$

This can be integrated to obtain

$$\Omega = \int_0^t P \exp\left(\frac{-\Delta E}{RT}\right) dt \quad (1.4)$$

This integration is carried out over the time the basal layer temperature, T , is greater than or equal to 44°C , which is the threshold temperature for thermal damage to skin.

Second degree burns were said to occur when Ω , the value of Henriques' burn integral (non-dimensional), is equal to 1.0. With this arbitrary value set and knowing the universal gas constant, R , the pre-exponential factor, P and the activation energy, ΔE were graphically determined from the experimental burn data. The activation energy, ΔE , was found to be 150 000 calories per mol. This is very close to that of thermal denaturation of proteins, which is thought to be what happens in the skin during heating.

The pre-exponential factor, P , was found to be $3.1 \times 10^{98} \text{ sec}^{-1}$. Knowing these values, times to second degree burn of skin could be determined for various temperature-time exposures. Further work found that a critical value of $\Omega=0.53$ can be used to predict the time for a first degree burn and that by using the temperature at the base of the dermis of the skin in Equation (1.2) and a critical value of $\Omega=1.0$, third degree burn times can be predicted. For this research, temperature-time data from skin simulant sensors, discussed in section 1.3.2, can be used in conjunction with a skin heat transfer model and Henriques' burn integral to compute times to second and third degree burns of human skin.

This burn integral is advantageous because it can be used for any heat flux and times to first, second and third degree burns can be obtained. The disadvantage of this method is that the calculations are more complicated. To obtain burn times, the use of a computer and specialized software is often necessary.

1.3 Heat Flux Sensors

Heat flux sensors are measuring devices that monitor changes in output that can be related to the heating or cooling of the sensor. By monitoring the temperature increase of a sensor and knowing its thermal properties, the heat flux to its surface can be determined. There are various types of heat flux sensors. The two used in this research are copper calorimeters and thin-film skin simulants. Both use thermocouples to measure temperatures. Similarities and differences between them are outlined in a paper by Torvi [21], and are briefly discussed below.

1.3.1 Copper Disk Calorimeter

Copper calorimeters are used in thermal protection test standards such as ISO 9151 [11], ASTM D4108 [12]. Both of these tests measure the heat transfer behind a material subject to a flame. The rate at which the copper calorimeter temperature increases is a direct measure of heat energy received. The copper calorimeters in these two standards are very similar in size and shape, however, the ISO standard has only a single type T thermocouple on the back of the disk, while the ASTM standard calls for four type J thermocouples on a single copper disk. For this research, ISO type copper calorimeters were used.

When using copper disk calorimeters, a lumped heat capacity analysis is employed. The temperature and heat flux data can be compared to the Stoll curve. When the Stoll criterion is exceeded, a second degree burn has occurred. This data analysis is outlined in section 4.2.1.

1.3.2 Skin Simulants

Skin simulants are thin-film heat flux sensors with thermal absorptivity ($\sqrt{k\rho c}$) similar to that of human skin. The material used for the skin simulants in this research is colcerceran, an inorganic mixture of calcium, aluminium, silicate with asbestos fibres, and a binder. These heat flux sensors were developed for use in the thermal mannequin tests at the University of Alberta [22].

The skin simulants are treated as semi-infinite solids for heat flux analysis. One problem with these sensors is that they develop internal temperature gradients that must be eliminated before a new test is performed. The temperature-time data obtained from

these sensors during heat exposures can be used in conjunction with a skin heat transfer model and Henriques' burn integral to determine times to second and third degree burns. This data analysis is outlined in section 4.2.2.

1.4 Microgravity Fire Safety Research

There is a considerable ongoing body of research for fire prevention, detection, and suppression in a microgravity environment (e.g. [23]). When it comes to clothing flammability, the key aspect of fire safety is prevention. Tests are performed to ensure materials meet the flammability safety requirements to be used onboard the space shuttle and in other space environments. Along with the research being done in this area, there is considerable research being conducted to better understand the behaviour of flames and the combustion process in low gravity environments. This section will discuss some of the applicable research done, as well as the facilities that house the research projects.

1.4.1 Material Testing for the Shuttle and ISS

There are test standards for selecting materials that can go onboard human-crew space missions. These tests are designed to ensure astronauts' safety from the risk of fires while in space. The NASA standard is NASA STD-6001[24], which covers a wide variety of tests, all with different purposes. The most commonly used is Test 1 – Upward Flame Propagation. In this test, a 300 mm long by 50 mm wide vertical sample is ignited at the bottom. Test 1 simulates the beginning of a fire with an ignition flux typically of 75 kW/m^2 maintained for 20 seconds. The chemical ignition source is initiated by means of current flowing through a bare nickel chromium wire. It is a self-extinguishment test, so the flame is not to progress more than 150 mm. Also, it is not to

ignite a sheet of paper mounted horizontally 200 mm below the base of the sample. This test is performed inside a closed chamber in the worst-case oxygen concentration and pressure environment in which the material will be used. Test 1 is performed on the ground in a normal gravity environment. For a vertical test such as this, the natural buoyancy forces in normal gravity aid the heat transfer because both the movement of hot gases and the flame spread are in the upward direction. For this reason, this test environment has always been assumed to be worst-case scenario, with materials assumed to perform better in the microgravity environment.

1.4.2 Flame Spread over Thin Solid Fuels in Low Gravity

Flames in microgravity are not subject to the buoyancy forces in normal gravity. However, past research has found microgravity combustion to be extremely sensitive to atmospheric flow and composition. An experiment with thin paper fuels [25] indicated that in a high oxygen concentration (greater than 40%), quiescent environment, flame spread rate is independent of gravity level. Other experiments with ash-free filter paper [26] have shown that flame spread rate increases with pressure in quiescent microgravity, quite different than in normal gravity.

The Radiative Ignition and Transition to Flame Spread (RITSI) experiment [27], conducted at the Japanese Microgravity Centre (JAMIC) drop tower facility and on the STS-75 Shuttle mission in 1996, uses a rectangular sheet of paper for a specimen. A nitrogen-oxygen mixture was vented over the specimen at speeds of 0 to 6.5 cm/s. A flame was found to propagate under all conditions studied, except at zero flow and 21% oxygen concentration. When flame spread was observed, it was always in the upstream

direction (towards the flow). Downstream flow was observed only after the upstream flow was complete. The flame spread in a fan-shaped pattern.

An experiment was conducted on Mir in 1998 to observe the concurrent-flow flame spread along cylindrical samples of three plastic materials, including polymethylmethacrylate (PMMA) [28]. The results indicated that each material had its own minimum concurrent air flow necessary to maintain flame spread in microgravity. They were all quite low, less than 1 cm/s, at 21% oxygen. They were also found to decrease further towards zero as oxygen concentration was increased.

Some current research is combining experimental investigations with numerical modelling. In the Solid Inflammability Boundary at Low-Speed (SIBAL) experiment, researchers are studying the effect of low-speed flow on spreading and extinction processes over solid fuels [29]. One part of this experiment deals with the comparison of extinction limits and spreading rates in opposed and concurrent spreading flames over thin solids. The focus here is on purely forced flows. A two-dimensional opposed flow flame spread model with flame radiation has been formulated and solved numerically. Parameters varied included oxygen percentage, free-stream velocity and flow entrance length. This model has also been compared to a similar model developed for concurrent flow flame spread. The thin solid fuel of choice for much of the SIBAL experiment is Kimwipes® (Kimberly-Clark, Dallas, TX).

Ignition and flame spread over solid fuels in microgravity is being studied at the JAMIC drop tower facility by igniting a PMMA sheet with a carbon dioxide laser [30]. There are two transition stages in this study, one from the onset of ignition to the formation of an initial anchored flame, and the second is the flame growth stage from the anchored flame to a steady fire spread rate. Two different thicknesses are being used

to represent materials that are thermally thin and materials that are thermally thick in terms of their heat transfer behaviour. Along with the experimental work, a numerical code based on a modified version of the Fire Dynamic Simulation code [31], developed by the US National Institute of Standards and Technology (NIST), has been developed.

Recently, some researchers have noticed a gap in the literature between studies of material flammability and flame spread phenomena in normal gravity and those conducted in microgravity, with or without forced flows. From a practical point of view, flame spread and material flammability have not been studied under partial gravity conditions that are the natural state for space travel explorations such as the Moon and Mars. To begin to bridge the gap, partial-gravity experiments (from 0.1-g to 1-g) were performed considering both upward and downward flame spread over thin solid fuels aboard the NASA KC-135 aircraft [32]. Kimwipes®, 2 cm wide, were burned in air at a reduced pressure of 27.6 kPa. The upward burning spread rate varied linearly with gravity level. The downward spread rate is non-monotonic and peaks near Martian gravity levels (0.38-g). Along with the experiment, some modelling work has also been done to compliment an existing three-dimensional model of steady upward spreading flames (buoyant flow). A new three-dimensional downward spread model for mixed forced and buoyant flow was also completed.

1.4.3 Test Development for Flammability in Microgravity

Some work is being done to develop tests that will more accurately represent flammability in a microgravity environment. The Equivalent Low Stretch Apparatus (ELSA) [33] and Forced Ignition and Spread Test (FIST) [34] are two such tests that may help improve selection of materials for use in space environments.

ELSA is an earth-based test to assess material flammability for microgravity and extraterrestrial fire-safety applications [33]. The researcher has modified a standard oxygen consumption (cone) calorimeter to provide a bench-scale test environment that simulates the buoyant or ventilation flow that would be generated by a flame in a spacecraft or extraterrestrial gravity level. It uses an inverted cone geometry with the sample burning in a ceiling fire configuration. The apparatus has a mass-flow controlled forced-air flow through a nozzle into the cone to augment low buoyant stretch. Initial testing has been done with 100 mm by 100 mm PMMA samples that are 24 mm thick. A standard cone calorimeter is used in such flammability standards as ASTM E1354 [35] and Test 2 from NASA STD 6001 [24]. It was found that normal cone tests such as these significantly underestimate the risk in microgravity. To provide a more accurate flammability test for materials to be used in partial and micro gravity environments, an ELSA prototype is being implemented into NASA's White Sands Test Facility's Controlled Atmosphere Cone Calorimeter facility. It will be calibrated with the PMMA samples, and then used to test the flammability of many other materials that have space applications.

FIST is being used to study the flammability characteristics of combustible materials in forced convective flows [34]. The methodology for this test is based on ASTM E1321 [36], Lateral Ignition and Flame Spread Test (LIFT), which determines ignition and flame spread characteristics of materials to produce flammability diagrams. LIFT relies on natural convection to bring air to the combustion zone and fuel vapour to the pilot flame. In the absence of gravity, there is no natural convection. Instead, FIST uses forced flow as the dominant transport mechanism, representative of flows typically seen onboard spacecraft. Thus, it is better suited to determine flammability

characteristics of materials used for space applications. The FIST apparatus can be used for a wide range of materials, with recent work being done on piloted ignition of blended polypropylene fibreglass composites [37].

1.4.4 Microgravity Research Environments

There are a variety of ways to achieve low gravity for periods of time to allow microgravity experiments to be performed. These include drop towers, parabolic aircraft, sounding rockets, space flight vehicles, and the ISS. The levels of gravity reached, as well as the low gravity exposure time, differ in each new environment. These research platforms are outlined below while further information is provided in Reference [38].

Drop towers provide researchers with a short amount of quality low gravity time. When using a drop tower facility, the experiment is prepared in a capsule and then released, allowing it to freefall for a certain distance. Depending on the freefall distance, the low gravity exposure time varies. Drop tower facilities include ZARM in Bremen, which allows 4.74 seconds of freefall time, NASA's 5.18 second drop tower at their Glenn Research Center in Cleveland, and the Japanese Microgravity Center (JAMIC) in Japan which has up to ten seconds of low gravity exposure. All these facilities achieve low gravity levels of 10^{-5} g. Individual tests are relatively short, but many tests can be done in a single day.

Parabolic aircraft are another way of achieving a microgravity research environment. Examples of these aircrafts are Novespace's Airbus A300 and NASA's KC-135, both of which are modified commercial aircrafts. To achieve low gravity, these aircraft perform parabolic flight manoeuvres, giving the opportunity to achieve

short periods of free fall. On the upward arc, the thrust of the airplane is adjusted so that there is no lift. The plane is then in free fall since nothing reduces the force of gravity. The plane remains in free fall over the top of the parabola and part of the downward arc. Microgravity conditions are achieved for time periods of around 20 to 25 seconds, in which it is possible to conduct experiments. The microgravity levels reached are the worst quality of the test environments, providing only 10^{-3} g levels, but exposure time is lengthier than drop towers. Researchers often use these flights for preliminary experimental work that could eventually lead to time aboard a space flight. Parabolic flights can also be used to achieve partial gravity test environments such as those of the Moon and Mars.

Sounding rockets can achieve high quality gravity levels of 10^{-7} g for minutes at a time. The experiment is enclosed in a capsule and powered by rocket motors. After it is launched a couple hundred kilometres up in the air it freefalls into the ocean where it is recovered. The main disadvantage of this research platform is that it is rather expensive to conduct such tests.

The Shuttle and the ISS and any other platform that are actually in the zero-gravity conditions of space are the ideal research platform for microgravity experiments. The time periods for experiments are significantly longer than any test environment previously discussed. Experiments can now be conducted for months or years instead of seconds or minutes and the gravity levels are very low ($<10^{-7}$ g). The main downfall of this platform, other than the high cost, is that the opportunities to obtain experiment time on space flights and the ISS are still very limited.

1.5 The Spacecraft Fire Safety Facility Test Rig

The Spacecraft Fire Safety Facility (SFSF) is an experimental test rig that flies on NASA's KC-135 low-gravity aircraft. This rig was constructed by researchers at the NASA Glenn Research Center in Cleveland, Ohio to perform various types of combustion experiments under a variety of experimental conditions. It has been used for various low-gravity flammability and fire safety experiments in the past. A list of some previous publications and experiments performed using the SFSF can be found in the user's guide [39]. Some examples are extinction of a diffusion flame over a PMMA cylinder by depressurization in low gravity, and solid diffusion flame extinction and transition to microgravity. The previous discussed FIST experiment has also been flown using this rig. Another experiment deals with suppression of PMMA flames with the objective being to determine the efficiency of carbon dioxide and helium fire suppressants in a microgravity environment. The SFSF rig is the test rig used to conduct the microgravity research for this experimental study. It is described in detail in section 2.1.

1.6 Cotton Flammability and Skin Burn Injury Experiments

The most comprehensive cotton flame spread and associated skin burn injury research to date came as a result of work done for by the Government Industry Research Committee on Fabric Flammability. This research committee consisted of four research partners: the Factory Mutual Research Corporation (FMRC), the Georgia Institute of Technology (GIT) School of Mechanical Engineering, the Gillette Research Institute (GRI) Harris Research Laboratories Department, and the Massachusetts Institute of Technology (MIT) Department of Chemical Engineering's Fuels Research Laboratory.

An overview study of the work done was conducted by a fifth separate group in the Department of Mechanical Engineering at MIT [40] which is briefly outlined below. Much of the work was done with cotton and cotton/polyester blends. Some wool and synthetic fibres were also tested. Fabric specimens were ignited by a burner flame and flame spread was visually observed. A skin simulant sensor was used to obtain the data necessary to evaluate burn injury. Both thermal dosage to the skin and the estimated depth of damage below the skin surface were reported. Experimental variables included fabric types, blends and weights, the angle of the fabric, the direction of burn, and the spacing between the fabric and the simulant. It was found that skin damage and flame velocity were both proportional to the weight per unit area of the cotton fabric. In general, heavier fabrics experienced slower flame spread rates and greater burn injury damage depths than the lighter weight fabrics of the same kind. For a given fabric weight, thermal injury was highest at the minimal spacing distance (1/8" or 3.175 mm) where the average speed of flame propagation was lowest.

1.7 Scope of Research

The main purpose of this research was to provide a preliminary investigation into the severity of skin burn injury times experienced in a microgravity environment. This work was done so the results could be compared to those obtained in normal earth gravity to see how the skin burn times are affected by different gravity levels. If the microgravity results are less severe than the 1-g test results, the current procedure of running tests for shuttle and ISS materials on the ground in 1-g and assuming this to be worst case may still be acceptable. However, if the microgravity burn times are more

severe than those in 1-g, further investigation into skin burn injury in microgravity may be required.

With this goal in mind an apparatus needed to be created for use in a microgravity environment. It was designed to fit in the SFSF and yet be similar to an existing standard test apparatus for ground tests in hopes that results could be linked back to a standard test. Since skin burn injury times were of primary concern, the factors that affect skin burns, such as heat fluxes, flame size, and flame spread rates, all had to be observed. The apparatus and procedure were created to obtain heat fluxes necessary to predict skin burn injury as well as flame spread rates. Fabrics chosen for use in this research include a regular T-shirt weight fabric and a heavier golf-shirt weight fabric. These were both ordered in 100% cotton and 50% cotton/50% polyester blend. The cottons were chosen as they are typically what astronauts wear for the majority of their space missions.

1.8 Overview of Thesis

The next chapter of this thesis will describe the experimental apparatus designed and used during this research. This is followed by a description of the test procedures performed at the various locations in which this research was conducted. Methods used to process the data gathered from the experiments are described. Flame spread rates, heat fluxes, and skin burn injury predictions are then presented and discussed. This thesis then closes with conclusions from the completed research and recommendations for further work.

CHAPTER 2 EXPERIMENTAL APPARATUS

This chapter will outline the components and design of the experimental apparatus. The major components of the Spacecraft Fire Safety Facility will be discussed, as it houses the microgravity experimental apparatus. The design of a new insert specific to this research will then be discussed, outlining design concerns and describing the end prototype piece by piece. The chapter concludes with a brief outline of the fabrics chosen for use in this research.

2.1 Spacecraft Fire Safety Facility

This research program involved the design of an insert to fit inside the Spacecraft Fire Safety Facility (SFSF) in order to obtain the microgravity data. The SFSF is an experimental test rig that flies on NASA's KC-135 low gravity aircraft. Constructed by researchers at NASA's John Glenn Research Center in Cleveland, Ohio, the SFSF has been used for numerous microgravity experiments [39]. This section will include a brief description of the rig's five main components: combustion chamber, sample holders, gas flow system, imaging system, and data acquisition and control system.

2.1.1 Combustion Chamber

The combustion chamber is the section of the rig that houses the experiment. It is a large aluminium cylinder in which the combustion experiments take place. The

chamber is 254 mm (10 in.) in diameter and 510 mm (20 in.) tall. During microgravity experiments the chamber is closed and sealed from its surroundings. A top lid can be removed between tests to allow access to the components inside the chamber. To allow viewing of the experiment inside the chamber, three windows are located in the chamber walls. The two side windows are circular, 104.6 mm (4.1 in.) in diameter, while the front window is rectangular, 152.4 mm (6 in.) by 101.6 mm (4 in.) in size. The centre of the viewing windows does not correspond to the vertical centre of the combustion chamber, but rather are closer to the base, with the centres located 203.2 mm (8 in.) up from bottom of the chamber.

The chamber has a hole in its side wall to allow necessary wiring to connect the apparatus to the power supply and the data acquisition and control system. Once the wires are in place this wire pass-through area is completely sealed so the chamber may still be pressurized when closed. The standard set-up of the rig allows four type K thermocouples and four 28 VDC power inputs.

2.1.2 Sample Holders

The sample holders house the actual samples to be burned during the experiments. They are placed inside the combustion chamber while the experiment is run and thus are limited in size by the chamber. New sample holders are designed for new SFSF experiments. They are often thin pieces of stainless steel that can be lowered into place on a set of guide rails inside the chamber. They hold the combustion sample and any thermocouple, igniter, or other power wires required for the experiment. Often multiple sample holders are made so that there is a new specimen prepared for each test point, as the nature of combustion experiments is such that test specimens are often not

reusable. It is also desirable to make the sample holders easy to change so as not to waste precious time on a low gravity aircraft flight. During a flight, parabolas are flown consecutively providing roughly 20 seconds of microgravity in the middle of the parabola, as will be further discussed in section 3.4. In order to obtain a maximum number of data points from the consecutive parabolas, samples must be switched as fast as possible.

2.1.3 Flow System

The flow system of the SFSF was designed to create a desired constant velocity flow through the combustion chamber. The basic flow direction is from bottom to top. Gas enters the chamber from an inlet at the base and exits through the lid at the top. During experiments, the gas is supplied by large pressurized gas bottles attached to the rig. From the gas bottles, it flows through mass flow controllers, check valves, and an inlet solenoid valve up through the chamber inlet. Passing through a flow expansion section and a porous bronze plate, the gas continues up through the chamber and out the lid. From here the gas proceeds through a vent valve and a motorized control valve to the facility flow outlet. During KC-135 flights, the facility flow outlet is simply a line that vents overboard.

The flow system can accommodate up to three gas bottles. Two of the mass flow controllers have an operating range of 25 to 500 standard litres per minute (SLPM), corresponding to a maximum velocity of 17 cm/s in the combustion chamber. The third controller has a higher operating range, 100 to 2000 SLPM, having a maximum velocity of 70 cm/s in the chamber; however, this upper limit is not recommended as the pressures become quite high and safety becomes a greater concern.

Pressure in the chamber is also monitored and controlled. It can range from zero to 3.4 atm. The chamber pressure is measured by means of a pressure transducer, and controlled by a PID controller which is connected to the motorized control valve downstream of the flow. The pressure can be changed manually or by using computer control.

2.1.4 Imaging System

The rig contains imaging hardware including a colour CCD video camera and a colour infrared temperature camera. The video camera is a Panasonic WV-CL352 (Panasonic, Secaucus, NJ) while the infrared camera is a Prism DS IR camera that uses a 25 mm IR lens (FLIR Systems Inc., Portland, OR). Both video outputs pass through a Horita-TG-50 time code generator (Horita, Mission Viejo, CA) where a running experiment time is overlaid on the image. The time code generators are configured so identical time stamps will appear on the two videos. The IR camera video output also passes through a Horita-SCT-50 titler so of pressure, velocity, acceleration, test name, and other SFSF control parameters appear on the image. Both new video output signals are then recorded using a portable Sony DVCam digital video recorder (Sony Corporation, New York City, NY). Because of the set-up of the rig, the infrared and video cameras cannot provide the same view at the same time. They are often used simultaneously to obtain orthogonal images. Mounted side by side, one takes a side view of the experiment in progress, while the other achieves a front view using a mirror mounted to the window frame. The cameras record 30 frames per second.

2.1.5 Data Acquisition and Control System

The SFSF has a personal notebook computer mounted on its top surface. The computer contains LabVIEW™ (National Instruments, Austin, TX), which is a commercial software that allows the user to write a custom control sequence with a graphical user interface. This software, along with the associated input and output hardware, provide a data acquisition and control system capable of collecting data and controlling all aspects of the experiment.

2.2 Design of the Sample Holder

For this research, a new sample holder was designed to fit into the SFSF to obtain the microgravity data. During the design it was desirable to create an insert that would be able to be used on the ground, be similar to an accessible standard flammability test apparatus, and fit inside the combustion chamber. By looking through various test standards it was decided that the CAN/CGSB-4.2 No.27-10 [10] specimen size, described in section 1.1.1, was the most compatible with the size of the combustion chamber and viewing windows. This standard test apparatus could also be used at the University of Alberta's Textile Analysis Service for some ground testing. For these reasons, it was decided to design the apparatus to accommodate a specimen 200 mm by 80 mm, as specified in this standard. The next main concern was then that a gas burner ignition source, as in the standard, was not allowed in the SFSF rig during the microgravity flight for safety reasons, so a new ignition source had to be found.

Once the test standard was chosen, the insert was designed to satisfy the purpose of the experiment, that is, to obtain skin burn injury information when a fabric is burning. Design considerations were to create an apparatus that would: house both the

fabric specimen and the equipment required to obtain burn injury information, fit inside the Spacecraft Fire Safety Facility's combustion chamber, and allow quick and easy specimen changing. The apparatus consists of various components to accomplish all these goals. The components, their purpose, and reasons for their design are outlined in the following sections.

2.2.1 Sample Card

The sample card is the base part of the apparatus to which all other required components can be mounted. SFSF experiments are conducted in the combustion chamber of the rig. As noted earlier, the combustion chamber is an aluminium cylinder, 254 mm in diameter and 510 mm high. There are guide rails on opposite sides of the chamber to allow the sample holder to slide into place in the centre of the chamber. With the guide rail stand-off distance and clearance at the top of the chamber, the sample card was required to be slightly smaller than the chamber dimensions. The cards were made 225 mm ($8\frac{7}{8}$ in.) wide and 470 mm ($18\frac{1}{2}$ in.) tall to fit in the chamber. They were manufactured out of stainless steel to withstand the high temperatures of the experiment. It was desirable to have the sample card thin for a couple of reasons. First, a thinner sample card allows for a better view of the specimen for the side viewing camera. Second, the chamber guide rails are designed to fit thin cards. A thickness of 0.9 mm was chosen, as it was within the acceptable range and provided sufficient stiffness.

The sample card has a rectangular cut-out in the middle 90 mm wide by 210 mm tall. Just slightly larger than the fabric specimen itself, this opening allows the back of the fabric specimen to be open to the heat flux gauges for the tests. The centre of the

opening is positioned 203 mm from the bottom of the card, shown in Figure 2.1. This makes it vertically centred in the viewing windows of the chamber.

Mounted on the front surface of the sample card are four smaller pieces of stainless steel, their purpose being to guide and hold the fabric specimen holder into place. Two “L” shaped pieces are welded to either side of the centre opening. They are 1.5 mm thick – the same thickness as the specimen holder itself. Positioned at the edges of the opening, the specimen holder will slide along these into place. They are shown in place in Figure 2.1.

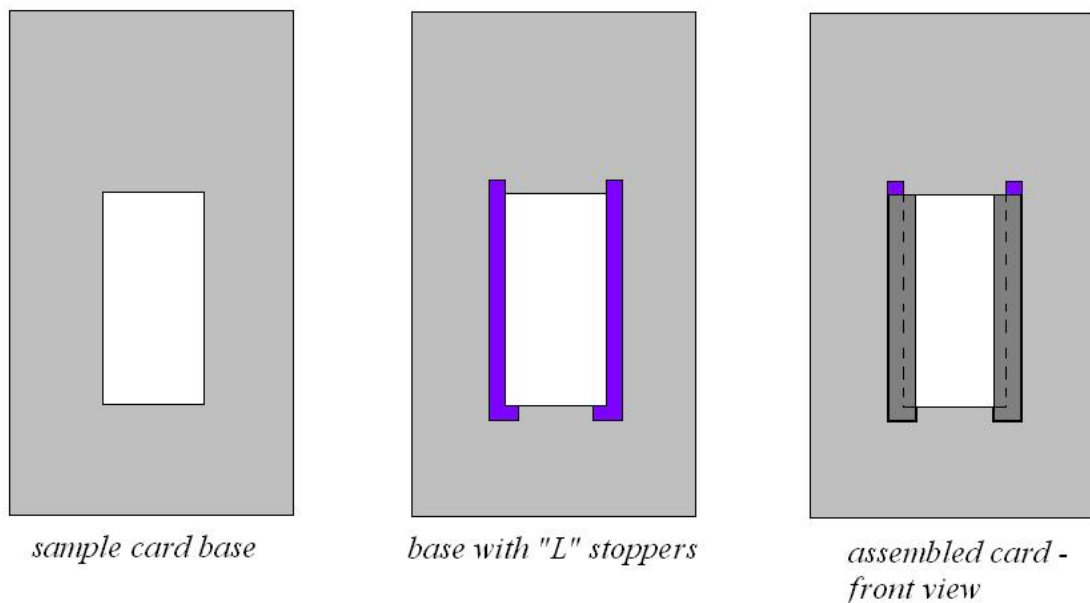


FIGURE 2.1 Front View of Sample Card Assembly

The base of the “L” provides a stop for the specimen holder so it does not slide all the way through. Located just at the corners, these stops do not disrupt the flow at the base of the fabric. The other two steel pieces are thinner, at 0.9 mm thick, and are welded directly on top of the “L” shaped stoppers, as shown in Figure 2.1. They are rectangular, slightly wider than the long part of the “L” pieces, and are fastened in place in order to

extend out over the specimen holder so the holder does not fall off the front of the card. Essentially these four pieces of steel provide a groove the thickness of the specimen holder so that the holder can slide into place directly above the centre cut-out of the card. The top pieces are tighter near the bottom, to prevent the specimen holder from moving around once in place.

Extending from the back surface of the sample card are four steel bolts, 30 mm in length, 3 mm in diameter. They are positioned outside the four corners of the centre cut-out, 10 mm in either direction. These bolts allow the sensor board to be mounted on the backside of the sample card, on the opposite side of the fabric specimen, to obtain the necessary data for determining heat fluxes used to estimate skin burn injury. Four nuts are also used to keep the sensor board in place after it is positioned on these bolts.

2.2.2 Specimen Holder

The specimen holder is used to hold the fabric specimens to be burned during the experiments. Both the specimen size and specimen holder design are taken from the CAN/CGSB-4.2 No. 27-10 [10] test standard. The specimen size is 80 mm wide and 200 mm long. The specimen holder is 100 mm wide and 220 mm long, with a centre cut out 70 mm wide by 190 mm long. Also manufactured out of stainless steel, it is 1.5 mm thick. A specimen holder can be seen in Figure 2.2a, with a fabric specimen in place in Figure 2.2b.

The CGSB standard calls for pins located at each corner on the specimen holder to attach the fabric in place; however, due to the safety concern of sharp object possibly floating around freely during the flight, the pins were removed and the fabric is now fastened to the holder by metallic tape. The tape pieces cover only the long edges of the

fabric and are about 5 mm in width. A fabric specimen mounted on the specimen holder using the metallic tape can be seen in Figure 2.2b.



FIGURE 2.2a Specimen Holder



FIGURE 2.2b Fabric Specimen on Specimen Holder

2.2.3 Heat Flux Gauges

As previously discussed, two different types of heat flux gauges were used to gather data in this research. Figure 2.3a shows a skin simulant sensor, while Figure 2.3b shows a copper disk sensor.



FIGURE 2.3a Skin Simulant Heat Flux Gauge



FIGURE 2.3b Copper Disk Heat Flux Gauge

The skin simulants, cylindrical sensors 22 mm in diameter and 19 mm in height made of colceran with a type T thermocouple mounted on their surface, were obtained from the University of Alberta, where they manufacture large quantities for use in their thermal mannequin [22]. They were calibrated at the University of Alberta to obtain the thermal absorptivity ($\sqrt{k\rho c}$) of each material. This was done by subjecting the sensors to a movie projector lamp of known intensity while measuring the surface temperature of the sensor. The incident heat flux from the projector lamp, q'' , is known. The initial temperature of the skin simulant, T_i , is recorded and the surface temperature, $T(x=0)$, is measured during the calibration period. For relatively short exposures, the heating of the sensor is assumed to follow the closed form solution for the surface of a semi-infinite solid [41]

$$T(x=0,t) - T_i = \frac{2q''\sqrt{t}}{\sqrt{k\rho c\pi}} \quad (2.1)$$

Since the incident heat flux and the temperature-time profile are known, the $k\rho c$ value for the sensor can be found.

The copper disks were manufactured by the Engineering Shops at the University of Saskatchewan following the specifications in the ISO 9151[11] test standard. They are thin disks made out of 99% pure copper. These sensors are 40 mm in diameter and 1.6 mm thick, and their mass is 18.00 ± 0.06 g. Once the disks were made, a type T thermocouple had to be silver soldered in place on the back of each disk, again following the ISO 9151[11] specifications. The end of the constantan wire is soldered to the centre of the disk, while the copper wire is soldered in place 5 mm from the outer edge of the disk. The surfaces of the heat flux gauges were painted black to ensure an

emissivity of around 0.95. This was done using a high temperature application spray paint – Tremclad High Heat Enamel (General Paint Corporation, Vancouver, BC). During testing it is important to maintain clean surfaces on the sensor faces. This is often accomplished by wiping the sensor faces with a damp cloth. If necessary, the paint can be removed with acetone and then reapplied.

2.2.4 Sensor Board

The sensor board is used to house the heat flux gauges described in the previous section. There are four heat flux gauges in the sensor board, as there are four available thermocouple ports in the SFSF. Because the gauges have type T thermocouples and the four available ports in the SFSF are normally type K thermocouples, the SFSF ports were changed to type T for this experiment. The gauges are mounted in a Marinite® block. Marinite® is an insulating material often used to mount heat flux gauges in various test standards including ASTM F955 [42] and in a new cylindrical test apparatus for thermal protection fabrics developed at the University of Alberta [43]. Marinite® was chosen for its flame and heat resistant properties, its rigidity that allowed the board to be manufactured to hold the sensors, and because it gave off less dust than other insulating materials to help keep the SFSF clean.

The gauges are equally distributed along the face of the sensor board to essentially span the entire length of the fabric specimen. For this to be the case, the centres of the gauges are located 45 mm apart. The Marinite® block is 235 mm long and 110 mm wide, and was chosen to be 19 mm thick, the same thickness as the skin simulant sensors. Four holes were cut out along the centre axis of the block to house the four sensors. The two different types of sensors employed, skin simulant and copper

disk heat flux gauges, alternate positions along the Marinite® block. The holes for the skin simulants are simply the same diameter as the sensors (22 mm), drilled all the way through the block, shown in Figure 2.4. Because the copper disks are only 1.6 mm thick, the holes for mounting them in the Marinite® block are slightly more complicated. The specifications for the copper disk mountings are taken from the ISO 9151[11] test standard and are shown in Figure 2.4. Behind the copper disk is an air space 37 mm in diameter, 9 mm deep to help minimize heat losses from the back of the disk during experiments. Each gauge is held in place with two small finishing nails on opposite sides. The nails are hammered in from the front side of the board, allowing the top of the nail to provide a lip so the gauge will not slide out of place.

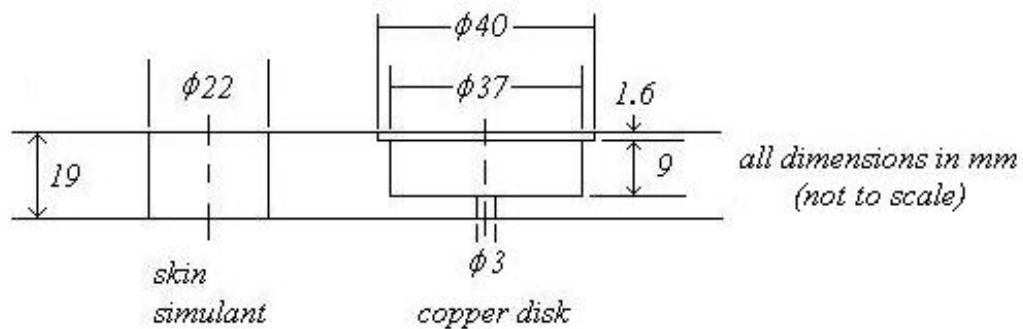


FIGURE 2.4 Side View of Heat Flux Gauge Mounting Holes in the Sensor Board

In order to mount the sensor board on the apparatus, a steel plate and holder were manufactured to enclose the Marinite® block and add rigidity to it. The block lies on a steel plate 260 mm by 140 mm, 1.5 mm thick with a centre cut-out 180 mm by 70 mm so the faces of the gauges are open to the back of the fabric specimen, as seen in Figure 2.5a, when the complete apparatus is assembled. Another thin steel piece (0.9 mm) was cut out to attach the Marinite® block to the front plate. It is essentially a rectangle, 255

mm by 150 mm, with its corners removed and a centre rectangular cut-out 200 mm by 80 mm to allow the thermocouple wires from the heat flux gauges to extend out the back, shown in Figure 2.5b. The thin piece sits on the back side of the block and its edges are bent down around it. The two long, side edges are then bent back out to provide two flaps parallel to the thick steel base plate. Holes for four small screws allow the two steel pieces to be attached together, with the Marinite® block housing the gauges in between. These screws are removable so the holder can be taken apart to allow access to the Marinite® block and sensors if necessary. The entire ensemble, consisting of the base plate, Marinite® block, heat flux gauges, thin plate and screws, is referred to as the sensor board. Front and back views of the sensor board are shown in Figures 2.5a and 2.5b, with a sketch of the front view showing the various sensors shown in Figure 2.5c.

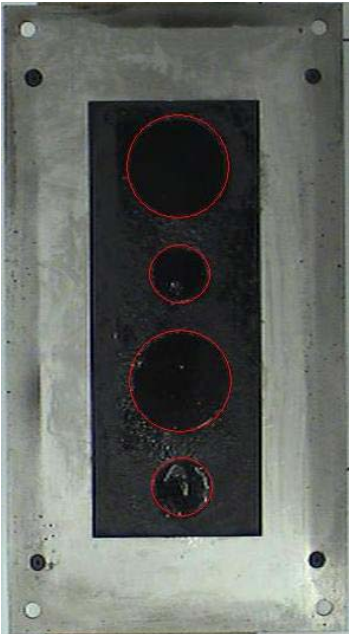


FIGURE 2.5a Front View of Sensor Board

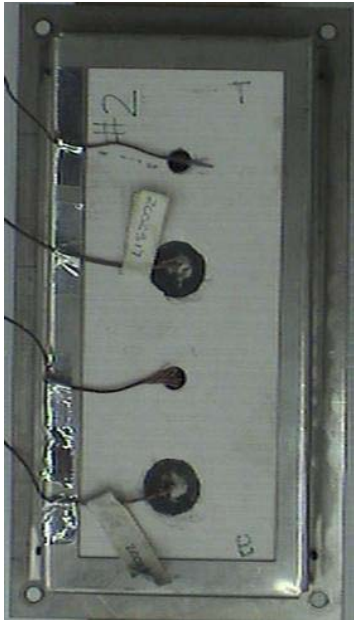


FIGURE 2.5b Back View of Sensor Board

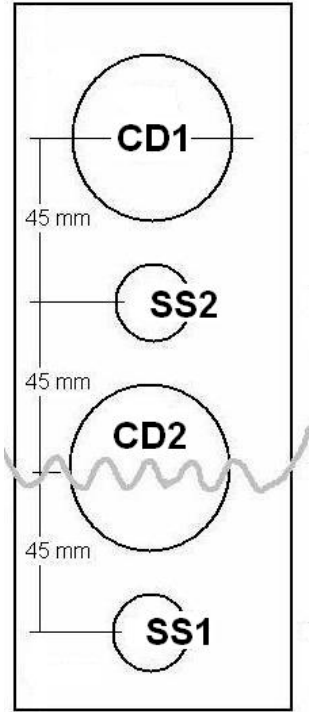


FIGURE 2.5c Schematic Front View of Sensor Board

Once assembled, the sensor board is mounted on the back of the sample card on the four large bolts. To make this possible, the sensor board has four corner holes in the base plate 10 mm in from the edges, 6 mm in diameter, shown in Figures 2.5a and 2.5b.

2.2.5 Spacers

A group of aluminium frames known as spacers are used to allow the sensor board to be placed certain distances from the back side of the fabric. This simulates how tight or loose a person's clothing fits – whether the fabric is in contact with or located a distance away from their skin. In assembling the apparatus, the spacer(s) is placed on the back of the sample card, around the four steel bolts, followed by the sensor board behind it. The aluminium spacers are a rectangle frame 6 mm wide, with rounded corners. The inside opening is 245 mm by 125 mm, allowing for some clearance around the four bolts. Aluminium was chosen for its light weight and its ability to withstand high temperatures. Spacers of three different thicknesses of $\frac{1}{8}$ ", $\frac{1}{4}$ ", and $\frac{1}{2}$ " (3.2, 6.35, and 12.7 mm) were made to allow three different air gaps to be created. If no spacer is in place the air gap distance between the back surface of the fabric and the sensor faces is 3.9 mm, due to the specimen holder, the sample card and the steel plate that the sensor board sits on. For this research, only two air gaps were used. They were 7.1 mm and 13.5 mm respectively, roughly one quarter and one half inches. The 7.1 mm air gap comes with the $\frac{1}{8}$ " (3.2 mm) spacer in place and the 13.5 mm air gap comes with the both the $\frac{1}{8}$ " (3.2 mm) and $\frac{1}{4}$ " (6.35 mm) spacers in place. It should be noted that the actual air gap between the fabric and the test sensors may change during a test due to thermal mechanical effects (eg. shrinkage) as the fabric is heated.

2.2.6 Hot Wire Ignition Source

As previously mentioned, a gas burner ignition source was not acceptable for the microgravity flight. After investigating several other ignition sources, a hot wire was chosen, as this source was previously used in experiments with the SFSF. An electrical current is passed through a wire of high resistance, causing the wire to heat up, which when placed in contact with a combustible item, will cause the item to ignite. Various metals in various wire diameters, known as gauges, are available for use as a hot wire.

For this research, a nichrome wire (Arcor Electronics, Northbrook, IL) was chosen. Nichrome is a nickel-chromium alloy. Changing the current flowing through the wire will change the temperature the wire will reach. Tables of current, voltage, resistance, and temperature for nichrome wires can be found in reference [44]. For this research 26 AWG nichrome wire was used to ignite the fabric specimens. The 26 AWG size was initially chosen as it was readily available from a local hobby store for initial testing. Through trial and error it was found that this wire ignited the fabric specimens and was within the power supply limits of the SFSF, so it was chosen for use. It was found that 5.0 A of current through the nichrome wire was sufficient to create good ignition of all four test fabrics. A higher current caused the wire to break before ignition occurred and a lower current caused the wire to simply singe or melt through the fabric with no ignition occurring. From reference [44], 5.0 A flowing through 26 AWG nichrome wire would heat the wire temperature to about 802°C, which is considerably higher than the ignition temperature of cotton (e.g. 407°C [45]).

Wires were held in place on the fabric surface by hand-stitching a new wire to each specimen using Kevlar®/PBI thread. A hot wire can be seen attached to the specimen in Figure 2.2b. Insulated wires connected to a power source are attached to

the ends of the nichrome hot wire to provide the circuit for the current to flow. For ground tests at the University of Saskatchewan, the power supply used was the LAMBDA Model LLS8018 (Lambda Electronics, San Diego, CA) with an output of 0-18 V at 24 A. The insulated wires extending from the power source were attached to the hot wire by means of alligator clips. For tests run in the SFSF, a pin and socket connection was used to connect the hot wire to the lead wires that were connected to the existing power supply in the SFSF.

2.2.7 Assembling the Apparatus

Assembling the apparatus for use involves mounting both the sensor board and the fabric specimen to the sample card. Recall that the back side of the sample card has four corner screws around the centre cut-out. The desired spacer is placed around these screws, shown in Figure 2.6a. Once the spacer is in place, the sensor board is mounted by putting the four corner holes on the board over the four corner screws on the sample card. The spacer and sensor board are then held in place by fastening a bolt to each corner screw. The back of the assembled apparatus is shown in Figure 2.6b.

The fabric specimen on its specimen holder must be mounted on the front of the sample card. Recall there are grooves for the holder to slide into place. Figure 2.7a shows the fabric specimen on its holder being slid into place on the front of the sample card. Once the specimen is in place, the hot wire igniter ends are connected to the power supply by means of alligator clips or pin and socket connectors. A front view of the assembled apparatus can be seen in Figure 2.7b.



FIGURE 2.6a Sample Card with Spacer

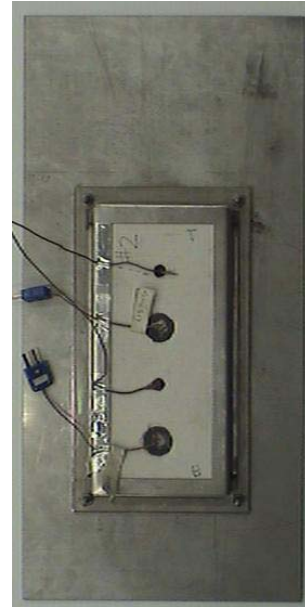


FIGURE 2.6b Assembled Apparatus Back



FIGURE 2.7a Mounting Specimen Holder on Sample Card

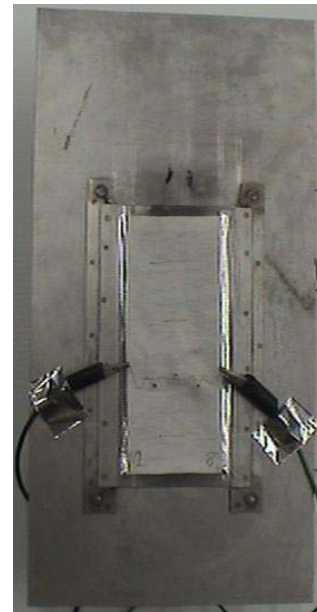


FIGURE 2.7b Assembled Apparatus Front

A schematic side view of the assembled apparatus is shown in Figure 2.8 so that all components of the apparatus can be seen together. The thin sample card is in the

middle to which everything else is mounted. On the front of the sample card is the fabric specimen taped to its holder. The hot wire for ignition is on the outer surface of the fabric specimen and is connected to the power supply by alligator clips, although the alligator clips are not shown in the Figure for clarity. On the back of the sample card is the spacer to create the desired air gap. Behind this is the sensor board, held in place by screws. Because there is a cut-out in the middle of the sample card, the back surface of the fabric is exposed to the front surface of the heat flux gauges.

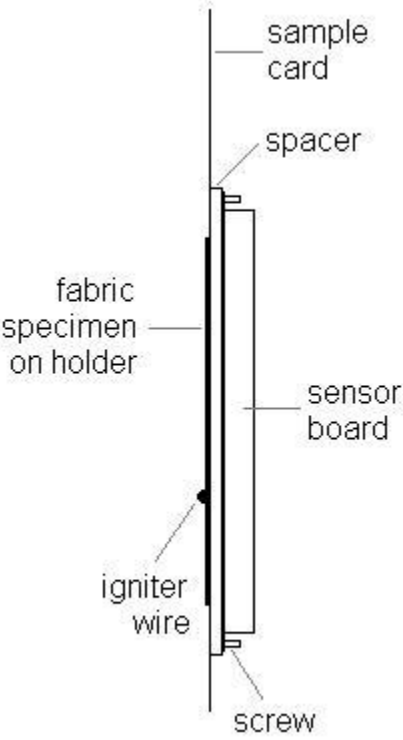


FIGURE 2.8 Schematic Side View of the Assembled Experimental Apparatus

CHAPTER 3 EXPERIMENTAL TEST PROCEDURES

The experimental work for this project was carried out in four different locations: the University of Saskatchewan in Saskatoon, SK, the University of Alberta in Edmonton, AB, NASA Glenn Research Center in Cleveland, OH and NASA Johnson Space Center at Ellington Field in Houston, TX. The first three locations were for ground testing in earth's gravity, while the latter provided access to a microgravity environment by means of a parabolic aircraft flight. This chapter will outline the types of experiments performed at each location and the procedures followed.

3.1 Edmonton Tests

During October 6-8, 2003 some preliminary work was done at the University of Alberta's Department of Human Ecology Textiles Laboratory, which is equipped to run a large number of standard and non-standard textile tests. This provided an opportunity to obtain mass and thickness data for the test fabrics using CGSB test standards and also to run some burn tests using the CAN/CGSB-4.2 No.27.10 [10] standard test apparatus which was described in section 1.1.1.

The mass of each fabric was determined according to CAN/CGSB-4.2 No.5.1-M90 [46]. Fabric samples were placed in a conditioning room at 21°C, 65% relative humidity overnight. Circles, 20 cm² in area, were die cut out of the fabric with a mallet. The circles were then weighed on a scale to determine the mass per unit area by

$$\text{mass (g/m}^2\text{)} = \frac{\text{mass of specimen (g)}}{\text{area of specimen (mm}^2\text{)}} \times 10^6 \quad (3.1)$$

The scale used was a Denver Instrument Company M-Series Analytical Balance, model #M-310 (Denver Instruments, Denver, CO). The standard stated that for five or more circles of the same fabric, they can all be weighed together and the result divided by five. For determining the mass of the test fabrics, ten circles from each fabric were used, taken from various locations throughout the fabric sample.

The thickness of each test fabric was determined according to CAN/CGSB-4.2 No.37-2002 [47]. Fabric samples were again conditioned at 21°C, 65% RH overnight. A fabric thickness tester was used, with the instructions being to lower the pressure foot onto the fabric without impact and allow it to remain at that pressure for 30 s. A pressure of 1 kPa is recommended. At least five measurements are required. The average thickness, the selected pressure, and the size of the pressure foot used must be reported. The C&R Tester Procedure – Model CS-55 from Custom Scientific Instruments, Inc. was used, which has a total applied weight of 2 oz (0.057 kg), and a pressure foot 29 mm in diameter. This corresponds to an applied pressure of 0.84 kPa. Ten readings were taken for each fabric at various locations throughout the samples.

Edmonton also provided the opportunity to work with the CAN/CGSB-4.2 No.27.10 [10] standard test apparatus, the ground-based standard the microgravity test apparatus design was based on. The standard apparatus differs from the experimental apparatus in two major ways: a gas burner as opposed to a hot wire ignition source, and pins as opposed to tape to hold the specimen in place. The tests performed in Edmonton used the gas burner as an ignition source for all, while the fabric was pinned for some tests and taped for other tests to obtain a comparison in burn behaviour.

The standard test calls for ten specimens to be tested, prepared five in the machine direction and five in the cross direction. Machine and cross refer to the direction which the specimens are cut from a test sample. The long edge of a machine cut follows the long edge of the fabric sample, while the long edge of a cross cut follows the shorter edge of the fabric sample, as indicated in Figure 3.1.

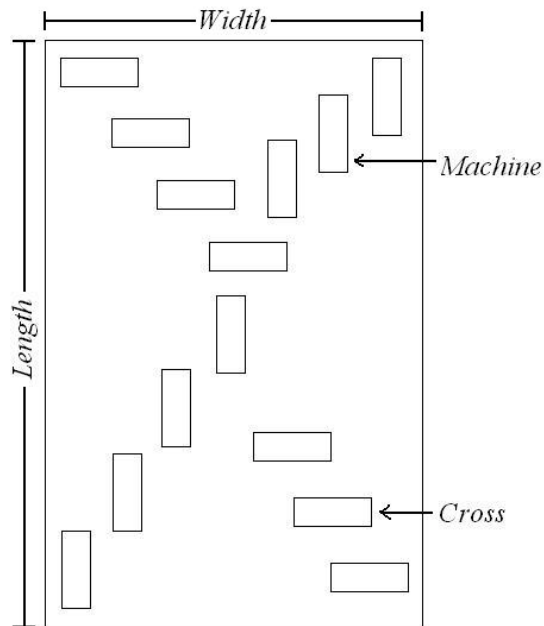


FIGURE 3.1 Directions of Test Specimens Cut From a Test Sample

It is also desirable to obtain specimens from various locations throughout the sample, trying not to overlap sampling areas if possible. All specimens cut for this research were sampled this way, with mark or cross direction recorded.

The CAN/CGSB-4.2 No.27.10 [10] test procedure calls for the specimens to be dried in an oven and cooled in a desiccator. Since this part of the procedure was unlikely to be achievable at the other test locations, this step was not included. The next

step is to light the burner for two minutes of preheating, after which the flame height is set to 40 ± 2 mm. Next the specimens are placed on the specimen holder which is placed on the frame on the support stand so the specimen's long direction is vertical, shown in Figure 3.2. Two different types of ignition are outlined in the standard. In surface ignition, the burner is perpendicular to the specimen, as in Figure 3.2a while edge ignition holds the burner at a 30° angle to the vertical, towards the lower edge of the specimen, as in Figure 3.2b. Instructions are to apply the flame for 12 seconds, watch the fabric burn, and when all combustion has stopped determine how much of the specimen is damaged. There is also a procedure outlined to determine a damaged length.



FIGURE 3.2a CAN/CGSB-4.2 No.27.10
Standard Test Apparatus – Surface Ignition

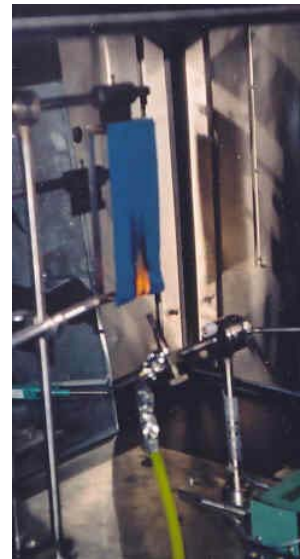


FIGURE 3.2b CAN/CGSB-4.2 No.27.10
Standard Test Apparatus – Edge Ignition

Because the fabrics tested for this research are cotton and cotton/polyester blends as opposed to flame resistant materials, nearly the entire fabric specimen is consumed by flames during the test. Therefore, it is not useful to determine a damaged length. A new, more applicable test procedure was developed. Although this research is

concerned primarily with skin burn injury, it is also concerned with determining flame spread rates. The new procedure was derived somewhat from the CAN/CGSB-4.2 No.27.3 Textile Test Methods “Vertical Flame Spread Test” [6]. It uses the same commercial grade propane gas burner as CAN/CGSB-4.2 No.27.10 [10] and calls for surface ignition, with edge ignition to be used only if surface ignition fails to ignite the specimen. This flame spread test uses a longer sample and calls for marker threads in three locations across the surface of the fabric. A weight is tied to each marker thread which will fall when the flame burns through the thread. The time from when the burner is set into place to when each weight falls is recorded. For this research, a single marker thread was placed at the top of each specimen, with a 32 g weight attached. To do this, a ring stand was placed next to the apparatus. The thread was tied to the apparatus support and directed up over the pins at the top of the specimen holder in place on the frame. From here the thread and weight hang over the ring stand to the side of the apparatus, as shown in Figure 3.3. With the ignition location being 30 mm from the base of the specimen, lines were marked on the specimen 100, 150, and 200 mm from its base to attempt to visually observe the time it takes for the flame to reach these locations.

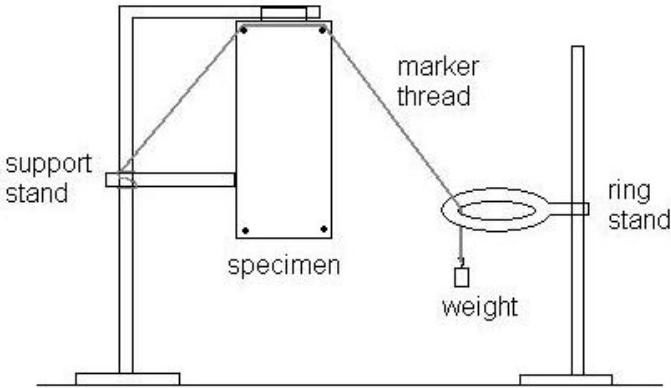


FIGURE 3.3 Schematic of Apparatus used to measure Flame Spread with a Marker Thread in Edmonton

The procedure for the Edmonton tests is as follows. First, the specimen is attached to the specimen holder by either corner pins or metallic tape. The specimen on its holder is then put in place on the support frame and the marker thread and weight are attached to the apparatus as shown in Figure 3.3. Next, the fumehood fan is turned off to achieve a quiescent environment. The propane is then turned on, the gas burner is ignited, and its flame height is set to 40 ± 2 mm.

To start the test, the burner is applied perpendicular to the specimen (as shown in Figure 3.2a), 30 mm from the specimen base, and the timer is started. Once ignition occurs, the burner is removed from the specimen surface. From this point on, burning behaviour is observed and important times are recorded. These times include the time the fabric specimen ignited, the times for the flame to reach the 100, 150 and 200 mm marked lines on the specimen, and the time the weight falls to indicate the marker thread has broken. Once the burning ceases, the propane and burner are turned off and the fumehood fan is turned on. When the specimen holder has cooled enough to touch, it is removed and the experiment is repeated with a new fabric specimen in place.

This flame spread experiment was performed for three machine and three cross cut specimens from each of the four fabrics. This was done once using the specimen holder with the corner pins to hold the specimen in place, and then repeated in its entirety using tape to attach the fabric to the holder instead, resulting in 48 tests in total.

During the final day at the University of Alberta, there was access to a battery-powered data logger. This provided the opportunity to obtain a temperature time profile using the heat flux gauges in the sensor board of the test apparatus. Data for five tests with the lightweight cotton fabric and five with the heavyweight cotton fabric was gathered. All these tests were conducted with the sensor board 7 mm from the back of

the fabric. The sensor board was oriented so a copper disk was at the bottom and the skin simulant was at the top. The data logger records non-stop and there is no real time reference. Tests have to be separated afterwards based on the temperature-time profile.

The procedure involved surface ignition of the vertical fabric specimen with the burner 30 mm from the fabric base. Once the fabric was lit, the burner was removed. Data was continuously acquired at a 0.1 s time interval. Between tests, specimens were replaced and sensors were allowed to cool to 25°C.

3.2 Saskatoon Tests

The majority of the tests performed in Saskatoon were done to provide a large amount of 1-g data using the insert designed for the microgravity flight. However, the first five tests done were similar to the Edmonton tests so the burner and hotwire data could be compared. Five tests with lightweight cotton and 7 mm air gap were performed as in Edmonton (same ignition location and sensor board orientation) with the only difference being the hot wire ignition source was used instead of the gas burner.

In tests which use the hot wire as an ignition source, the wire is attached to the surface of the fabric specimen using Kevlar®/PBI threads. These threads are flame resistant and did not break apart when subject to the heat of the wire before the fabric ignites. A wire attached to a fabric specimen is shown in Figure 3.4. The wire section is curved back and forth to cover more surface area while spanning the width of the specimen. From previous experiments it had been observed that by curving the wire to cover more surface area of the fuel, the chance of successful ignition increased. The Kevlar®/PBI thread is hand-stitched around the fabric in three locations to keep it in place.

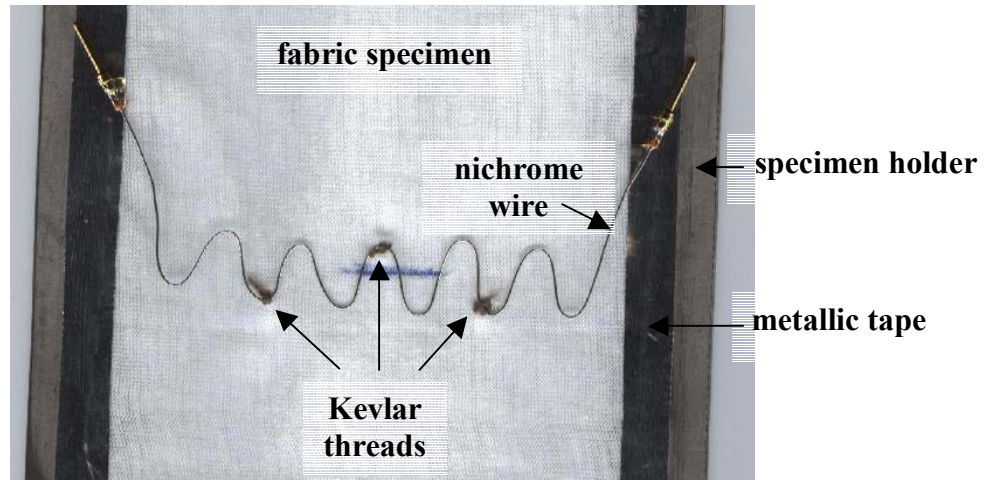


FIGURE 3.4 Igniter Wire Attached to Fabric Specimen Prior to Ignition

After a few tests were done like they were in Edmonton, tests shifted to more accurately mimic desired flight conditions. The major change was the decision to move the igniter wire to a new location, directly above the inner copper disk sensor, and flip the sensor board so a skin simulant was at the bottom and a copper disk at the top, as shown in Figure 3.5. Advantages of the new ignition location are: if the flame spread is in both directions the two skin simulants are now equal distance away from the ignition location and results from the two could be compared, and a gauge is now centred directly across from the ignition source. It is reasonable to think the flame spread could be in both directions in microgravity because in a perfect zero gravity environment with no buoyancy forces, up and down are the same just as left and right are. Along with the change in igniter location came the change in flame spread marker locations. Lines are drawn above the center of each heat flux gauge so equal flame spread distances of 45 mm are easily observed, as shown in Figure 3.5.

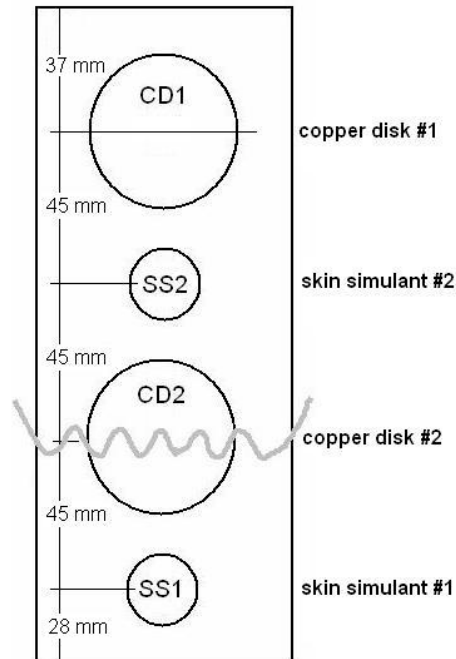


FIGURE 3.5 Heat Flux Gauge and Hot Wire Ignition Locations along the Fabric Specimen Surface

The complete experimental set-up consists of the new apparatus insert described in section 2.2, a data acquisition system and a personal computer. The data acquisition system used was the Agilent 34970A Data Acquisition/Switch Unit manufactured by Hewlett-Packard (Palo Alto, CA), connected to a personal computer, with the corresponding computer software version 1.4 entitled Agilent Benchlink Data Logger. The Agilent data logger has 300 channels for data input. For this experiment, four channels were configured to type T thermocouples. These were the channels to which the wires from the four heat flux gauges were attached. The software allowed the data to be read and plotted in real time on the computer screen. An acquisition time of 0.1 s was chosen. The four channels used do not take data at the same instant in time, but rather one after the next. Although the desired acquire time is set to 0.1 s, the actual

time step that resulted was often between 0.15 and 0.16 s. Temperature and time data could then be exported between tests to appropriate spreadsheet files on a personal computer using an RS232 60601 cable for further analysis.

Before testing begins, specimens are cut out in both the machine and cross dimensions (Figure 3.1). Lines for flame spread measurements are drawn on the specimens in locations over the centre of each heat flux gauge. A hot wire is sewn to each specimen using Kevlar®/PBI thread (Figure 3.4), 73 mm from the base of the specimen, corresponding to the centre of the middle copper disk.

Before an individual test begins, the specimen is taped to the specimen holder, which is slid into place on the apparatus. The ends of the hot wire are attached to the alligator clips that connect to wires from the power supply. The apparatus is then placed in its desired orientation (Figure 3.6), the fumehood fan is turned off to obtain a quiescent environment, and the data acquisition program for the Agilent 34970A is started. At this point one must check to ensure the gauges have cooled to 25°C or less to verify that the internal temperature gradients in the skin simulant sensors have been eliminated. Typically this takes approximately 20 minutes. For the ground tests performed, 20 minutes was allowed to elapse between tests. For the low gravity flight, two different sensor boards were used alternately so the gauges had enough time to cool down between uses.

To begin a test, the igniter power supply is turned on and the timer is started. The time and temperature of the CD2 sensor at ignition are recorded. This time is used for the flame spread rate calculations and the temperature is noted to locate the ignition point in the data file. After ignition occurs, the igniter power is turned off. Burning behaviour is observed. Times for the flame to reach the remaining three marker lines

corresponding to heat flux gauge locations are also recorded for use in flame spread calculations. Once the afterglow has ceased, the data acquisition program is stopped and the fumehood fan is turned on. The specimen is then removed and a new one is put in place for the next test to begin.

Tests were performed in three different orientations: vertical, horizontal, and flipped. The reason for this was to investigate the effect of buoyancy in different orientations on the ground, as it is not present in microgravity. The various orientations are shown in Figure 3.6.

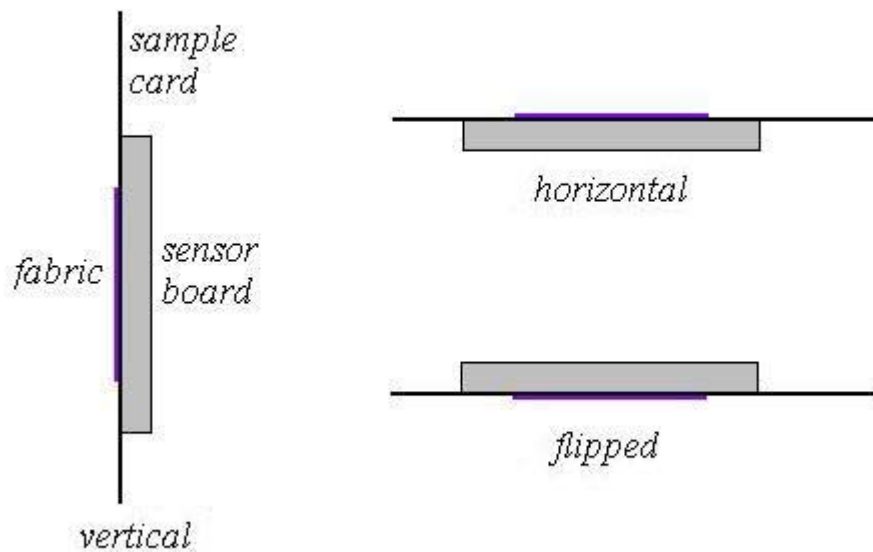


FIGURE 3.6 Various Test Orientations for the Experimental Apparatus

The vertical orientation is most similar to the Edmonton set-up, as the long axis of the fabric sample lies in the vertical direction. Changing the orientation will affect both flame sizes, flame spread rates and heat transfer, and hence skin burn injury times.

Flame spread in 1-g is largely in the upward direction, as the hot air and the flame rise, preheating the area just above the combustion zone, where the flame will quickly proceed next. For this reason, flame spread rates are expected to be much faster for the vertical orientation than for the other two orientations. Convection inside enclosures must be looked at to determine the variations in heat transfer occurring with the various orientations. The horizontal orientation is stable, as the hot surface is on top of the cooler surface, so convection currents will likely not develop. However, in both the vertical and flipped orientations, convective heat transfer is likely to occur for air gap sizes larger than the critical gap size necessary for convection to occur [48].

For the ground tests using the procedure described in this section, each of the four fabrics was tested in all three orientations, at both the 7 mm air gap and a 13 mm air gap. Each test point was repeated three times for a total of 72 tests.

A further investigation into flame spread rates at various angles of inclination was also conducted at the University of Saskatchewan for the heavyweight cotton fabric. In addition to the vertical (90°) and horizontal (0°) tests, the apparatus was placed at various other angles of inclination including 15° , 22.5° , 30° , 45° , 60° and 75° , and the tests performed as outlined above. Three tests were performed at each angle, with the sensor board being placed at the 7 mm air gap distance behind the fabric specimen.

3.3 Cleveland Tests

A trip to NASA Glenn Research Center in Cleveland from October 20-22, 2003 provided the opportunity to work with the SFSF and the new insert on the ground a final time before the flight campaign. A primary task was to ensure that the LabVIEW™

program read and recorded all desired information properly, and that tasks were being performed in the correct sequence.

Modifications to the SFSF rig and card were also completed. The thermocouple ports on the rig had already been changed from type K to type T, as discussed in section 2.2.4, and the chamber had been resealed. The new modifications included replacing the alligator clips on the card with a pin and socket connection for ease of connection and to reduce bulk. Power and thermocouple wires were taped to the card surface so they would not catch on anything during card changes or disrupt the flow. Thermocouple connectors were bolted to the top edge of the card to make the disconnection and reconnection part of the sample card change-out process faster.

While in Cleveland, the cameras were mounted in position on the rig. It was decided to have the video camera set up to view the side of the apparatus so that the IR camera could have the front view to obtain temperature data of the fabric surface during the experiments. The height of view of the video camera was determined once the sample card was positioned in the rig. The specimen was centred in the viewing windows, with the middle 100 mm of the specimen visible to the camera, as shown in Figure 3.7. This means the bottom 50 mm and top 50 mm of the specimen were out of the viewing area. The guide rails that the sample card slide into inside the combustion chamber had to be widened slightly by loosening some screws, as the new sample cards were a little thicker those used in the previous experiment.

On the final day in Cleveland, there was time for four tests to be run with the insert in the SFSF. The orientation of the sample card and sensor board in the chamber was exactly the same as the vertical orientation from the Saskatoon tests. Tests were run with the lightweight cotton and heavyweight cotton fabrics at both the 7 and 13 mm air

gaps. The gas bottle being used for flow through the chamber contained 21% oxygen and 79% nitrogen, representative of standard air. Some flow is desired to have gas in the chamber at all times for burning. These four tests were conducted with a flow velocity of 2 cm/s. Based on previous work with the rig this flow velocity was expected to have little effect on the burning behaviour, as buoyancy has been found to dominate up to a flow rate of about 9 cm/s.

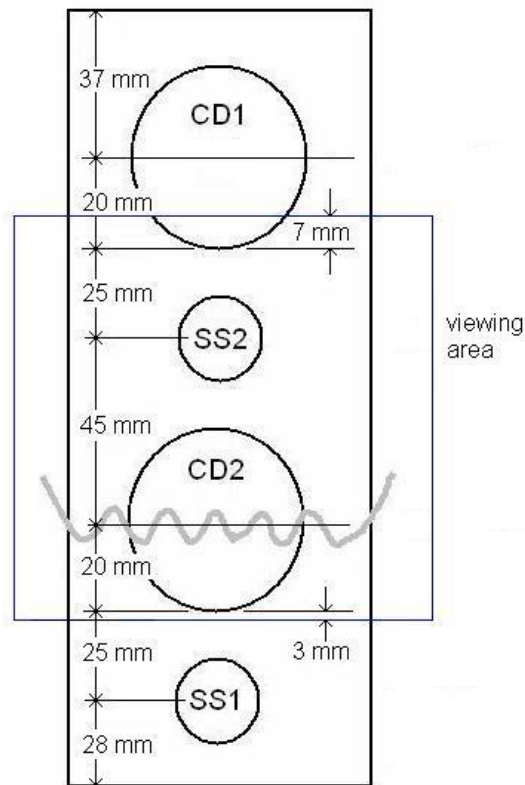


FIGURE 3.7 Field of View of the Camera on the SFSF

3.4 Houston Tests

The microgravity data for this research project was gathered during the November 3-8, 2003 flight week onboard NASA's KC-135 aircraft out of Johnson Space Center at Ellington Field in Houston, Texas. A typical flight week starts with a

Test Readiness Review (TRR) Monday morning in which all experiments are explained and the apparatuses are inspected for safety concerns. If the test rigs pass the TRR, they are loaded onto the aircraft on Monday afternoon. The flight week then consists of a single flight at 9:00 am each of the next four mornings (Tuesday through Friday). Due to technical difficulties, the four flights in this week were conducted Wednesday afternoon, Friday morning and afternoon, and Saturday morning.

A typical KC-135 flight out of Johnson Space Center consists of 40 parabolas. Each parabola provides approximately 25 s of 10^{-3} g in the middle of the loop, as shown in Figure 3.8.

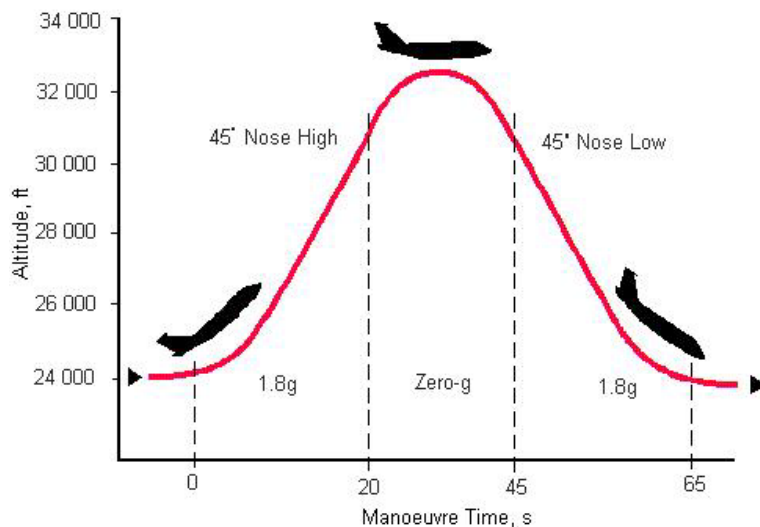


FIGURE 3.8 The KC-135 Parabolic Flight Trajectory (Source: NASA, reprinted with permission)

To achieve the microgravity, the plane first flies along horizontally and then gradually pulls up the nose to climb at an angle of 45° . During this pull-up period the plane experiences an acceleration level 1.8 times that of earth's gravity (1.8-g). When the plane reaches a certain altitude, the engine thrust is reduced to the minimal level necessary to counteract the drag force. From this point on, the aircraft is then in free fall

through the top of the parabola and weightlessness is achieved. The plane must then pull out of the manoeuvre so it does not crash. During the pull-out period, the plane again experiences 1.8-g until it straightens out into normal level flight. Gravity levels of the aircraft are recorded at all times.

The 40 parabolas in a flight are flown in groups, ten consecutively, followed by a break to turn the plane around, which often lasts about five minutes. This is repeated four times to get the 40 parabolas. Due to the nature of the combustion experiments, it is not possible to get data points during each parabola. For each test point the sample must be installed, the chamber filled with gas, and the pressure in the chamber checked to ensure it is sealed. The sample can then be ignited and the burn data obtained, with ignition needing to occur during a certain portion of the flight pattern. Following this, more gas flow is required through the chamber to ensure all flames are extinguished and the apparatus is cool enough to touch. Once the pressure is equalized, the chamber can be opened, the card removed, and a new card installed to start a new test. Based on previous experiences, it was hoped that data for ten test points per flight could be obtained, so ten specimens were prepared for each flight.

An operating procedure for the experiment was developed in conjunction with the NASA Glenn scientists performing this experiment on the KC-135 flight. It is included in Appendix A. The trickiest part of the procedure was trying to ignite the sample at an appropriate time to ensure it was burning during the microgravity portion of the test. The following was noted during the flight week. The procedure states that the igniter should be turned on 30 seconds into the pull-up. This was just a guideline, as that timing depended on the fabric type and oxygen concentration. For the best burns, igniter durations were on the order of 15 - 25 seconds and it was desirable to have the

igniter off before 0-g. The objective was to let the flame propagate 1-2 cm away from the igniter (into the center portion of the video display) before 0-g began. However, the flame propagation length was not completely consistent because of variability in the ignition. Since ignition was done before a parabola, the time reference used was "feet down" (the end of the microgravity period) on the previous parabola, so any variability in the length of the pull-up also affected the ignition. The ignition technique improved with each flight.

A test matrix is often developed to outline the tests for the entire flight week. However, since this was a new experiment, the behaviour and results were somewhat unknown, so there was freedom for changes as the flight week progressed. The plan was to prioritize the variables, plan the first flight or two, and then to see how the experiments unfolded. Test variables include fabric type, air gap, oxygen concentration, and flow velocity. There were four fabric types available for testing, two cottons and two cotton/polyester blends, as outlined in section 5.1, with the focus being on the 100% cotton fabrics for this set of tests. The two air gaps chosen to focus on were 7 mm and 13 mm. The oxygen concentration refers to the concentration of oxygen in the bottles being vented through the chamber during the experiments. The 21% oxygen, 79% nitrogen was chosen to represent standard air. As higher oxygen percentages cause an increase in flammability concerns, a 25% oxygen, 75% nitrogen mixture was also chosen, as this is the upper limit of operation on the ISS [49]. This variable is not easily adjusted as it requires an entire gas bottle change. For this reason, it was chosen to have two flights at 21% and two at 25% oxygen. The final variable of concern is flow velocity, however, in this study the major test variables were fabric type, air gap and oxygen concentration. Therefore, although changing the flow rate will have an effect on

the results it was not investigated in this particular research. The only stipulation of flow velocity was that it be a relatively low flow rate that would ensure ignition and sustained burning of the fabric specimens during the tests. The test matrix that was flown during the flight week is shown in Table 3.1. Flow velocities used ranged from 2 to 5 cm/s. The abbreviations LC, HC and LB refer to the lightweight cotton, heavyweight cotton and lightweight blend fabrics. Again, descriptions of the fabrics can be found in section 5.1.

TABLE 3.1 Flight Test Matrix

Flight	Oxygen Concentration	Air Gap	1	2	3	4	5	6	7	8	9	10
1	21%	7 mm	LC	HC	LC	HC	LC	HC	LB	LB	LB	LC
2	21%	13 mm	LC	HC	LC	HC	LC	HC	LC	LB	LB	LB
3	25%	7 mm	LC	HC	LC	HC	LC	HC	LC	LB	LB	LB
4	25%	13 mm	LC	HC	LC	HC	LC	HC	LC	LB	LB	LB

LC=lightweight cotton, HC=heavyweight cotton, LB=lightweight blend

3.5 Summary of Tests Performed

This section gives a summary of what tests were performed where and how they can be compared. The list below shows what fabrics were tested where, what data was obtained from the tests, and how many tests were performed. The flame spread tests done in Edmonton can be examined to compare results from pinned and taped specimens. The five lightweight cotton tests done in Edmonton can be compared to those done using the same set-up in Saskatoon to compare differences between tests with burner and hot wire ignition. The majority of the Saskatoon tests and the four Cleveland tests can be compared to the Houston tests done at 21% oxygen to compare tests at 1-g

and μ -g. Finally, individual Houston tests can be compared to determine the effects of increasing the oxygen concentration from 21% to 25%.

TABLE 3.2 Summary of Experiments Conducted

LOCATION	QUANTITIES MEASURED	AIR GAP SIZES	FABRICS TESTED	OTHER TEST CONDITIONS
Edmonton	Flame spread rates	No sensor board	ALL	Pinned and Taped
	Heat fluxes and skin burn times	7 mm	LC, HC	
Saskatoon	Flame spread rates	7 mm	HC	Various angles of inclination
	Flame spread rates, heat fluxes and skin burn times	7 mm, 13 mm	ALL	
	Flame spread rates, heat fluxes and skin burn times	7 mm	LC	Same set-up as Edmonton
Cleveland	Flame spread rates, heat fluxes and skin burn times	7 mm , 13 mm	LC, HC	
Houston	Flame spread rates, heat fluxes and skin burn times	7 mm, 13 mm	LC, HC, LB	21% and 25% oxygen

CHAPTER 4 TREATMENT OF DATA

This chapter will give an overview of how the data was processed to obtain the results included in chapter 5. This includes how heat fluxes and skin burn injury times were determined from the temperature-time profiles obtained from the heat flux gauges, as well as how flame spread rates were determined from the visual observations made during the experiments. The chapter also includes a discussion of changes made to the treatment of data for the microgravity portions of the tests as the 20 s time window limits the amount of data available to represent microgravity.

4.1 Flame Spread Rates

During experiments, the time at which the flames reached certain marked locations was recorded. This information was used to determine the rate of spread of the flame along the fabric with the simple formula

$$\text{rate} = \frac{\text{distance}}{\text{elapsed time}} \quad (4.1)$$

For the majority of the Saskatoon tests, times were recorded for the flame to reach a point on the fabric opposite the centre of each of the heat flux gauges based on visual observations of the tests. This distance travelled is 45 mm (centre to centre distance between gauges) and the elapsed time is simply the time it takes for the flame to progress from one gauge to the next. The time recorded for CD2 was the time at which

ignition occurred. Flame spread rates were calculated for CD2 to SS1, CD2 to SS2, and SS2 to CD1 for each test (Refer to Figure 3.6, section 3.2 for heat flux gauge names and locations). A test average was taken as the average of these three readings. An overall flame spread rate was determined for each test condition (fabric type, orientation, air gap) by taking an average of all the individual test average values.

In the vertical orientation, the flame spread at times was too fast to obtain readings at each of the designated gauge locations. Instead of a reading at CD1, a reading was sometimes taken at the top of the fabric instead, adding an extra 37 mm to the value to be used in Equation 4.1. Also, for the vertical orientation, the spread was rarely in the downward direction towards SS1, so the CD2 to SS1 flame spread rate was not included in the average value.

For the tests performed at the University of Alberta, the fabric was ignited 30 mm from the base of the sample, and flame spread times were recorded at 100, 150, and 200 mm. The times recorded were for the charred area of the fabric to reach the marker line. Flame spread rates were calculated using the previously discussed technique, with the distances adjusted accordingly.

During this portion of the research, it was found that obtaining flame spread measurements visually is, at times, a difficult task. As previously noted, the flame spread in the vertical orientation is faster than the horizontal and flipped orientations, which causes problems in obtaining accurate measurements. For the flipped and horizontal orientations, the flame front and the char edge were essentially in the same location, shown in Figure 4.1, so there was no ambiguity in the measuring point. However, the vertical tests proved harder to obtain consistent results as the flame and char front edges were not necessarily in the same location on the fabric. The main

problem that arose was that the upward shooting flames were in the same plane as the fabric specimen. From the front view, the flame could be as high as the top of the fabric specimen, but the actual base of the flame and the front edge of the charred surface were in separate locations much lower on the fabric. Another reference point used was the highest point of the broken fabric behind the flame as it progressed along the surface. This worked relatively well for the cottons, however, for the blends, the fabrics often melted first and did not break apart as the flame spread across. The three different measurement locations investigated were the flame base, the front edge of the charred fabric, and the broken fabric behind the flame, all shown in Figure 4.1 for both the vertical and horizontal orientations. As will be shown in section 5.4.2, using different measurement techniques will result in different flame spread rates.

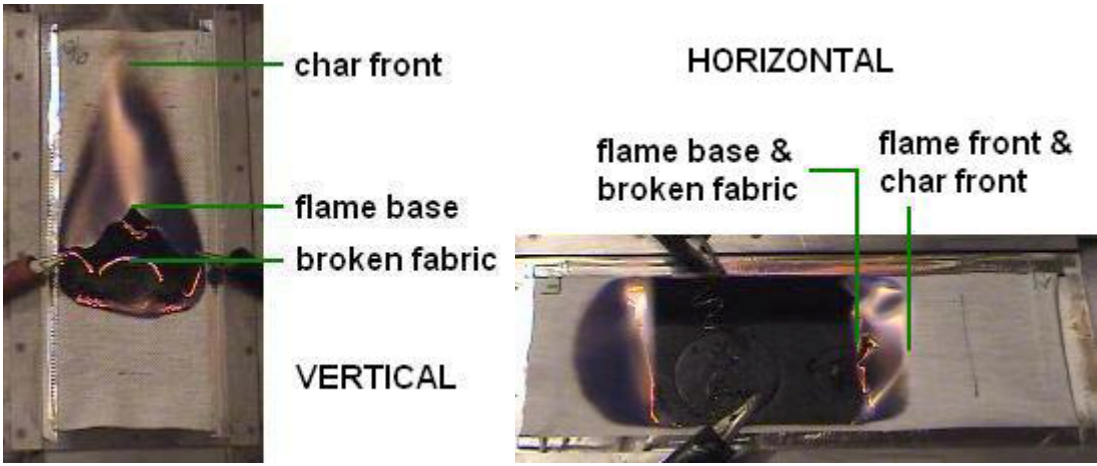


FIGURE 4.1 Reference Locations for Flame Spread Rate Measurements in the Vertical and Horizontal Orientations

It was decided to present the vertical test results from the University of Saskatchewan obtained from measuring the upward spread of the base of the flame on the fabric surface. Tests performed in the horizontal and flipped orientations had flame

spread rates measured using the flame front, which was essentially in the same location as the char front. For the tests done to investigate flame spread rates at various angles of inclination, results using all three measuring techniques (char front, flame base and broken fabric) are presented.

4.1.1 Microgravity Flame Spread Rates

Flame spread rates in microgravity were obtained visually from videos captured during the KC-135 flight. Recall from section 3.3 that the video camera had a side view of the apparatus while the IR camera had the front view and that the field of view for the cameras was essentially the middle 100 mm of the fabric specimen. To get data for the microgravity flame spread rates, the videos of the tests were viewed on a computer screen. The 100 mm tall viewing window from the rig corresponded to a 120 mm tall viewing window on the computer screen. This indicates that for every millimetre of movement observed on the computer screen, the flame actually spread 0.833 mm. It was then observed and measured on the computer screen how far the flame spread in a certain length of time during the microgravity portion of the test. The time was read off the video from the time stamp on the screen. This measured computer screen distance was converted to actual distance and divided by the elapsed time to obtain the μ -g flame spread rate for that test. A single value was obtained for each test. When measuring the flame spread rate it was observed that the flame front did not move at a constant speed. Sometimes a single flame would move quickly for a short time period, stall, and then continue to move. To try to account for this, the flame spread value was obtained over as long a time period as possible to average out the different speeds. Unfortunately spread rates were not always attainable, as sometimes the flame was too weak to appear

on the screen, or the fabric had been ignited early in the 1.8-g portion of the parabola and its middle 100 mm had already been consumed before the microgravity portion began. One thing to be aware of with this technique is that there may be a parallax error as the flame moves towards the edges of the viewing window. It should be noted that the reference location for μ -g flame spread rates was the edge of the burning fabric, which essentially corresponded to the small flame. Visual observations were made from the IR camera view, as the flames in μ -g could be rarely be seen in the side view, and the temperature data from the IR camera was not obtained from NASA for analysis.

4.2 Heat Fluxes

The heat fluxes were calculated using the temperature time data obtained from the heat flux gauges. The two different sensor types, copper disk calorimeters and skin simulants, calculate the heat fluxes in different ways. These methods are outlined in this section.

4.2.1 Copper Disk Calorimeters

The heat flux to the copper disks is calculated using the lumped heat capacity method [41]. The instantaneous heat flux at each time step is determined from the temperature time history using the following equation:

$$q''(t) = \frac{mc}{A} \frac{dT}{dt} + K(T(t) - T(0)) \quad (4.2)$$

The first term in equation 4.2 is the lumped capacity formula, while the second term accounts for the conduction losses from the back and sides of the copper disk. As

discussed in previous work by Torvi [48], for these disks the loss coefficient, K , has a value of $25 \text{ W/m}^2 \cdot ^\circ\text{C}$.

Two different approximations to dT/dt were used. The first is the common central difference approximation:

$$\left. \frac{dT}{dt} \right|_{t_m} = \frac{T_{m+1} - T_{m-1}}{t_{m+1} - t_{m-1}} \quad (4.3)$$

This method can cause fluctuation error in the data due to the resolution of the data and other factors. An alternative five point least linear squares method [50] was also used:

$$\left. \frac{dT}{dt} \right|_{t_m} = \frac{-2T_{m-2} - T_{m-1} + T_{m+1} + 2T_{m+2}}{2.5(t_{m+2} - t_{m-2})} \quad (4.4)$$

The heat fluxes calculated using the two different approximations were plotted and compared in Figure 4.2.

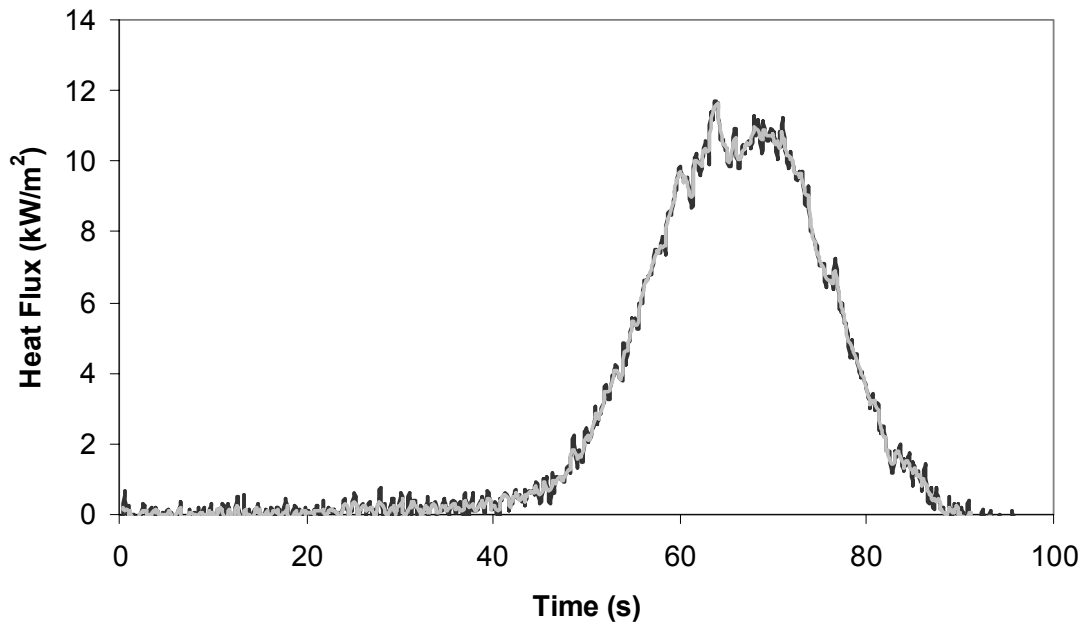


FIGURE 4.2 Heat Fluxes Calculated with the Central Difference Approximation (black) and the Five Point Least Linear Squares Approximation (grey)

Figure 4.2 indicates that the five point least linear squares approximation, indicated with a grey line, results in slightly smaller fluctuations in the calculated heat fluxes than the central difference does. For this reason, the heat fluxes determined from the copper disk calorimeters use the five point least linear squares method of approximation.

4.2.2 Skin Simulants

Assuming that the skin simulants are initially at a uniform temperature, the surface heat flux can be determined from the surface temperature data using Duhamel's theorem [51].

$$q''(t) = \sqrt{\frac{k\rho c}{\pi}} \left[\frac{1}{2} \int_0^t \frac{T_s(t) - T_s(\tau)}{(t-\tau)^{3/2}} d\tau + \frac{T_s(t) - T_i}{t^{1/2}} \right] \quad (4.5)$$

There is a singularity in this integral when $t=\tau$. To overcome this, the method of Cook and Felderman [52] was used.

The values for conductivity, density and specific heat of the skin simulants can be input into the program, or the nominal values can be used. The measured $k\rho c$ values obtained as described in section 2.2.3 ranged from a maximum of the nominal plus 17.1% to a minimum of the nominal value minus 0.23%. Using these minimum and maximum $k\rho c$ values for the same heat flux calculation resulted in differences consistently less than 10%, with the curves shown in Figure 4.3. Note that with a change in $k\rho c$ one would expect this magnitude of change in the heat flux based on equation 4.5. Times to second and third degree burns were predicted with Henriques' burn integral (section 4.2.3) for both the minimum and maximum curves seen in Figure 4.3. The predicted second degree burn times differed by 5.1% and the predicted third

degree skin burn injury times differed by 4.5%. The decision was made that the nominal kpc value would be acceptable for use in heat flux calculations.

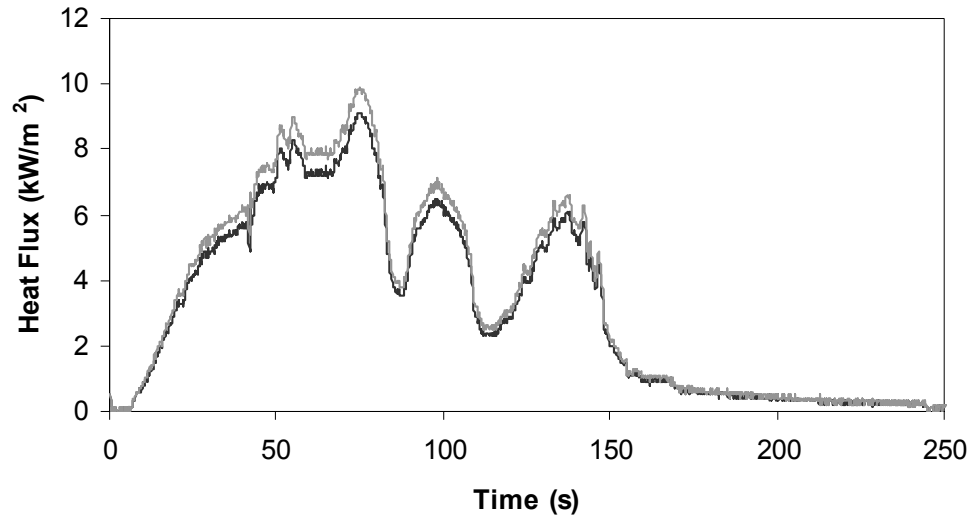


FIGURE 4.3 Heat Flux Curves using the Minimum (black) and Maximum (grey) Calibrated kpc Values

4.2.3 Effect of Sensor Types

As previously mentioned, data was obtained from two different types of heat flux gauges. The shape of the heat flux curves tend to be different for the two different sensors. Skin simulants seem to have sharper peaks than the copper disks. This was most noticeable for the horizontal orientation at the 7 mm air gap, as shown in Figure 4.4 for the lightweight cotton. For the same test, skin simulants have much higher and sharper peaks than the copper disks. While this has somewhat to do with the apparatus orientation and nature of the tests with a moving flame front, it also has to do with the different nature of the sensors being used. For the copper disk to heat up, and hence the measured heat flux to increase, the entire 18 g copper disk must be heated to the point that its temperature increases. For the skin simulant to record a change in heat flux, only

the temperature of the surface of the gauge must change. Therefore, a small fluctuation in heat flux may have more of an effect on the skin simulants than the copper disk.

Recall the copper disk sensors are 40 mm in diameter while the skin simulant sensors are only 22 mm in diameter. This size difference between the sensors can also affect the heat flux readings. The heat flux due to radiation will differ for the two gauges because the different sizes mean a different view factor. Also, because the flame is travelling across the sensor faces it has almost twice as far to go to cross an entire copper disk than a skin simulant. Since an average heat flux value is being read by each sensor, the average may be more smoothed out for a copper disk than a skin simulant because the flame is over the sensor for a longer time. This could contribute to the different shapes of the heat flux curves seen in Figure 4.4.

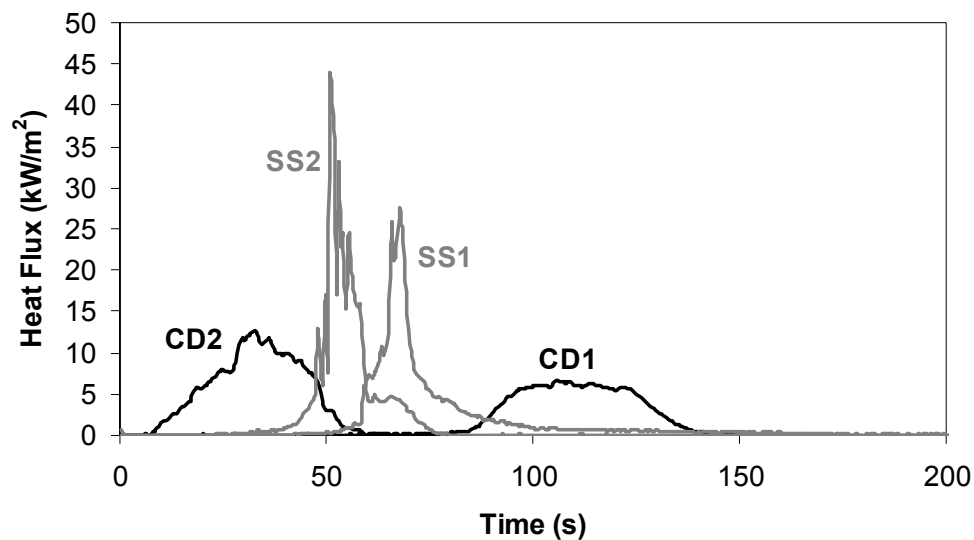


FIGURE 4.4: Heat Flux Curves from Two Copper Disk (black) and Two Skin Simulant (grey) Sensors for a Horizontal Lightweight Cotton Test at the 7 mm Air Gap

The surface temperatures of the two sensor types have noticeably different histories as well, shown in Figure 4.5 for the same test as the data in Figure 4.4. The copper disk sensors have smoother curves that are not as steep as the skin simulants. These shapes are typical of the majority of heat flux curves observed during this research. Further information on differences in measurements from these heat flux gauges can be found in Reference [21].

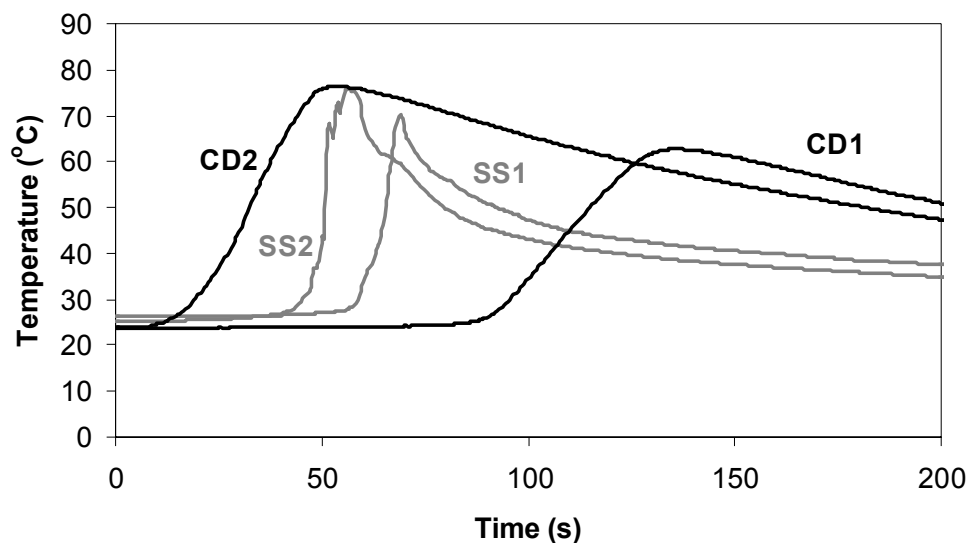


FIGURE 4.5: Temperature Curves from Two Copper Disk (black) and Two Skin Simulant (grey) Sensors for a Horizontal Lightweight Cotton Test at the 7 mm Air Gap

Up to this point, the discussion on the effect of different sensor types has concentrated on the physical and structural difference between the two sensors. However, the different analysis techniques performed on the data obtained from the sensors will also create some differences in the presented heat fluxes. To illustrate this, two sets of temperature time data were created to produce constant 15 kW/m^2 heat flux curves for the two different sensors. Following this, some temperature spikes were added to the original data to see how the different sensors react to this.

For the copper disk, a constant heat flux was created by setting the temperature-time gradient to be constant, as the copper disk heat flux formula is essentially

$$q'' = \frac{mc}{A} \frac{\Delta T}{\Delta t} \quad (4.6)$$

With a heat flux value, q'' , of 15 kW/m² and setting the time increment, Δt , the copper disk temperatures could be determined using Equation (4.6).

For the skin simulant sensors, the surfaces temperatures for a constant 15 kW/m² heat flux were determined from the semi-infinite solid heat transfer equation with a constant surface heat flux [41].

$$T - T_o = \frac{2q''}{k} \sqrt{\frac{\alpha t}{\pi}} \quad (4.7)$$

Both sets of temperature data were created using a time step of 0.5 s. Once the temperature data was obtained, some fluctuations or temperature spikes, were added to the data to see how this would affect the heat fluxes calculated by the different sensors. Temperature spikes of 0.1°C at 10 s and 0.5°C at 15 s were arbitrarily chosen. For example, if the original data set had a temperature of 52.34°C at 10 s, the new data set with temperature spikes would have a temperature of 52.44°C at 10s, an increase of 0.1°C. The heat fluxes were then recalculated with the new temperature spikes data set, with the resulting curves shown in Figure 4.6.

Figure 4.6 shows that the copper disks are more sensitive to fluctuations in temperature than the skin simulants, indicated by the larger heat flux increases on the curve. Note that the temperature spike affects the copper disk heat flux by increasing it, while the skin simulant first sees a slight increase in the heat flux followed by a slight decrease. The reasons for these different behaviours come from the mathematics used

to obtain the heat fluxes. Generally speaking, differentiation would act to make a curve rougher while integration would act to smooth out a curve. Copper disk heat fluxes are calculated using differentiation, while the skin simulant heat fluxes are calculated using integration. This effect is important, however, it is not seen in the actual experimental data shown in Figure 4.4. This indicates that the previously discussed factors of the sensors being different physically and structurally are more of a concern for this particular research.

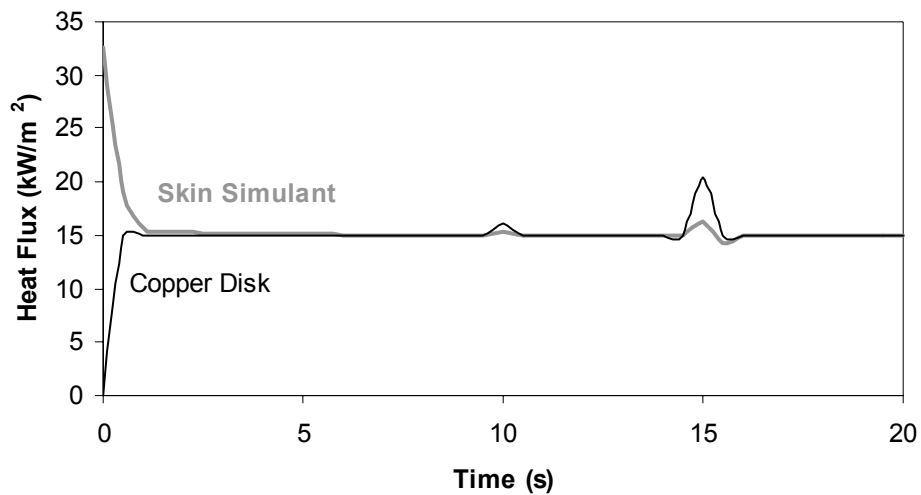


FIGURE 4.6 Constant Heat Flux Curves for the Copper Disk and Skin Simulant Sensors with a 0.1°C Temperature Spike at 10 s and a 0.5°C Temperature Spike at 15 s

4.2.4 Issues in Treatment of Data

During the course of this research different time steps were used to obtain temperature data. This was due to the various data acquisition systems used at the various test locations. Time steps used ranged between about 0.1 and 0.5 s. Changing this resolution can affect the calculation of the heat flux. To investigate this, heat flux curves were calculated and plotted for the same temperature data at two different time

steps. The original data was gathered at a time step of about 0.18 s. By taking every third data point, data with a time step of 0.54 s was also obtained. This was done for one copper disk and one skin simulant, with the results shown in Figures 4.7a and 4.7b respectively.

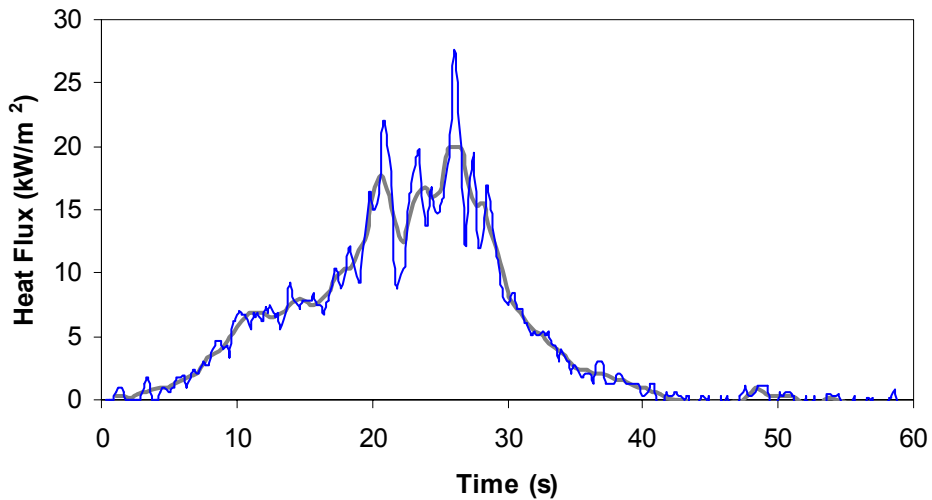


FIGURE 4.7a Copper Disk Heat Flux Data for the Same Test with Data Gathered at Time Steps of 0.18 (blue) and 0.54 Seconds (grey)

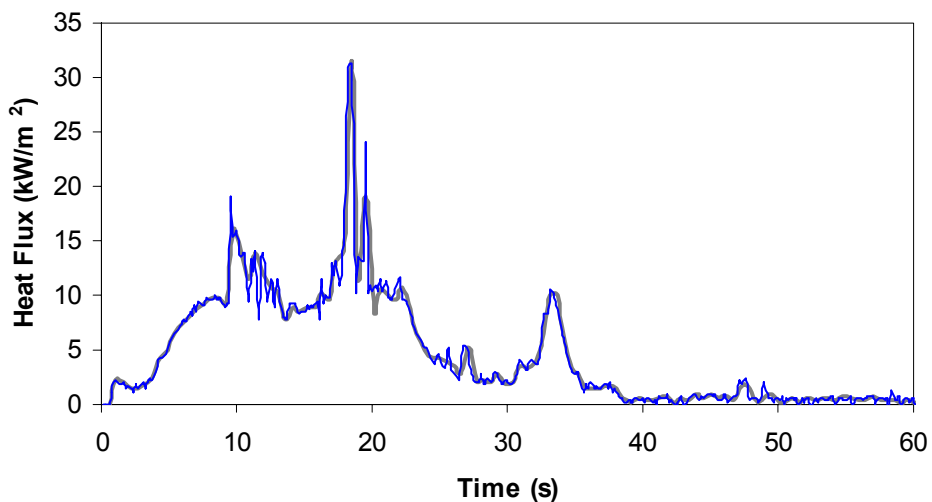


FIGURE 4.7b Skin Simulant Heat Flux Data for the Same Test with Data Gathered at Time Steps of 0.18 (blue) and 0.54 Seconds (grey)

Figures 4.7a and 4.7b show that the curves are smoother at the longer time step, with this being much more evident for the copper disk (Figure 4.7a) than for the skin simulant (Figure 4.7b). Although the longer time step creates a smoother curve, it can lose important features that are evident at the shorter time steps.

As heat flux curves created from different data with various time steps will be compared in the results chapter of this thesis, it is important to realize that some of the differences in the curves arise simply because of the different time steps used.

4.3 Skin Burn Predictions

Calculations were made to predict times for second and third degree burns to occur in human skin based on the previously calculated heat fluxes. The two different methods to predict the burn times, the Stoll criterion and Henriques' burn integral, are outlined in this section.

4.3.1 Stoll Second Degree Burn Criterion

Temperature-time data from the copper disks is used in conjunction with the Stoll second degree burn criteria to determine the time for a second degree burn to occur. Recall from section 1.2.3 that the Stoll criterion can be written in terms of the temperature rise of a calorimeter. A curve fit for a copper disk calorimeter to Stoll's data found in standards such as ASTM F1939 [14] shows that the equation for the critical temperature at any particular time is

$$T_{cr} = T_o + (8.871465 \times t^{0.2905449}) \quad (4.8)$$

This critical temperature, T_{cr} , is calculated at each time step, with T_0 being the original temperature of the sensor at time $t=0$. This initial time is set to the time when the fabric ignited. The calculated critical temperature is then compared to the measured temperature. When the measured temperature exceeds the critical temperature, a second degree burn is said to have occurred.

The Stoll criterion (equation 4.8) is graphically represented in Figure 4.8, shown in black. In Figure 4.8, the temperature data from a copper disk calorimeter is also plotted in grey. Recall that once the temperature of the copper disk (measured temperature) exceeds the Stoll criterion (critical temperature), a second degree burn is said to occur. For this example, the second degree burn occurs around seven seconds, indicated by the crossing of the two curves. To find the Stoll predicted second degree burn time for each sensor, the Stoll criterion is compared to the temperature time profile of each disk. The critical temperature is determined and the corresponding time to second degree burn is obtained.

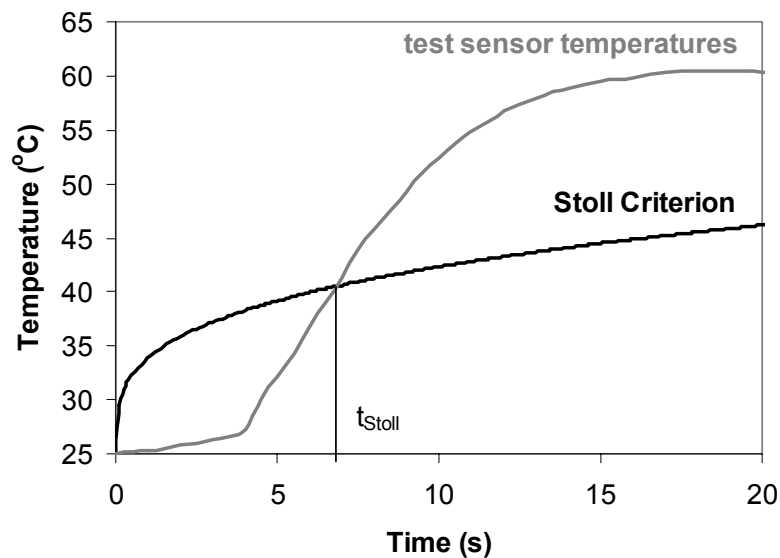


FIGURE 4.8 Test Data Being Compared to the Stoll Second Degree Burn Criterion

4.3.2 Henriques' Burn Integral

The numerical model used to calculate second and third degree burn times takes the calculated heat fluxes and then determines temperatures of the different layers of the skin. After this is complete, the model uses Henriques' burn integral to predict times to second and third degree burns. These calculations were all performed using an existing computer program written by Torvi [53].

The temperatures within the skin are predicted using Pennes' bioheat transfer equation [54]

$$\rho c \frac{\partial T}{\partial t} = k \frac{\partial^2 T}{\partial x^2} - G(\rho c)_b (T - T_c) \quad (4.9)$$

The initial and boundary conditions used to solve this differential equation are outlined below:

$$T(x, t = 0) = T_i(x) \quad (4.10)$$

where $T_i(x)$ is a quadratic initial temperature between the skin surface temperature and the body core temperature.

The first boundary condition is

$$T(x = L, t) = T_c(x) \quad (4.11)$$

which indicates the temperature of the base of the subcutaneous layer is assumed to remain constant at the body core temperature. The heat flux on the surface of the skin is used in the other boundary condition:

$$k \left(\frac{\partial T}{\partial x} \right) + q''(t) = 0 \quad (x = 0, t) \quad (4.12)$$

After these temperatures within the skin are found, Henriques' burn integral is used to estimate times to second and third degree burns of the skin. The burn integral reads as follows:

$$\Omega = \int_0^t P \exp\left(-\frac{\Delta E}{RT(t)}\right) dt \quad (4.13)$$

To predict time for a second degree burn to occur, the temperature of the basal layer (base of the epidermis) of the skin is used in equation 4.13. The equation is integrated over the time which the basal layer temperature remains above 44°C, the temperature at which thermal damage begins [18]. A second degree burn is said to occur when $\Omega=1.0$. To predict third degree burns, the same procedure is followed, however, the temperature, T, in equation 4.13 is changed to represent the temperature at the base of the dermis of the skin. More information on the model can be found in Reference [53].

4.4 Microgravity Heat Fluxes and Skin Burn Injury Times

During the KC-135 flight, data was gathered from the copper disk and skin simulant heat flux gauges and heat fluxes were calculated as in the ground tests (sections 4.2.1 and 4.2.2). Because the microgravity period is fairly short, the fabric was ignited before μ -g, namely in the 1.8-g pull-up period. This means predicting time to skin burn injury is no longer as straight forward as in 1-g.

Skin burn injury times were first calculated starting from ignition as on the ground, ignoring the gravity level. Once the burn times were predicted, the gravity levels were looked at to see if the burns occurred before, during, or after the low gravity period. It was found that predicted burn times rarely occurred during the low gravity period likely due to the higher heat fluxes in 1.8-g. Figure 4.9 shows an example of this

trend, showing the heat flux curves for both copper disks with the time to second degree burn for each indicated with a cross in the Figure. The copper disk #2 predicted second degree burn time is 6.6 s, which is before the microgravity period (7.2 to 29.2 seconds), while the predicted second degree burn time of 42.49 s for copper disk #1 is after the microgravity period.

Next, skin burn injury times were predicted using the start of the microgravity period as the reference start time. When this was done, burns again rarely occurred in the low gravity time because of the short time span and lower heat fluxes. To overcome this problem, it was decided to focus on only the heat fluxes during the low gravity period, and to calculate how long it would take burns to occur for longer duration exposures to this magnitude of heat flux (rather than only the 20 s exposure on the KC-135 flight).

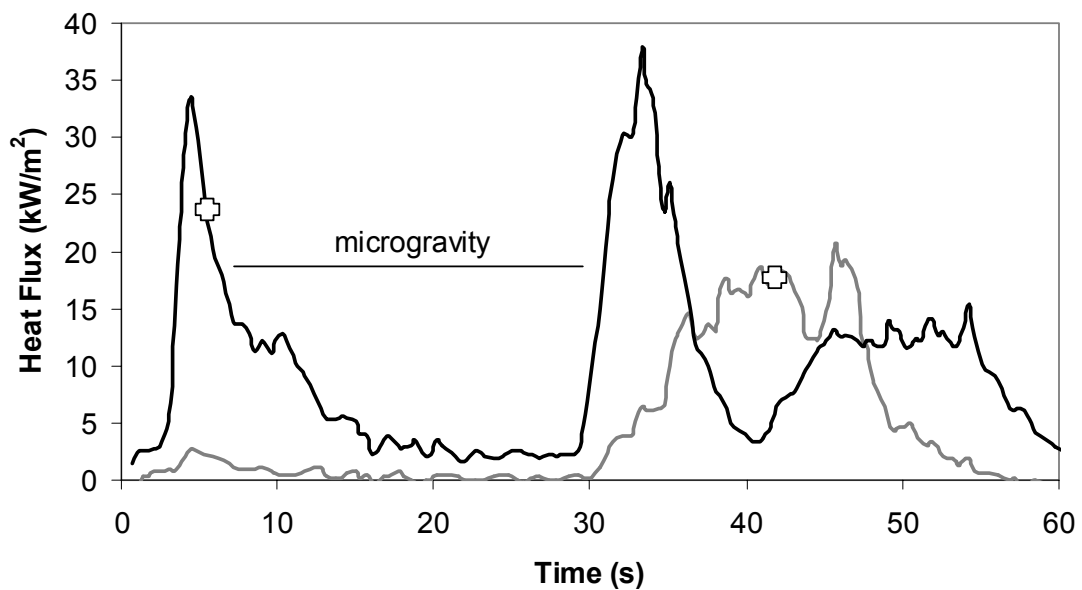


FIGURE 4.9 Heat Flux Data for Copper Disk #1 (grey) and Copper Disk #2 (black) from Test #1 of Flight #3 – Lightweight Cotton in 25% Oxygen with a 7 mm Air Gap showing Predicted Second Degree Burn Times (☒)

As previously mentioned, since ignition occurs before the 20 s microgravity period, the entire heat flux curves are not representative of only μ -g. To account for this, the entire curves were plotted with lines indicating both when the igniter was turned on and off and when the low gravity period started and ended. These time periods can vary slightly as the time for a specimen to ignite can vary and the igniter was turned off only after ignition was observed. Also the length of microgravity time during each parabola can change slightly depending on the path of the plane. The data was then replotted to focus in on this μ -g time span. Figure 4.10 shows the microgravity portion of Test #1, Flight #3: the same test as is shown in Figure 4.9, but only for copper disk #2. The microgravity time range for this test is from 7.2 to 29.2 seconds, essentially what is shown on the curve. The igniter was turned off at 11.1 s, after which time the heat flux drops off to a fairly steady value between 2 and 4 kW/m^2 .

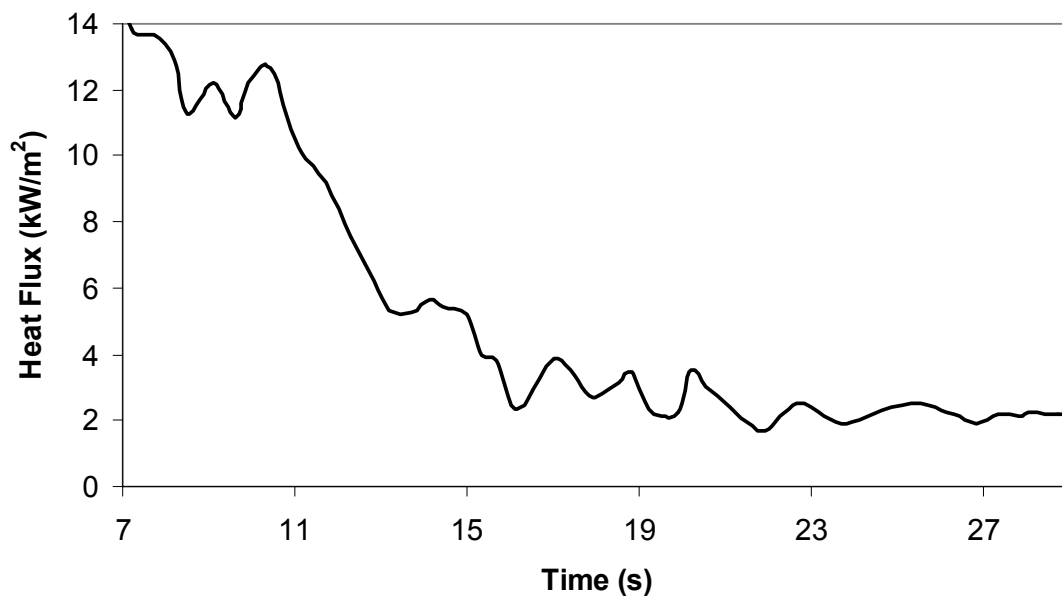


FIGURE 4.10 Heat Flux Measured by a Copper Disk Sensor during the Microgravity Portion of Test #1 from Flight #3

Figure 4.10 is typical of most flight tests, as it was found that most of the heat flux curves dropped off from a higher heat flux value in 1.8-g before levelling off through the μ -g period.

To obtain the μ -g heat flux value, a 10 s level period, often near the end of the microgravity time, was considered and the average heat flux value was calculated. For example, when finding the average heat flux for the data presented in Figure 4.10, the period from 17 s to 27 s was chosen, and the resulting value was 2.5 kW/m². An average value was calculated for each heat flux gauge for each test. It was common for a single heat flux sensor to read higher than the rest during this time, as the reduced μ -g flame size meant the flame was positioned over a single sensor and did not spread to the next sensor in the 20 second period. The average value that read the highest amongst the four sensors was then taken as the heat flux value for the test.

Having a heat flux specifically representative of the μ -g portion of the experiment provided an alternative method to predicting burn times. Because heat fluxes were low and no third degree burns were expected, the Stoll second degree burn criterion was used for its simplicity. Assuming the μ -g heat flux was a constant incident heat flux, q'' , the Stoll criterion,

$$q'' = 50.123t^{-0.7087} \quad (4.14)$$

as described in Section 1.2.3, was used to predict time to second degree burn of skin, t .

CHAPTER 5 RESULTS AND DISCUSSION

In this chapter, all experimental results will be presented. This will include flame spread rates, heat fluxes and estimated skin burn injury times. This information is presented for a variety of test conditions with variables including fabric type, type of ignition, apparatus orientation, air gap size, gravity level, and oxygen concentration in the test environment. The chapter begins with information on the fabrics tested for this research and concludes with a short chapter summary.

5.1 Test Fabrics

Four different types of fabrics were used for this research. They were obtained from Testfabrics Inc. in West Pittston, Pennsylvania. Fabrics were chosen to closely resemble clothing worn by astronauts during space missions. Regular T-shirt weight fabric and a heavier golf-shirt weight fabric were chosen. These were both ordered in 100% cotton and 50% cotton/50% polyester blend. Table 5.1 outlines the catalogue description of each fabric ordered, as well as the lot number for each fabric sample received. Throughout this research, these fabrics were referred to as lightweight cotton (LC), heavyweight cotton (HC), lightweight blend (LB), and heavyweight blend (HB) respectively.

TABLE 5.1 Information on Fabrics used for Testing

FABRIC TYPE	Testfabrics STYLE NO.	CATALOGUE DESCRIPTION	MASS PER UNIT AREA (g/m²)	Testfabrics LOT NO.
Lightweight Cotton (LC)	437W	Bleached Cotton T-shirt Fabric, Tubular	124	9729
Heavyweight Cotton (HC)	459	Bleached Cotton Knit – sport shirt weight, Tubular, Lacoste	175	9730
Lightweight Blend (LB)	7421	Polyester/Cotton 50/50 Single Knit, Tubular	140	8004
Heavyweight Blend (HB)	7439 OB	50/50 Poly/Cotton Interlock Tubular (with Optical Brightener)	None in catalogue	541-B

Once the fabrics arrived, they were all taken to Edmonton where their mass and thickness were determined in accordance with CGSB test standards as outlined in section 3.1. The results of these tests are listed in Table 5.2.

TABLE 5.2 Mass and Thickness of the Test Fabrics as determined by Standard Tests

FABRIC TYPE	MASS (g/m²)	THICKNESS (mm)
Lightweight cotton	143.6	0.43
Heavyweight cotton	175.7	0.73
Lightweight blend	129.5	0.52
Heavyweight blend	196.1	0.76

5.2 Effects of Changes to Standard Test Apparatus

This section shows how the changes from the standard test apparatus affect results. The two major changes are a hot wire ignition source instead of a burner and using tape to fasten the fabric to the holder instead of corner pins.

5.2.1 Hotwire Ignition vs. Gas Burner Ignition

Under nearly identical test conditions and procedures, experiments were run using a gas burner ignition source at the University of Alberta and then using a hot wire ignition source at the University of Saskatchewan. This was done for the vertical orientation using the lightweight cotton fabric. When using the burner to ignite the fabric, the fabric ignited about four seconds after the burner had been applied. The hot wire needs to be applied a little longer, around nine seconds, before the fabric ignites. Once ignition has occurred the burn behaviours of the tests are similar. The ignition source is removed once the fabrics are lit, and thus can no longer affect the burning taking place. Heat flux curves obtained from the two tests – one gas burner ignition and one hot wire ignition – are shown in Figure 5.1. The heat flux curves obtained from the two different ignition sources follow the same general shape, and maximum values reached are similar. Sometimes a difference was seen in the shape of the CD2 sensor curves, with the hot wire curve having a smoother rise than the burner. This may be partly due to the flickering of the burner flame.

The area under the curves in Figure 5.1 is representative of the energy being received by the heat flux sensors. By looking at Figure 5.1, it appears that the areas under the CD2 curves are similar in size, as are the areas under the CD1 curves. The maximum heat fluxes reached are 26.3 and 25.6 kW/m² for the hotwire igniter curve at CD2 and CD1 respectively. The maximum heat fluxes reached for the burner ignition curve are 25.8 and 23.6 kW/m² for CD2 and CD1 respectively. While the maximum heat flux values are not exactly the same for the two different ignition sources, they are within the range that arises for identical test conditions due to the repeatability of the tests. Perhaps a better comparison lies in the predicted skin burn injury times for these

curves. Predicted second and third degree burn times from the CD1 sensor for the burner ignition source were 29.8 and 48.2 s respectively. These are nearly identical to the corresponding times for the hot wire ignition source of 29.5 and 48.5 s. This indicates that changing the type of ignition source has little effect on predicted skin burn injury times.

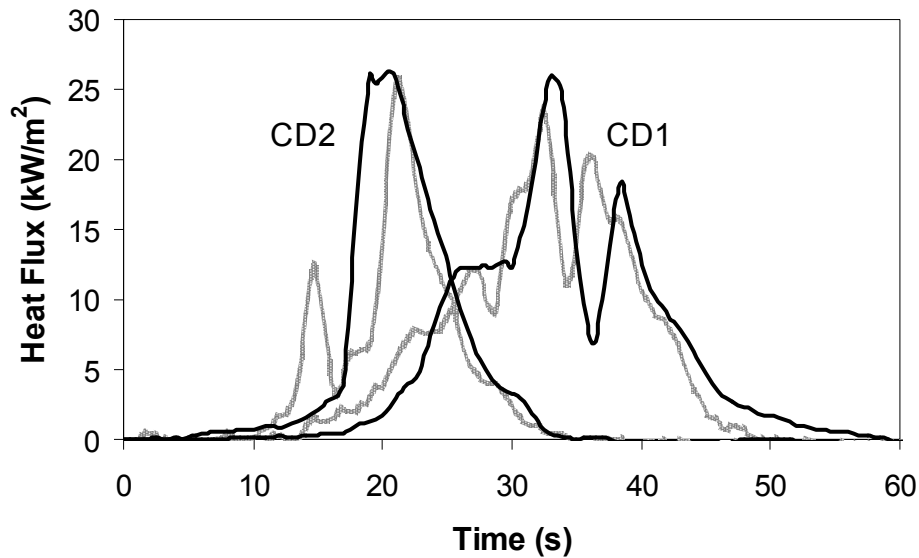


FIGURE 5.1: Heat Flux Curves from a Burner (grey) and Hotwire (black) Ignition Source Test for Two Copper Disk Sensors

5.2.2 Metallic Tape vs. Corner Fastening Pins

Flame spread measurements were obtained for all four fabrics in the vertical orientation with no sensor board in place. For half the tests the fabric specimen was attached to the specimen holder using corner pins, while the specimen edges were taped to the holder without pins for the other half of the tests. The flame spread rates obtained by observing the char front are listed in Table 5.3. Both the pinned and taped times are listed, along with a percent change to indicate how the taped value differs from the

pinned value. Generally flame spread rates were faster for the taped condition than the pinned, as indicated in Table 5.3. This was the case for all fabrics except the heavyweight blend, which had a faster flame spread rate when pinned than when taped. The faster spread rates for the taped condition arise because the fabric is fastened more rigidly in place making it quite taut compared to the corner pins attachment. With the corner pins, the fabric is only held at the four corners, while the edges are free to move. As the fabric burns, the edges can curl up towards the front burning surface. This is not the case with the tape where the edges stay attached to the holder. The cotton fabrics seem to be more affected by the change from pinned to taped specimen attachment than the blends. This could be due to the fact that the blend fabrics tend to shrink ahead of the flame while burning. This shrinking is observed for both the pinned and taped conditions and acts to lessen the effect of the constrained taped edges.

TABLE 5.3 – Vertical Flame Spread Times for Pinned and Taped Fabrics

FABRIC TYPE	PINNED (mm/s)	TAPED (mm/s)	% CHANGE
Lightweight cotton	20.90	24.86	+19.0
Heavyweight cotton	12.12	15.07	+23.7
Lightweight blend	21.16	22.51	+6.3
Heavyweight blend	14.13	12.86	-9.0

Because changing from pins to tape affects the flame spread rates, it is a noted deviation from the test standard. This is important because flame spread times also affect predicted skin burn times because if a flame moves faster along a surface, it has less time to burn the area beneath it, but also covers more area faster and may be causing skin burn injury of the larger surface sooner. For this reason, slight differences in

predicted skin burn times between the new test apparatus and the standard apparatus may arise due to the change from pinned to taped specimen attachment. Table 5.3 shows that while the lightweight blend had a faster flame spread rate for the taped condition, the heavyweight blend had a slower one. This indicates that differences between the flame spread rates of the two blends will be more pronounced for the new test apparatus (taped attachment) than if the standard test apparatus (pinned attachment) was used.

5.3 Observations of Burning Behaviours

This section gives an overview of general observations made about the burning behaviour of the fabrics in this research, complemented with photos of the burning fabrics. The burn behaviours in 1-g are discussed first, followed by comments about the μ -g burning behaviour of the fabrics.

5.3.1 1-g Burning Behaviours

Visual observations during the tests show different burning behaviour depending on both the fabric type and the apparatus orientation (orientations shown in Figure 3.7). The 100% cotton fabrics appear to burn cleaner than the 50% cotton/50% polyester blends. Smoke produced from burning blends is black compared to the light grey smoke from the cottons. This is expected as the composition of the fabrics is different, so the chemical processes undergone during burning and the combustion products released will be different. This is evidenced through their different smoke and flame colours as well as their different residues. The blends are a synthetic fabric, while cotton is natural. Flames from burning blends are generally brighter and taller than those flames from

burning cottons. When the blends are ignited they melt and drip, and larger pieces of melted fabric fall to the ground below the holder. There is often a layer of combustion products from the melted fabric left on the specimen holder after the blends are removed. Residue from burning blends is initially a hard cream coloured substance that eventually becomes darker. Cotton residue is a fine grey ash, much easier to clean afterward. Along with producing more smoke while burning, the blends also give off a stronger odour than the cottons. Burning cottons smell similar to burning paper, while the blends give off a chemical odour when burning.

Flame spread for fabrics in the vertical orientation is largely in the upward direction, with downward spread only being occasionally observed at the smaller air gap. Flame spread for fabrics in the flipped and horizontal orientations is observed equally in both the left and right directions.

Fabrics ignited in the vertical orientation are consumed the fastest, as flame spread rates are quickest. This is due to the fact that the buoyancy forces make the hot gases rise, thus heating the area just ahead of the flame base where it will proceed to next. The flames shoot up high, often past the top of the fabric specimen. For the 100% cotton tests it was observed that the flame is ahead of the char frontline on the fabric, while for the blends the flame and char are in about the same location along the surface. The blends also show evidence of shrinkage of the fabric just ahead of the flame as it proceeds along the surface. During the vertical tests, the flame first proceeds upward across the fabric surface. In some cases, after the flame has progressed to the top it will begin to burn back down the sides of the fabric and continue to burn in the downward direction, consuming the fabric below the igniter location. Images of a vertical test for one cotton fabric and one blend fabric are shown in Figure 5.2. Note that the flame

height in both cases is quite substantial, proceeding past the top of the specimen. The test in Figure 5.2a is the heavyweight cotton at the 7 mm air gap, while Figure 5.2b is the heavyweight blend at the 7 mm air gap. The pictures were taken 17 and 10 s after ignition respectively. For the vertical tests it was found that fabric type was the most dominant variable in the observed burning behaviour. Both the light and heavyweight cottons at the 7 and 13 mm air gaps had similar burn behaviours, as did the light and heavyweight blends at both air gaps. The main difference in appearance between the cottons and blends in the vertical orientation is the colour of both the smoke and the flame. As seen in Figure 5.2, the flame is bright orange and yellow in colour for the blend and a duller orange with blue highlights for the cotton. This indicates that the two fabrics burn at slightly different temperatures, but the main difference in the flame colours comes from the different products of combustion being emitted.

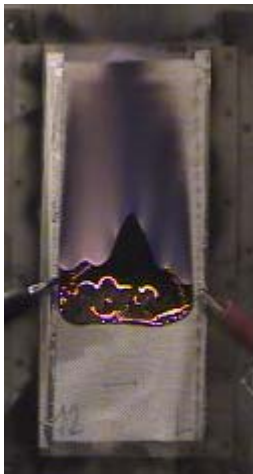


FIGURE 5.2a Vertical Test of the Heavyweight Cotton at a 7 mm Air Gap 17 Seconds after Ignition



FIGURE 5.2b Vertical Test of the Heavyweight 50/50 Cotton/Polyester at a 7 mm Air Gap 10 Seconds after Ignition

In the horizontal orientation, the flame moves across the surface of the fabric slower than in the vertical orientation. Fabrics are positioned in the horizontal plane and are ignited from the top surface. A flame is again seen on the fabric surface, however it is not nearly as tall as in the vertical orientation. As with the vertical orientation, the entire fabric is consumed and burns as the flame passes over it. The blends seem to melt ahead of the flame front while the cottons do not melt or shrink noticeably. Figure 5.3 shows the lightweight cotton burning in the horizontal orientation at both the 7 and 13 mm air gaps.



FIGURE 5.3a Horizontal Test of the Lightweight Cotton at a 7 mm Air Gap 76 Seconds after Ignition

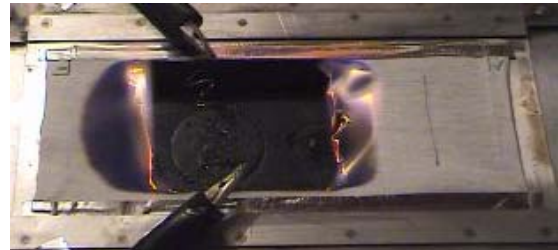


FIGURE 5.3b Horizontal Test of the Lightweight Cotton at a 13 mm Air Gap 35 Seconds after Ignition

Figure 5.4 shows the lightweight blend burning in the horizontal orientation at both the 7 and 13 mm air gap. These photos were both taken 28 s after ignition. In comparing Figures 5.3 and 5.4 it can be seen that the flame height for the blends was much greater than for the cottons and, like the vertical tests, the blends exhibit a brighter flame. Unlike the vertical orientation, the air gap also plays a noticeable role in the appearance of the flames. The flame in Figure 5.3b, at the 13 mm air gap, is larger than that at the 7 mm air gap (Figure 5.3a). The same is the case for the blend in Figure 5.4.



FIGURE 5.4a Horizontal Test of the Lightweight 50/50 Cotton/Polyester at a 7 mm Air Gap 28 Seconds after Ignition



FIGURE 5.4b Horizontal Test of the Lightweight 50/50 Cotton/Polyester at a 13 mm Air Gap 28 Seconds after Ignition

It was also observed that the weight of the fabric did not play a large role in determining the burning behaviour of the material. The heavyweight cotton exhibited behaviour similar to the lightweight cotton and likewise the heavyweight blend exhibited behaviour similar to the lightweight blend. If any difference was noted, it was that the lighter fabric had flames slightly larger than the heavier fabric, but not nearly as noticeable a difference as caused by the change in air gap previously shown.

The flipped orientation again shows a slower spread of flame than the vertical orientation, however, unlike horizontal and vertical orientations, an orange flame on the fabric surface is rarely visible for the cotton fabrics. Recall that for this orientation the fabric was lit from the bottom surface. Figure 5.5 shows the lightweight cotton fabric burning in the flipped orientation, 52 seconds after ignition. Note the flame is wide, but not tall, and blue rather than orange. Behind the flame are orange ambers where the edge of the broken fabric is located. The burning behaviour of the lightweight cotton did not change substantially with a change in the air gap.



FIGURE 5.5 Flipped Test of the Lightweight Cotton at the 7 mm Air Gap 52 Seconds after Ignition

At first glance, the burning behaviour of the heavyweight cotton seemed nearly identical to the burning behaviour of the lightweight cotton. Further investigation showed that for the heavier cotton, the fabric specimen was only charred on the first pass of the blue flame and it remained intact. Once the blue flame reached either end of the fabric specimen, the ends of the fabric caught on fire and small orange ambers would burn back across the charred fabric face, consuming the remaining fabric in the process. This two-pass behaviour of the flame was only observed for the heavyweight cotton fabric. It was not observed for the blends, as the fabric melts and a flame burns in the air gap, as will soon be discussed. It was not observed for the lightweight cotton because the fabric was thin enough that it was all consumed in the first pass of the flame. With the heavyweight cotton being a thicker fabric, there was enough material present for the two-pass behaviour of the flame to be observed. This process is illustrated sequentially in Figure 5.6 at times 42, 95, and 108 seconds after ignition. This was observed for the heavyweight cotton at both the 7 and 13 mm air gaps.

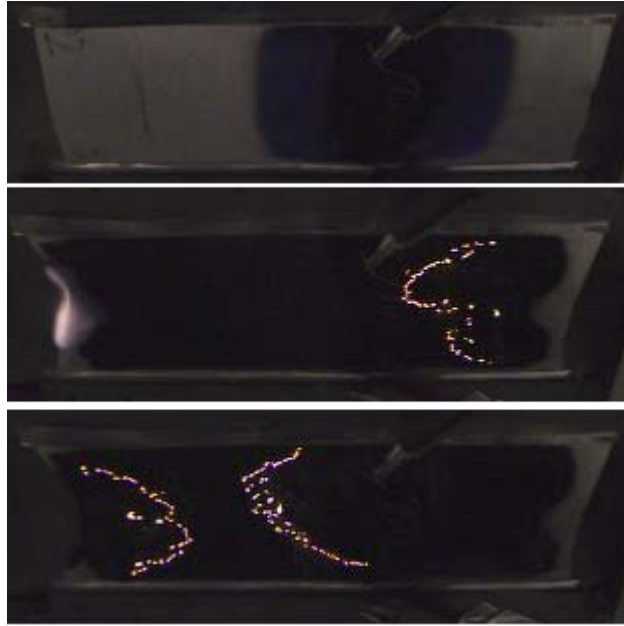


FIGURE 5.6 Various Stages of a Heavyweight Cotton Test in the Flipped Orientation at the 7 mm Air Gap obtained 42, 95, and 108 Seconds after Ignition

The blends in the flipped orientation produce the greatest amount of visible smoke of all ground tests. It collects in the air gap and seeps out between the fabric and the specimen holder at the ends. When the blends were burned in the flipped orientation, an upward orange flame was seen to be present in the air gap just behind the blue/orange flame on the fabric surface. This is illustrated in Figure 5.7. Figure 5.7 shows the heavyweight blend burning in the flipped orientation at both the 7 and 13 mm air gaps, 26 and 56 s after ignition respectively. The smaller air gap showed a wider flame on the surface of the fabric (Figure 5.7a) while the larger air gap, naturally, had a taller flame in the gap (Figure 5.7b). Figure 5.8a shows the lightweight blend in the flipped orientation at the 7 mm air gap 44 seconds after ignition, and Figure 5.8b shows the lightweight blend in the flipped orientation at the 13 mm air gap 20 seconds after ignition. The burning behaviour of blends in the flipped orientation is more dependent

on air gap than fabric weight, as the lightweight blend (Figure 5.8) burned in a similar fashion to the heavyweight blend (Figure 5.7), with the flames just slightly smaller. Again note that the blends have brighter burning flames than the cottons (compare Figures 5.5 and 5.6 with Figures 5.7 and 5.8).

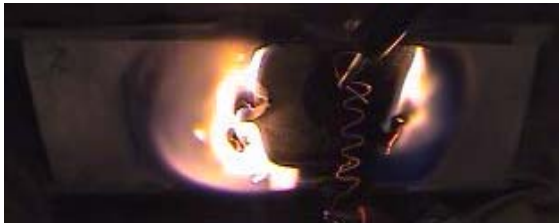


FIGURE 5.7a Flipped Test for the Heavyweight 50/50 Cotton/Polyester at a 7 mm Air Gap 26 Seconds after Ignition



FIGURE 5.7 b Flipped Test for the Heavyweight 50/50 Cotton/Polyester at a 13 mm Air Gap 56 Seconds after Ignition



FIGURE 5.8a Flipped Test for the Lightweight 50/50 Cotton/Polyester at a 7 mm Air Gap 44 Seconds after Ignition



FIGURE 5.8b Flipped Test for the Lightweight 50/50 Cotton/Polyester at a 13 mm Air Gap 20 Seconds after Ignition

5.3.2 Microgravity Burning Behaviour

Fabrics were ignited before the microgravity period during which time the burning behaviour was similar to the vertical 1-g tests. After the transition to microgravity, the size of the flame diminished substantially due to the lack of buoyancy forces. From the infrared camera front view it was observed that there ceased to be a continuous flame front across the surface of the fabric, as had been the case in 1-g. This is shown in Figure 5.9. During the low gravity portion, small flames flickered and

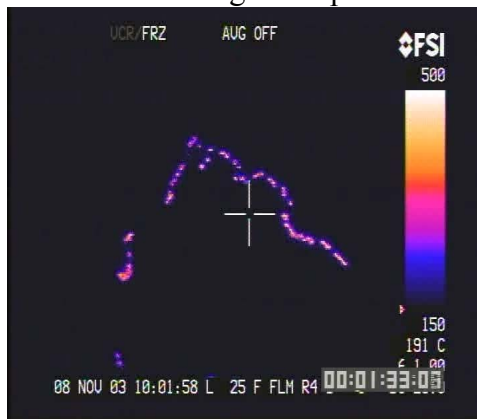
movement was observed in all directions. Once the microgravity period ended and the gravity level transitioned back to 1.8-g, the flame again grew in size and a full flame front was observed across the face of the fabric, as shown in Figure 5.9.



IR view – 1.8g Pull-up Period



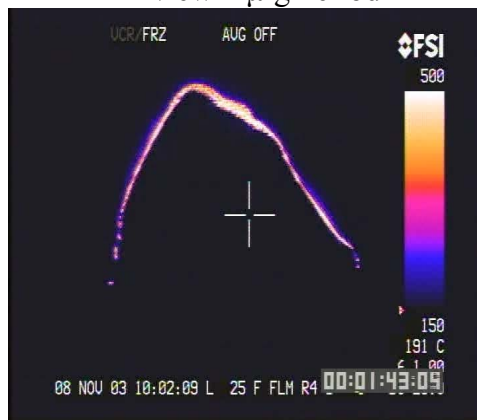
Side View – 1.8g Pull-up Period



IR view – μ -g Period



Side View – μ -g Period



IR view – 1.8g Pull-out Period



Side View – 1.8g Pull-out Period

FIGURE 5.9 Infrared and Video Camera Views of the Heavyweight Cotton at the 13 mm Air Gap in 25% Oxygen obtained 9, 31 and 41 Seconds after Ignition

During the first two flights at the 21% oxygen concentration it was observed that the blends were not igniting as well or producing as large flames as the cottons. Flow velocities were adjusted to try to obtain better burns. At the higher oxygen concentration, this did not seem to be a problem. The higher oxygen concentration caused a lot more burning to take place as nearly the entire fabric specimen was consumed during such a test.

5.4 Flame Spread Rates

This section presents and discusses the flame spread rates measured throughout this research. Results from ground tests at three main orientations of interest (vertical, flipped and horizontal) are presented first, followed by results at various angles of inclination in between the horizontal and vertical orientations. These ground test results are followed by the microgravity results.

5.4.1 Flame Spread Rates in 1-g

The results presented here were obtained by visually observing the spread of flame across the fabric, as described in section 4.3. Table 5.4 lists the average flame spread rates obtained for each fabric at each of the three main orientations studied. Flame spread is controlled by the mechanism by which heat is transferred ahead of the burning zone [55]. The vertical flame spread rates were found to be the fastest. This is because the flame and the hot gases rise in the same direction creating high rates of heat transfer ahead of the flame base. Since the area ahead of the flame is preheated, the flame will quickly proceed to this location.

Generally the flipped flame spread rates were found to be faster than the horizontal rates. One reason is that the flipped orientation involves igniting the fabric from beneath, so the flame is on the bottom side of the fabric specimen, while in the horizontal orientation, the flame sits on top of the specimen. Thus, when the hot gases rise in the horizontal orientation, they are being carried away from the specimen and do not help transfer a significant amount of heat ahead of the burning zone. The exception to this is that for the cottons at the 13 mm air gap the horizontal flame spread rate is faster than the flipped. One reason for the horizontal flame spread rate being faster than the flipped in this case could be that the flame for the cotton in the horizontal orientation with a 13 mm air gap actually has a height of about 5 cm as compared to only about 3 mm for the flipped case (Figures 5.3b and 5.6). This extra size in the flame could be enough to transfer heat to the region ahead of the flame base so that the flame spread becomes faster than the corresponding flipped case.

TABLE 5.4 Flame Spread Rates at Various Orientations

FABRIC TYPE	VERTICAL (mm/s)		FLIPPED (mm/s)		HORIZONTAL (mm/s)	
	7 mm	13 mm	7 mm	13 mm	7 mm	13mm
Lightweight Cotton	4.3	4.6	1.1	1.1	0.9	2.1
Heavyweight Cotton	3.2	3.6	0.9	1.0	0.6	1.2
Lightweight Blend	5.3	5.7	2.3	2.7	1.1	2.4
Heavyweight Blend	3.5	4.1	2.3	1.7	0.7	1.3

The flow of hot gases in the air gap is a factor that affects flame spread rates. The heated air is entrained in the air gap between the fabric and the sensors; however, this area is not completely sealed because of the porous nature of the fabric, the

breakage of fabric during burning, and the short ends of the specimen not being taped to the specimen holder. This air flow can either aid or hinder the flame spread by affecting the preheating of the fabric ahead of the flame front. The size of the air gap will also play a role in determining how the flow of hot gases affects the flame spread rate.

The fastest flame spread was 5.7 mm/s for the lightweight blend at the 13 mm air gap in the vertical orientation. The slowest flame spread rate was 0.7 mm/s for the heavyweight blend at the 7 mm air gap in the horizontal orientation. While the slowest vertical spread rate was 3.2 mm/s, the fastest flipped and horizontal times were only 2.7 and 2.4 mm/s respectively. Recall from section 4.3 that for the vertical tests, the flame base was used as the reference point for flame spread measurements, and the char front was used for the horizontal and flipped orientations. The char and flame front are essentially in the same location for the horizontal and flipped orientations, however, for the vertical orientation, the char front spreads much faster than the flame base, so the vertical times presented in Table 5.4 are actually the slower of the two vertical measurement techniques.

For the same fabric type, the lighter fabric had a faster flame spread rate than the heavier one. This is due to the fact that there is less material to be consumed and that there is a smaller mass of material at the surface that needs to be heated to allow the flame to spread. For thermally thin fuels, the flame spread velocity, V has been found to be inversely proportional to the product of the fuel's density (ρ), specific heat (c), and thickness (τ), as follows [55]:

$$V \propto \frac{1}{\rho c \tau} \quad (5.1)$$

A thermally thin approach can be used if the Biot number is less than 0.1. The thickest fabric tested had a thickness of 0.76 mm. Assuming a convective heat transfer coefficient of 20 W/m^2 (half that of a large laboratory burner flame [21]) and a typical value of thermal conductivity for a fabric ($0.06 \text{ W/m}^\circ\text{C}$), gives a Biot number of 0.25. As this is only slightly larger than 0.1, it indicates that a thermally thin approach should be reasonable for making estimates of flame spread rates.

Assuming the specific heats are the same for the two cotton fabrics, and again the same for the two blends, the flame spread rate is essentially inversely proportional to the product of the density and thickness, which is the mass per unit area. To test this relationship, the velocity and mass of the lightweight material was used in conjunction with the mass of the corresponding heavyweight material to predict the flame spread rate. Using the fabric mass per unit area in Table 5.2 and Equation (5.1), the flame spread rate of the heavyweight cotton should be 82% of the flame spread rate of the lightweight cotton. Similarly, the flame spread rate of the heavyweight blend should be 66% of the flame spread rate of the lightweight blend. In most cases, the flame spread rates predicted using this approach were within 10% of the measured flame spread rates in Table 5.3. For example, for the blends in the vertical orientation at the 7 mm air gap 66% of 5.3 mm/s (the measured lightweight blend value) is 3.5 mm/s, which is the measured heavyweight blend value. For the cottons in the flipped orientation at the 7 mm air gap, 82% of the measured lightweight flame spread rate of 1.1 mm/s does indeed predict the measured heavyweight flame spread rate of 0.9 mm/s. The difference between the predicted and measured flame spread rates was the largest for the blend in the flipped orientation at the 7 mm air gap, the test case discussed in the next paragraph.

The only case in which the flame spread rate was not faster for the lighter fabric was the heavyweight blend at a 7 mm air gap in the flipped orientation. Under these burning conditions, the flame for the heavyweight blend was observed to occupy more surface area on the fabric than the lightweight blend, as shown in Figures 5.7a and 5.8a. Since the flame has a larger surface area, it produces a higher heat flux to preheat the area ahead of the flame, which will increase the flame spread rate of the heavyweight blend, so as to be comparable to the lightweight blend.

The flame spread rates at the 13 mm air gap are generally faster than those at the 7 mm air gap for all cases except the heavyweight blend in the flipped orientation. Again, this is likely due to the phenomena discussed previously: the flame size at the 7 mm air gap on the heavyweight blend (Figure 5.7a) is larger than, in this case, the flame size on the heavyweight blend at the 13 mm air gap (Figure 5.7b). Observing that flame spread rates increase as the air gap size increases is consistent with previous GIRCCF work [40]. Reasons for a faster flame spread rate at a greater air gap are there is increased air supply to aid the combustion process and there is reduced heat loss to the cooler sensor board, as it is now further away. Table 5.4 shows that the cottons in the flipped orientation are not largely affected by air gap size, as the flame spread rates are barely higher at a 13 mm air gap than at a 7 mm air gap. This is not surprising if one compares Figures 5.5 and 5.6 and sees that the burning behaviour of the heavyweight cotton at the 7 mm and 13 mm air gaps are very similar.

Changes in air gap size have the largest effects on flame spread rates in the horizontal orientation. In the horizontal orientation, the flame and products of combustion will not be trapped in the air space below the fabric, so there will be more oxygen in the air space to support combustion. In addition, heat losses across the

horizontal air space will be smaller because convection cannot occur since the fabric, the hotter surface, is above the cooler sensor board. Having a faster flame spread rate at the 13 mm air gap may again be due to the larger flame that could preheat the area ahead of the flame, enhance the heat transfer there, and thus create a flame spread rate faster than that at 7 mm where the flame is smaller and gives off less heat. Figure 5.3 and 5.4 clearly indicate that for the horizontal orientation, flame sizes are much larger at 13 mm than at 7 mm.

In all orientations, the blends had faster flame spread rates than cottons of similar weight, which is again consistent with the GIRCFF work [40]. This is because different fabric compositions experience different chemical reactions while burning that involve different amounts of energy. For example, the peak heat release rates per unit area of sample of a cotton and a blend of comparable weights are 109 and 147 kW/m² respectively [56]. For the vertical and horizontal orientation, the order of flame spread times from fastest to slowest was lightweight blend, lightweight cotton, heavyweight blend, heavyweight cotton. This can be explained on the basis of fabric weight and fabric types, as the lighter fabrics have faster flame spread rates than the heavier fabric and the blends have faster flame spread rates than cottons of similar weight. For the flipped orientation, again the blends have a faster flame spread rate than the cotton, but this time both blends were faster than both cottons, indicating that flame spread rates in the flipped orientation may be more dependent on fabric type.

5.4.2 Flame Spread Rates at Various Angles of Inclination

Tests were done in 1-g for the heavyweight cotton fabric with a 7 mm air gap for various angles of inclination between the horizontal and vertical orientation. The results are illustrated in Figure 5.10. Recall from section 4.3 that there was difficulty in measuring flame spread rates when the char front edge and flame base were not in the same place. Figure 5.10 not only illustrates the flame spread rates at different angles, but also shows the flame spread rates obtained using various measurement techniques. The three different reference points for measurement were the top of the charred part of the fabric, the base of the flame on the fabric, and the broken portion of the fabric as it breaks apart after the flame has passed. Recall these measurement locations were discussed in section 4.3. The char moves the fastest, with the flame base and the broken fabric having similar results in speeds. In the previous section, the flame base was used for the vertical orientation results, while the charred fabric front was used for the horizontal and flipped orientations.

Figure 5.10 indicates that as the angle of inclination is increased from 0° (horizontal orientation) to 90° (vertical orientation), the flame spread rate increases. It is relatively constant until around 22.5° after which it increases substantially before beginning to level off again. Reasons for these changes are the changing interaction between the flame and the unburnt fabric as the angle changes.

Flame spread generally can be classified as concurrent, when the spread direction is the same as the direction of air flow, or counter-current, when the flow of air is opposed to the direction of spread. Concurrent flow generally creates faster flame spread rates than counter-current flow. In the absence of an imposed air flow, the air movement is developed naturally. Thus, for the case of upward flame spread on a

vertical surface, naturally induced concurrent flow is seen, as the hot air is moving upward in the same direction as the flame. For the case of flame spread across a horizontal surface in an otherwise still environment, naturally induced counter-current flow is developed. What is observed then in Figure 5.10 is that for the heavyweight cotton at a 7 mm air gap, at an angle of somewhere around 22.5° the flow changes from counter-current to concurrent and thus, the flame spread rate begins to increase.

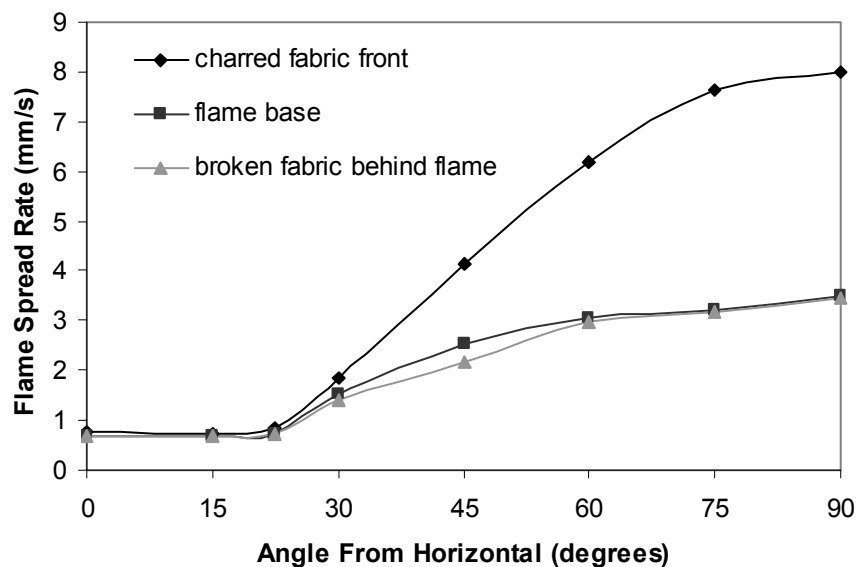


Figure 5.10 Flame Spread Rates at Various Angles of Inclination for the Heavyweight Cotton Fabric at a 7 mm Air Gap

A previous study investigating flame spread on inclined surfaces [57] indicated that there is a clear difference between the mechanisms of flame spread for thin and thick fuels. For thick fuels, a change in mechanism was found to occur at an angle of inclination between 15° and 20°, with the change in slope being enhanced if entrainment of air from the sides is restricted. Figure 5.10 indicates that for this research, a change in mechanism takes place somewhere between 22.5° and 30°, evident as the large increase

in slope of the curve. While the heavyweight cotton fabric can be treated as a thin fuel, it seems to exhibit the behaviour of a thick fuel for its flame spread rates at the lower angles. Reasons for this are that it is near the upper limit of fuels classified as thin, so will begin to behave more like a thick fuel, and that there are indeed side walls on the apparatus so the entrainment of air is restricted and the effect enhanced. Often for thin fuels, the specimen is seen to burn on both the front and back surface, while the thick fuels only burn on one side. In this experiment, the sensor board was in place behind the fabric causing the burning to be mainly on the top surface as is the case for a thick fuel.

5.4.3 Flame Spread Rates in Microgravity

Flame spread rates in microgravity were obtained from the videos of the flight tests, as outlined in section 4.4.2. Unfortunately, data was not able to be gathered from all the tests because at times the flame front could not be seen clearly enough to obtain an accurate reading. The average flame spread rates found for the cotton fabrics under the various flight test conditions are shown in Figure 5.12. They range from a low of 0.6 mm/s for the heavyweight cotton at a 7 mm air gap in 21% oxygen to a high of 1.3 mm/s for the lightweight cotton at a 7 mm air gap in 25% oxygen. It can be seen from Figure 5.11 that the μ -g flame spread rates are affected more by oxygen concentration than by air gap size or fabric weight. Faster flame spread rates are observed in the enriched oxygen environment because an increase in oxygen speeds up the combustion process. From Figure 5.11 it can also be seen that the lightweight cotton has a slightly faster flame spread rate than the heavyweight cotton under the same conditions, as in the ground tests. This is again because there is a smaller mass of material that needs to be heated to allow the flame to spread. Notice that at the 13 mm

air gap, 21% oxygen test environment, the difference in flame spread rates between the two cottons is very small, likely due to the limited number of data points, as a flame spread rate was obtained from only one heavyweight cotton test under these conditions.

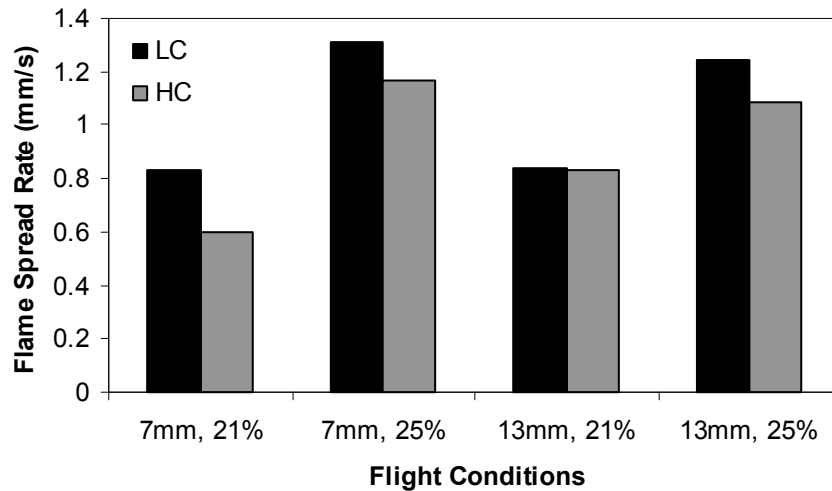


Figure 5.11 Microgravity Flame Spread Rates for the Lightweight (LC) and Heavyweight (HC) Cotton Fabrics at 7 and 13 mm Air Gaps in 21 and 25% Oxygen

The average flame spread rates from μ -g and 1-g are compared in Table 5.5 for the three fabrics tested on the flight – the two cottons and the lightweight blend. At the 7 mm air gap, the μ -g flame spread rates are comparable to the 1-g flame spread rates from the horizontal orientation. These values are nearly identical for the two cottons. At the 13 mm air gap, the cotton μ -g flame spread times are closest to the 1-g flipped times. The blend fabric at the 13 mm air gap in μ -g had a much slower flame spread time than any of the orientations in 1-g. Note that for the lightweight blend fabric the μ -g rates are slower than both the cottons, but they were faster for the 1-g test results. The cottons seem to have μ -g rates comparable to those on the ground in the certain orientations while the lightweight blend experienced slower flame spread times in μ -g. In comparing the values in Table 5.5, one must keep in mind the repeatability of a single

test. Due to the behaviour of fire, variations flame spread values from tests of the same kind can be as great as the variations between some of the different test cases in listed in the Table. For example, for the flame spread rate in the horizontal orientation for the lightweight cotton at the 7 mm air gap ranged from 0.83 to 0.98 mm/s. This is a difference of 0.15 mm/s, which is greater than the 0.1 mm/s difference between the μ -g value (0.8 mm/s) and the horizontal orientation value (0.9 mm/s) for the lightweight cotton at the 7 mm air gap. In general, the individual flame spread rate values for the horizontal and flipped orientation tests were between 3% and 20% different than the average values presented in Table 5.5. For the faster flame spread rates of the vertical orientation this percent difference was seen to increase slightly.

TABLE 5.5 Comparisons of Microgravity and Normal Gravity Flame Spread Rates

FABRIC TYPE	7mm Air Gap Rate (mm/s)				13 mm Air Gap Rate (mm/s)			
	μ -g	H	F	V	μ -g	H	F	V
Lightweight Cotton	0.8	0.9	1.1	4.3	0.8	2.1	1.1	4.6
Heavyweight Cotton	0.6	0.6	0.9	3.2	0.8	1.1	1.0	3.6
Lightweight Blend	0.5	1.1	2.3	5.3	0.4	2.4	2.7	5.7

H=1-g horizontal, F=1-g flipped, V=1-g vertical

The fact that some microgravity flame spread results are most similar to the horizontal 1-g orientation while others are most similar to the 1-g flipped orientation demonstrates that it is difficult to find a single 1-g test orientation that is representative of the behaviour in μ -g. While other researchers have been using the flipped orientation to represent μ -g behaviour [33], those experiments, unlike the ones in this research, also use air flow as an experimental variable in 1-g.

5.5 Heat Fluxes

Heat flux curves were calculated from copper disk and skin simulant temperature data, as outlined in sections 4.1.1 and 4.2.1, for vertical, horizontal and flipped ground tests as well as microgravity flight tests. In this section, ground test heat fluxes will be presented and discussed, followed by microgravity heat fluxes.

5.5.1 1-g Heat Fluxes

Plots containing the heat fluxes calculated for each of the four sensors were developed for each test. An example is shown in Figure 5.12. This is a lightweight cotton test with a 7 mm air gap in the flipped orientation. The first peak, CD2, corresponds to the sensor over the ignition source. The flame then progresses to the skin simulants (SS2 and SS1) which are located on either side of the ignition point. The final peak, CD1, is the gauge the furthest away from the ignition point. The distances between heat flux peaks show the nature of the spread of flame across the fabric during the testing. Note that the peak heat flux values in Figure 5.12 range anywhere from 11 to 29 kW/m², with the SS1 peak being substantially higher than the other three. Sharp peaks such as the one in the SS1 sensor data can arise because of the flickering of the flames caused by air movement in the test environment or a combustion reaction taking place. It is also worth noting that the heat flux curves can provide an alternative method for calculating flame spread rates. For example, the peaks of the two copper disk heat flux curves in Figure 5.12 are approximately 80 seconds apart in time. Since the distance between the two copper disks centres is known to be 90 mm, the flame spread rate can be calculated. This method gives a flame spread rate of 1.1 mm/s, the same

value listed in Table 5.5 for the lightweight cotton in the flipped orientation at the 7 mm air gap.

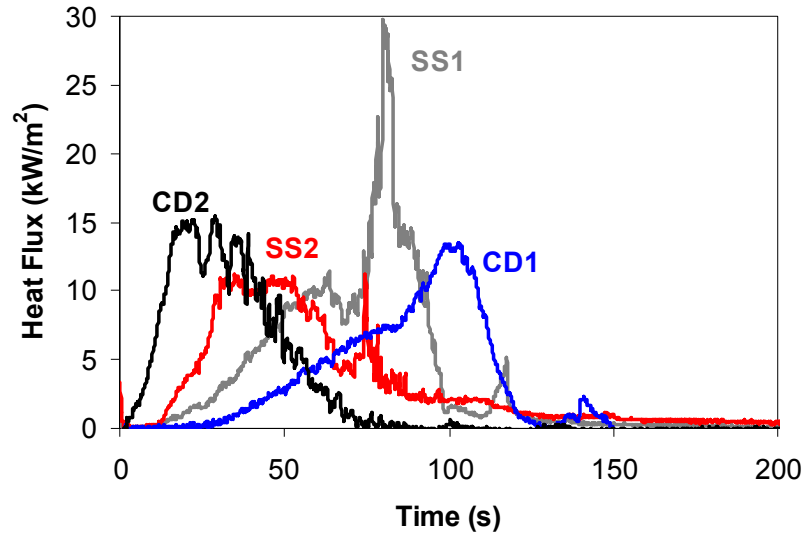


FIGURE 5.12 Heat Fluxes from All Four Sensors for a Lightweight Cotton Test at the 7 mm Air Gap in the Flipped Orientation

Heat flux curves change in appearance for various test conditions. Figure 5.13 shows the heat fluxes achieved for two different lightweight cotton fabrics tested using the 7 mm air gap. One is in the vertical orientation, the other is horizontal. In both cases only data from the two copper disk sensors is shown for clarity. The vertical heat flux curves peak higher, sharper and sooner than the horizontal heat flux curves, which are more similar in shape to the heat flux curves from the flipped orientation. Both vertical peaks are about 25 kW/m^2 while the horizontal peaks are 12 and 6 kW/m^2 for CD1 and CD2 respectively. Vertical heat fluxes are higher than the horizontal and flipped because the flow of hot gases due to buoyancy is in the same direction as the

flame spread. Having the vertical peaks close together in time reflects that the flame spread rates for the vertical orientation are much faster than at the other orientations.

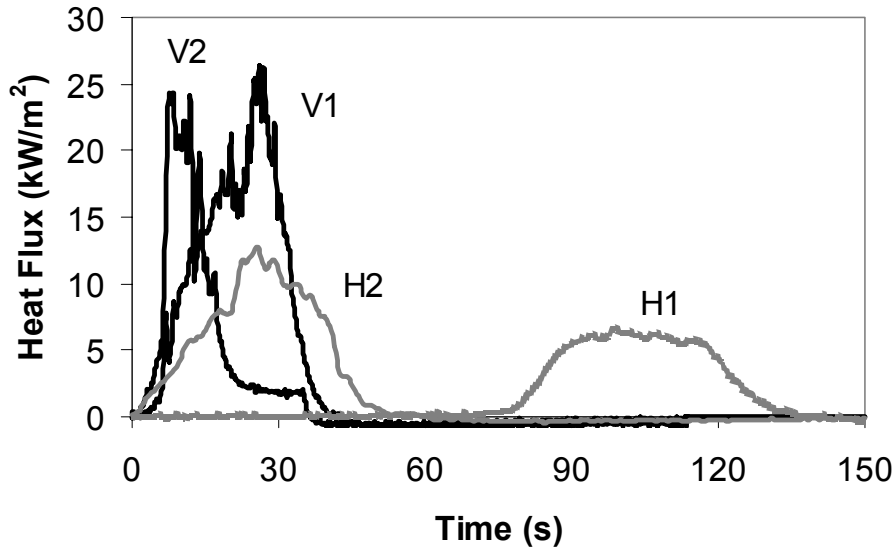


FIGURE 5.13 Heat Fluxes Measured By Two Copper Disk Heat Flux Sensors (1 and 2) for the Lightweight Cotton Fabric with a 7 mm Air Gap in Vertical (V) and Horizontal (H) Orientations

The maximum heat flux measured by each sensor was determined for each 1-g test. Results from the same orientation, air gap, and fabric type were then averaged together to get a representative heat flux value for each sensor. These heat fluxes were found to range anywhere from 6.3 kW/m² to 50.3 kW/m² and are listed in Table 5.6. These heat fluxes can be compared with those from some real life examples. The heat flux 10 cm away from a 100 W incandescent light bulb is 6.4 kW/m² and 100 kW/m² is the heat flux impingent from a propane torch at the flame tip [58]. Note that for the vertical orientation, a heat flux value for SS1 is not included in the Table because the flame rarely spreads in the downward direction where this sensor is located. Table 5.6 shows that there is a large range in maximum heat flux values for different sensors under

the same test conditions. Although some of these results may be due to the nature of the different sensors as outlined in section 4.2.3, they are also affected by the flickering behaviour of fire itself as the flame constantly changes size and shape which changes the heat flux.

TABLE 5.6 Maximum Heat Flux Values (kW/m^2) for Each Test Sensor

Fabric	Orientation	Air Gap	SS1	SS2	CD1	CD2
Lightweight Cotton	Vertical	7 mm	n/a	41.3	24.0	23.7
		13 mm	n/a	23.3	21.0	10.3
	Horizontal	7 mm	28.0	41.0	6.7	13.3
		13 mm	15.0	17.3	11.0	25.0
	Flipped	7 mm	16.7	16.0	10.0	17.7
		13 mm	9.0	16.3	8.7	15.0
Heavyweight Cotton	Vertical	7 mm	n/a	37.5	15.5	20.0
		13 mm	n/a	25.0	19.7	10.0
	Horizontal	7 mm	22.0	27.3	7.0	12.3
		13 mm	14.7	18.0	10.0	23.0
	Flipped	7 mm	8.0	10.0	8.7	21.7
		13 mm	9.0	8.7	6.3	13.7
Lightweight Blend	Vertical	7 mm	n/a	38.3	26.3	26.0
		13 mm	n/a	20.3	10.3	19.0
	Horizontal	7 mm	22.3	28.0	9.0	16.0
		13 mm	13.7	22.7	11.0	18.3
	Flipped	7 mm	33.7	34.0	21.7	28.0
		13 mm	9.7	28.0	24.7	28.0
Heavyweight Blend	Vertical	7 mm	n/a	50.3	28.3	28.7
		13 mm	n/a	30.7	19.3	14
	Horizontal	7 mm	24.0	25.0	7.0	11.7
		13 mm	22.3	22.0	12.3	17.3
	Flipped	7 mm	12.0	26.3	11.7	31.3
		13 mm	16.0	36.7	20.3	30.0

Due to the random nature of fire, the heat flux values read by the same sensor for different tests under the same conditions were found to vary. On average, the values from each sensor for each test condition deviated 24% from the average value presented in Table 5.6. Some never changed for all three trials, such as the first skin simulant (SS1) sensor for the heavyweight blend in the flipped orientation at the 7 mm air gap,

which read a maximum of 12.0 kW/m² for each test performed. Others were not as consistent, such as the first skin simulant (SS1) sensor for the heavyweight cotton in the horizontal orientation at the 7 mm air gap, which read 11, 24 and 31 kW/m² for the three tests.

The maximum values for the individual sensors in Table 5.6 were then averaged together to obtain a single average maximum heat flux value for each test. These results are presented in Table 5.7.

TABLE 5.7 Average Maximum Heat Flux Value for All Fabrics in Various Orientations at 7 mm and 13 mm Air Gaps

ORIENTATION	FABRIC TYPE	Average Maximum Heat Flux (kW/m²) 7 mm Air Gap	Average Maximum Heat Flux (kW/m²) 13 mm Air Gap
VERTICAL	Lightweight Cotton	29.7	18.2
	Heavyweight Cotton	24.3	18.2
	Lightweight Blend	30.2	16.6
	Heavyweight Blend	35.8	21.3
HORIZONTAL	Lightweight Cotton	22.3	17.1
	Heavyweight Cotton	17.2	16.4
	Lightweight Blend	18.8	16.4
	Heavyweight Blend	16.9	18.5
FLIPPED	Lightweight Cotton	15.1	12.3
	Heavyweight Cotton	12.1	9.4
	Lightweight Blend	29.3	22.6
	Heavyweight Blend	20.3	25.8

In Backer's summary of the GIRCFF research project [40] it is explained that there are many factors that affect the heat flux from a burning fabric to the skin and hence skin burn injury outlined below. It is not the individual factors alone that can be used to assess heat fluxes, but rather the combined effect of them all. The factors affecting the heat fluxes and burn injury to skin are:

- thermal radiation from hot gases and the heated fabric which is directly proportional to the fourth power of temperature and inversely proportional to the square of the size of the air gap
- convection and conduction through the air gap which is directly proportional to the temperature of the hot gases in the air gap and depends on whether or not convective cells develop within the air gap
- condensation of steam and pyrolysis products from the fabric which is dependant on air gap size
- exposure time which is inversely proportional to flame spread rate (which increases as the air gap is increased)

In an effort to determine how much heat transfer comes from thermal radiation, conduction and convection, and how these change at the different orientations, some preliminary heat flux calculations were done assuming different surface temperatures of the fabric. These calculations were not intended to be a representative model of the experiments performed. They are merely simple calculations to illustrate the radiation, conduction and convection heat transfer contributions for an enclosure with a hot surface parallel to a cold surface. In actual fact, the enclosure is not completely sealed as the fabric is porous, the fabric breaks apart during burning, and the short ends of the fabric specimen are not taped to the specimen holder. The radiation heat transfer calculations used were very simple. The air flow in the gap parallel to the hot and cold surfaces was also not accounted for in these calculations. Throughout the discussion of heat flux results that follows, when the movement of hot gases is mentioned it refers to movement perpendicular to the fabric and sensor board only and does not account for movement in

the parallel direction. To begin the calculations, ignition temperatures of cotton in the literature were found to range between 250°C [59] and 407°C [45]. Temperature measurements from the IR camera during the flight indicate the cotton temperatures generally reached a maximum of about 285°C while the blends were a little warmer at about 305°C. Therefore, the heat transfer estimates were done assuming fabric temperatures of 250, 300, 350 and 400°C. It should also be noted that the temperature of the hot gases in the air space may be higher than the fabric temperatures. The estimated heat flux as due to radiation, conduction, and convection are listed in Table 5.8. The equations used and calculations done to obtain these heat fluxes are shown Appendix B.

Table 5.8 shows that generally the total heat flux from radiation, conduction and convection is much less than the heat fluxes the sensors are measuring during the experiments listed in Table 5.7. This indicates that other modes of energy transfer, such as the energy being released during the chemical reaction and deposition of products of combustion play a large role in the total heat flux to the sensors. Note that in Table 5.7, at the 13 mm air gap the heat fluxes predicted are highest for the flipped orientation, followed by the vertical and horizontal orientations. Those predicted at the 7 mm air gap are slightly higher than the 13 mm values, but do not change with a change in orientation because the air gap is too small for convective heat transfer to occur, as shown in Appendix B. The heat transfer is simply by conduction and radiation, both of which do not change with orientation. Overall it seems that a change in orientation and air gap does not have a large effect on the radiation, convection and conduction heat transfer contributions. Therefore, it is likely that changes to orientation have a larger effect on flame spread rate, deposition of combustion products and other factors not accounted for in these calculations that affect the heat transfer. These other factors

could include the enclosure not being completely sealed, and the various flow patterns of the hot gases through the air gap because of this. All these factors contribute to make the experimental heat flux values higher than those predicted for the simple case represented in Table 5.8.

TABLE 5.8 Estimated Radiation, Conduction and Convection Heat Transfer for Both Air Gaps in All Orientations based on Four Different Fabric Temperatures

AIR GAP & ORIENTATION	CALCULATED TOTAL HEAT FLUX (kW/m ²)			
	250°C	300°C	350°C	400°C
7 mm F, V, and H	4.5	6.5	9.0	12.2
13 mm FLIPPED	4.3	6.2	8.5	11.3
13 mm VERTICAL	3.9	5.6	7.8	10.5
13 mm HORIZONTAL	3.6	5.3	7.4	10.1

The maximum experimental heat flux values from Table 5.7 are plotted separately at each of the air gaps showing all the orientations for further investigation. Figure 5.14a shows the average maximum heat fluxes for the 7 mm air gap tests, while Figure 5.14b has the 13 mm air gap results. By comparing the vertical heat fluxes in Figure 5.14a and 5.14b it is seen that the maximum heat fluxes were mostly dependent on the air gap, as the four fabrics at the 7 mm air gap all had higher heat fluxes than at the 13 mm air gap. Because the burning behaviour did not appear to change substantially throughout the vertical tests it makes sense that the heat fluxes at 7 mm would be higher than those at 13 mm simply because the hot gases are closer to the sensors. Contrary to this, in the flipped orientation, heat fluxes are more dependent on fabric composition, as the blends at both air gaps had higher heat flux values than the

cottons, as shown in the figures. This could be attributed to the difference in burn behaviour of the two different fabric types. Images of fabrics burning in the flipped orientation are shown in Figures 5.5 through 5.8. When the cottons burn, a small blue surface flame stays on the under side of the fabric away from the heat flux sensors, but when the blends burn, a flame protrudes up into the air gap touching the sensors which in turn increases the measured heat flux. The smallest range of values was found in the horizontal orientation, where the heat fluxes were in the mid range between about 16.4 and 22.3 kW/m², indicating that air gap and fabric type have the least effect on this orientation, likely because most of the hot gases are moving away from the sensors.

From Figure 5.14a it is seen that both cotton fabrics have a highest heat flux in the vertical orientation, followed by the horizontal value and then the flipped. Figure 5.14b shows that the cottons have the same order of highest to lowest heat flux as Figure 5.14a, indicating that the air gap does not change this order. The main difference in the heat flux comes from the burning behaviour. For cottons in the flipped orientation, the small flame stays on the bottom side of the fabric away from the sensors and the rising hot gases are blocked. This could be why the cottons have the lowest heat flux in the flipped orientation. In the horizontal orientation, although the hot gases are rising away from the sensors, the base of the flame is directly exposed to the sensors when the fabric breaks apart creating a higher heat flux than the flipped case where flame is not directly exposed to the sensors. In the vertical case, the large flame area that can burn on either side of the fabric causes a larger heat flux to the sensors.

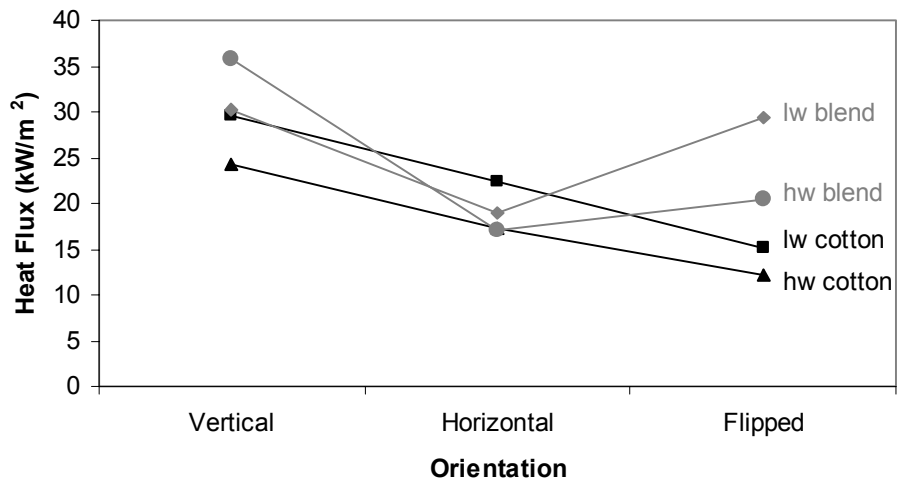


FIGURE 5.14a: Average Maximum Heat Flux Values for 1-g Tests at Various Orientations for the 7 mm Air Gap

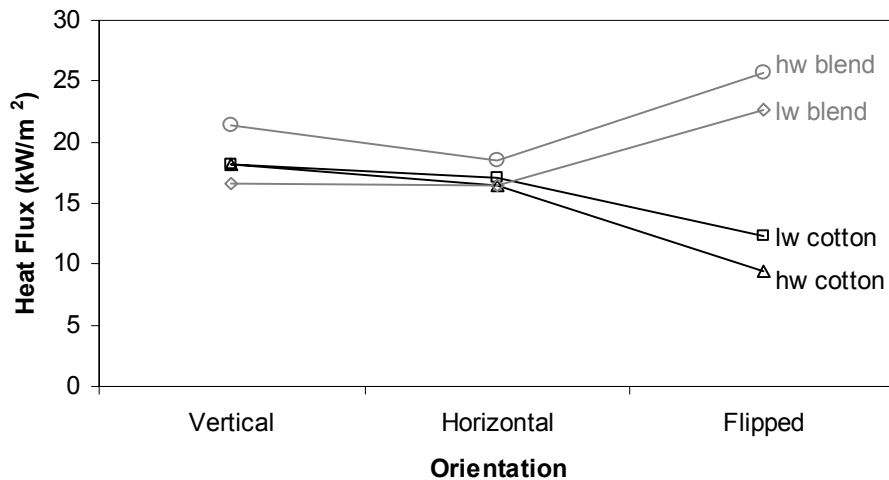


FIGURE 5.14b: Average Maximum Heat Flux Values for 1-g Tests at Various Orientations for the 13 mm Air Gap

From Figure 5.14a it is seen that the blends have highest heat fluxes in the vertical orientation like the cottons, but the next highest heat fluxes are at the flipped orientation and the lowest heat fluxes are in the horizontal orientation. The heat fluxes in the flipped orientation are now higher than the heat fluxes in the horizontal orientation because there is a small flame shooting upward in the air gap, as seen in Figures 5.7a

and 5.8a. For the blends at the 13 mm air gap, the flipped heat flux value becomes higher than both the horizontal and the vertical orientations, shown in Figure 5.5b. Again the reason for this lies in the burning behaviour, as now the only flame seen is directed upward in the air gap towards the sensors as shown in Figures 5.7b and 5.8b. Cottons in the flipped orientation see a large drop in heat flux while the blends see a large increase because of this difference in the flame size and location.

It should also be noted that for nearly all test cases, the heat flux value at the 7 mm air gap was greater than the corresponding value at the 13 mm air gap, likely because the flame and combustion reaction are all closer to the sensors. Radiation from the hot gases, and the exposure time, factors affecting the heat fluxes to the sensor listed earlier in this section, would all predict higher heat fluxes at the 7 mm air gap than at the 13 mm air gap. The radiation would be greater at the smaller air gap because the view factor is higher and the exposure time longer because the flame spread rates are slower. The combustion products would also be able to cross the smaller air gap in a shorter amount of time. The only two cases where the heat flux value was greater at the larger air gap were the heavyweight blend fabric at both the horizontal and flipped orientations. Photos of these tests are seen in Figures 5.4b and 5.8b. It appears that the size of the flame is larger for an air gap of 13 mm than an air gap of 7 mm for these cases, and that the size of the flame is the most important factor affecting the heat fluxes.

5.5.2 Microgravity Heat Fluxes

Microgravity tests were run for three of the fabrics – both cottons, and the lightweight blend. Both the 7 mm and 13 mm air gaps were used in tests in standard air (21% oxygen, 79% nitrogen) and oxygen enriched air (25% oxygen, 75% nitrogen).

Heat flux data was obtained from prior to ignition to after extinction. This section will give information on the heat fluxes obtained from the microgravity flight data.

A plot of the heat flux data for the lightweight cotton at the 7 mm air gap in 21% oxygen is shown in Figure 5.15a. Figure 5.15a includes heat flux curves for three of the four sensors. The bottom skin simulant (SS1) did not register any significant heat flux because there was little downward flame spread, so it is not included in the plot. Figure 5.15a shows both the pull-up and pull-out 1.8-g periods and the middle μ -g period. Lines on the graph indicate the time periods when the igniter was on and when the gravity level was low. Heat fluxes near the beginning of the test reach values of about 35 kW/m^2 for both the CD2 and SS2 sensors. These values are in the upper range of those observed in the 1-g tests. From Figure 5.15a it appears that the flame has spread across CD2 and is near SS2 propagating towards CD1 when the transition to microgravity occurs. At this time the heat flux from SS2 drops off substantially. The CD1 sensor reaches a maximum value of only 15 kW/m^2 , because the flame decreases in size during transition to μ -g, so likely the flame is no longer seen over this top sensor. After the transition to microgravity, the heat flux values drop off. Recall from Section 4.4 that to further investigate the heat flux in μ -g, only the microgravity portion of each test was looked at. Figure 5.15b is the same curve as Figure 5.15a, but for the μ -g time span only.

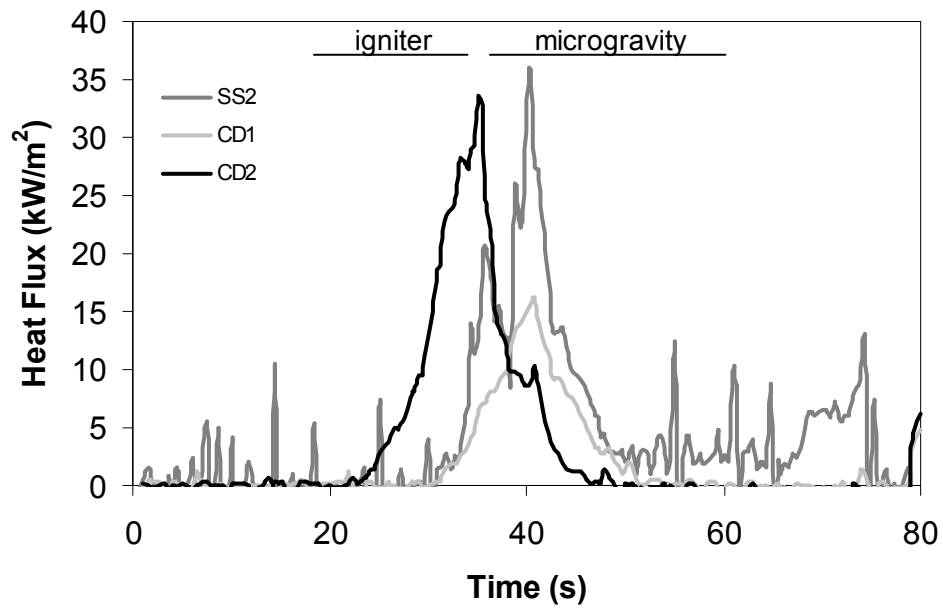


FIGURE 5.15a: Heat Flux Curve for the Lightweight Cotton Fabric at the 7 mm Air Gap from the Microgravity Flight Data

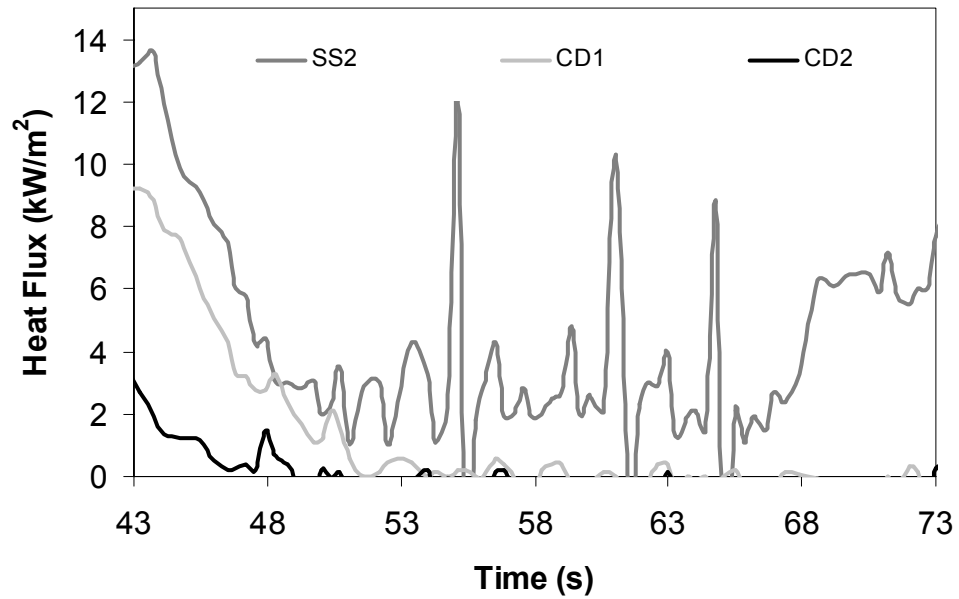


FIGURE 5.15b: Microgravity Portion of the Heat Flux Curve for the Lightweight Cotton Fabric at the 7 mm Air Gap from the Microgravity Flight Data

Figure 5.15b shows that after the heat fluxes decrease from their initial value they seem to level off for much of the microgravity period. It can also be seen that the copper disk sensors both measure negligible heat fluxes, while the skin simulant sensor measures a nominal value greater than zero. Having only one sensor register a noticeable heat flux while the others are essentially zero, as is the case in this test, is quite typical of the microgravity results. This is because the flame size in microgravity is much smaller, so the heat flux is typically only read by the closest sensor, and the 20 s time span is not long enough to observe the spread of flame from one sensor to another. The fastest flame spread rate observed for a single microgravity test was 1.6 mm/s. Even at this rate it would take 28 s to travel the 45 mm between sensors. The average heat flux value obtained from the test data in Figure 5.15b was 3.0 kW/m². This was obtained by averaging the SS2 heat flux values for 53 to 63 seconds, a 10 s level period of the microgravity test, as described in section 4.4.1.

Table 5.9 lists the heat flux values for all forty flight tests. The numbers in bold in the Table are the highest heat flux obtained for each flight test condition. By looking at the Table it is seen that the microgravity heat fluxes are lower than those from the ground tests. Reasons for this are the lack of buoyancy forces and the smaller flame sizes on the burning samples. The lack of buoyancy forces means that there is essentially no convective heat transfer occurring in the air space. The smaller flame size will result in lower radiation heat transfer. Radiation heat transfer values were estimated for a smaller flame with a surface temperature of 300°C to disks of 40 and 22 mm diameter disks (copper calorimeter and skin simulant sizes). The values ranged between 1.9 and 4.9 kW/m², with the calculations shown in Appendix B. These values are closer to those measured in microgravity. It also appears that the air gap does not determine

which heat flux value is the highest likely because with no buoyancy forces the air movement within the air gaps does not change much or affect the heat transfer much. Also, the lightweight blend has noticeably higher heat fluxes in the higher oxygen concentration, indicating that combustion increases in the enriched oxygen environment.

TABLE 5.9 Heat Flux Values from the Microgravity Flight Tests*

FABRIC TYPE	21% Oxygen HEAT FLUX (kW/m ²)		25% Oxygen HEAT FLUX (kW/m ²)	
	7 mm	13 mm	7 mm	13 mm
Lightweight Cotton	0.6	1.0	2.5	0.9
	1.2	0.8	1.1	2.0
	3.0	0.6	2.0	1.3
	0.1	0.5	2.0	1.2
Heavyweight Cotton	1.6	1.5	2.0	2.0
	2.0	3.0	1.1	2.0
	3.0	0.5	1.0	1.5
Lightweight Blend	0.5	0.3	2.0	2.0
	0.3	0.7	0.6	1.2
	0.2	0.5	2.0	2.0

*Numbers in bold indicate the highest heat flux value for each test condition

Generally speaking, these microgravity heat flux results only touch the surface of what needs to be explored. There are limited tests and limited data in this study. While the heat fluxes in microgravity are significantly lower than those in 1-g, there is no real pattern to the μ -g results. This is likely because the heat flux value obtained depended on how well the fabric burned and where the flame was in relation to a sensor. A good burn of the fabric specimen was dependent on a good ignition at the desirable time before the μ -g portion of the parabola, which was not always attained. If the flame happened to be positioned directly over a sensor during μ -g, chances are the heat flux for that test would be higher than if the flame were positioned between two sensors. Unfortunately, during the flight tests there was little to no control over the location of the flame during the transition to microgravity.

5.6 Predicted Skin Burn Injuries

In this section predicted skin burn injury times are presented for the experiments. Ground test results will be presented first, followed by microgravity results. Skin burn injury times were predicted from the heat flux data as described in sections 4.1.2 and 4.2.2, with the microgravity calculation process explained in section 4.4.1. Skin burn injury is dependant on the heat flux to the skin. Therefore, the relative rankings of the results in this section should be the same as those just presented in the heat flux results section.

When examining the burn prediction, it should be noted that Henriques' burn integral (section 1.2.4, equation 1.4) is non-linear, meaning that a small change in heat flux may have a large effect of burn predictions, especially at the lower heat fluxes. To investigate this, skin burn injury times were predicted using the burn integral with various constant heat flux inputs. These results are shown in Table 5.10. This Table indicates that for a 2 kW/m^2 change in heat flux, the predicted burn times can change by a few seconds. The worst case is for the lower heat fluxes. By looking at the difference in predicted burn times for 10 and 12 kW/m^2 it is seen that for a 20% difference in heat fluxes there is a 30% difference in second degree burn times and a 17% difference in third degree burn times. The non-linear behaviour of Henriques' burn integral is also seen in the Stoll Criterion (section 1.2.3, Figure 1.3). By observing the Stoll criterion in Figure 1.3, it can be seen that at the lower heat fluxes, a small difference in heat flux will result in a larger change in predicted burn time, as was shown in Table 5.10 for Henriques' burn integral.

TABLE 5.10 Second and Third Degree Burn Times Predicted by Henriques' Burn Integral for a Constant Heat Flux

HEAT FLUX (kW/m ²)	TIME TO 2° BURN (s)	TIME TO 3° BURN (s)
10	9.90	35
12	7.60	30
14	6.10	27
16	4.98	24
18	4.20	22
20	3.60	21

5.6.1 Second Degree Skin Burn Times in 1-g

Some typical values for second degree burn times at the various orientations are shown in Figure 5.16. The data used in this Figure are average values for the lightweight cotton fabric at the 7 mm air gap. Similar plots for the other test conditions are located in Appendix C. Recall that the igniter is located in the centre of CD2. For the horizontal and flipped orientations, the burn always occurred here first, followed by the skin simulants and then the far copper disk. The further the sensor is from the ignition location, the longer the time for a second degree burn to occur, as the flame must first spread to reach the location. By looking at the heat flux plot in Figure 5.12, it can be seen that the order of predicted burns corresponds with the order of heat flux peaks for the different sensors. In Figure 5.12, the CD2 peak is first, followed by the SS2 and SS1 peaks, with the CD1 peak being the last. This is the same order of predicted burn times from fastest to slowest in Figure 5.16.

For the vertical orientation, the spread is predominantly in the upward direction, as it is aided by buoyancy forces. This results in the bottom skin simulant (SS1) either not predicting a burn time (no downward flame spread), or predicting one much slower (downward flame spread does occur) than the sensors located above the ignition point. Recall there are no heat fluxes for SS1 in the vertical orientation in Table 5.5 because downward spread was rare. While all other data points in Figure 5.16 are averages from multiple tests, the SS1 value is from a single test, as downward spread was only observed once for this test condition. The buoyancy forces in the vertical orientation can also affect the heat transfer such that the SS2 sensor data actually predicts a faster burn time than the CD2 ignition sensor, as is the case in Figure 5.16. Because the ignition location is in the centre of the copper disk and the flame is moving upward, the top half of the copper disk sees the flame while the bottom half does not. The flame also then quickly progresses across the skin simulant (SS2) just above. Since the entire surface of the skin simulant sees the flame while initially only the top half of the copper disk does, the predicted burn time for the skin simulant SS2 may be faster than that predicted for the copper disk CD2. This can be seen in Figure 5.2a, which is a heavyweight cotton vertical test at the 7 mm air gap. The flame has already progressed upward over the SS2 sensor and since there is no downward burning, the CD2 disk was only half exposed to the flame before it progressed upward. The top edge of the unburned portion of the fabric specimen lies about 73 mm from the bottom edge of the fabric, which is equal to the centre of the copper disk (CD2) sensor.

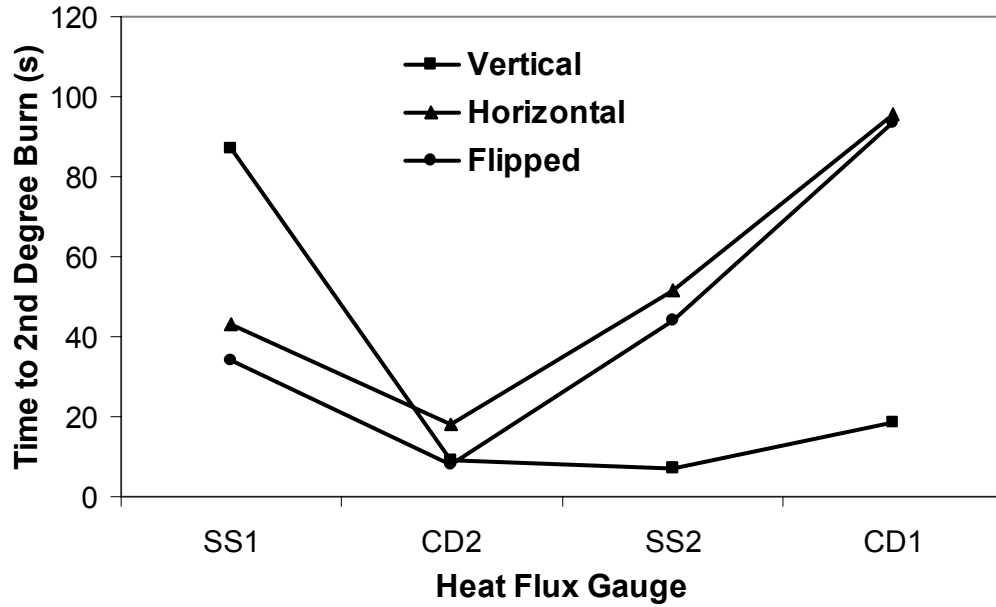


FIGURE 5.16: Skin Burn Injury Times for the Lightweight Cotton Fabric at the 7 mm Air Gap for Various 1-g Orientations

From Figure 5.16 the different burn times at the various orientations can be compared. In general, the vertical orientation showed the fastest burn times, with the flipped orientation being the second fastest and the horizontal being third. Predicted second degree burn times for the vertical orientation ranged from 1.4 to 18.8 s. This excludes the SS1 burn times, as at the 13 mm air gap (see Appendix C), no vertical test predicted a burn time for SS1, as the flame did not spread in this direction. At the 7 mm air gap, only one of each of the three tests for each fabric in the vertical orientation predicted a burn time. In general the downward spread of flame did not occur because the hot gases were rising up; however, with higher heat fluxes at the smaller air gap, as shown in Table 5.6, there was a better chance for downward spread to occur. The SS1 predicted burn times ranged anywhere from 54 s to 98 s, which is much longer than any of the times for the sensors above the ignition point. The main factor in these predicted burn times was how long into the test it was before the downward spread began.

Predicted second degree burn times for the flipped orientation ranged from 1.9 to 93.6 s and from 8.8 to 128.9 s in the horizontal orientation. Again this is compared to 1.4 to 18.8 s for the vertical orientation. Again by looking at the heat flux curves of the different orientations, one can get an idea of why the predicted burn times are different. By looking at Figure 5.13, it can be seen that the heat flux peaks for the vertical test are much higher and occur sooner than the horizontal heat flux peaks, which are lower and more spread out in time. This indicates that the burn times in the vertical orientation would be much shorter than in the horizontal burn times. By looking at the two copper disk peaks from the Figure 5.12 and comparing them to Figure 5.13, it can be seen that the flipped orientation heat fluxes are much more similar in behaviour to the horizontal orientation, than the vertical, which is what was found with the predicted burn times as well.

Figures 5.17a, b and c show the predicted second degree burn times for the different fabrics at each orientation for the 7 mm air gap. Figure 5.17a shows the vertical orientation results. The bottom skin simulant, SS1, was not included in the chart as it often predicts no burns, or lengthier burn times as previously outlined. Vertical burn times from the Figure range from 1.4 s to 18.8 s, with the blends having consistently faster predicted burn times than the cottons, as for most cases their heat fluxes were higher (Figures 5.14a and 5.14b). Also note that the predicted burn time at SS2 is shorter than that at CD2 (ignition) for all fabrics except the heavyweight blend, the heaviest of the four fabrics. This goes back to the fast upward spread of the flame causing a burn at the sensor above the ignition point. Because the spread of flame is slower for the heavier fabric, the burn could occur at CD2 before the SS2 sensor.

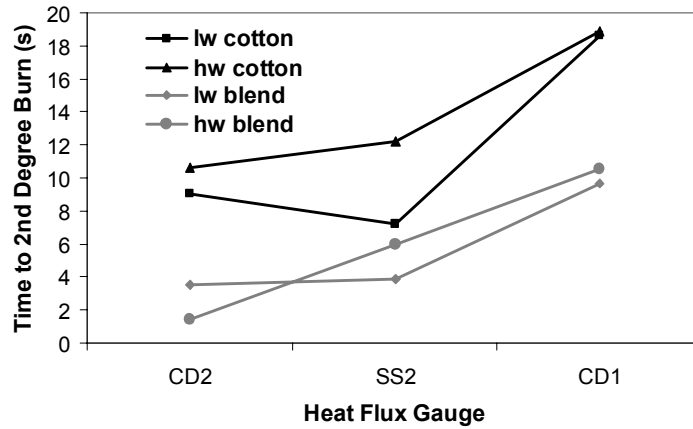


FIGURE 5.17a: Average Predicted Second Degree Burn Times for All Fabric Types at the 7 mm Air Gap in the Vertical Orientation in 1-g

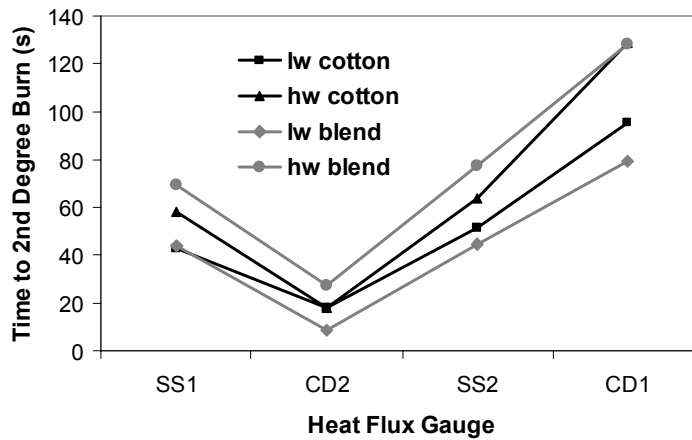


FIGURE 5.17b: Average Predicted Second Degree Burn Times for All Fabric Types at the 7 mm Air Gap in the Horizontal Orientation in 1-g

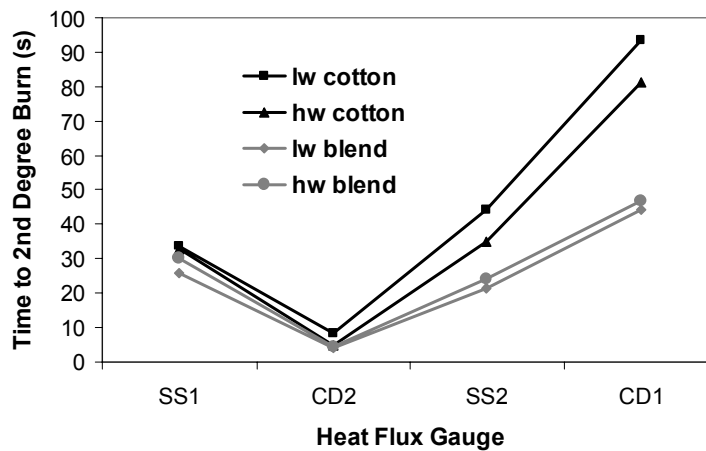


FIGURE 5.17c: Average Predicted Second Degree Burn Times for All Fabric Types at the 7 mm Air Gap in the Flipped Orientation in 1-g

Figure 5.17b shows predicted burn times for the horizontal orientation at a 7 mm air gap. The burn times here range from 8.8 s to 128.9 s, significantly longer than the vertical orientation. These predicted burn times are largely determined by fabric weight as the order of shortest to longest burn times corresponds with lightest to heaviest fabric. Contrary to this, for the flipped orientation at the 7 mm air gap the burn times are more dependant on fabric composition as, like the vertical orientation, the blends have shorter predicted burn times than the cottons. This is shown in Figure 5.17c. Again, faster predicted burn times for the blend fabrics are due to the higher heat fluxes exhibited by the blends in the flipped orientation (shown in Figures 5.14a and 5.14b). The burn times for the flipped orientation are seen to range between 4.4s and 93.6 s, which are in between the burn times in the vertical and horizontal orientations.

Similar plots but at the 13 mm air gap are included in Appendix C. At this air gap for both the vertical and horizontal orientations, the lightweight fabrics have shorter burn times than the heavier ones, and the blends again burn faster than the cottons for the flipped orientation. These are similar trends to those found at the 7 mm air gap.

5.6.2 Third Degree Skin Burn Times in 1-g

Third degree burn times were also obtained for 1-g tests as outlined in sections 4.1.3 and 4.2.2. Overall, the results follow similar patterns to the second degree burn times, but the times themselves are obviously longer than the second degree ones. The third degree burn times are plotted for the lightweight cotton at a 7 mm air gap for the various orientations in Figure 5.18. Plots of the remaining third degree burn time data is found in Appendix C. The range of predicted third degree burn times for the vertical test (excluding SS1) was 14.8 to 49.7 s. The flipped range was 17.7 to 122.2 s while the

horizontal range was 27.0 to 177.7 s. As for the second degree burn times, the burn times in the vertical orientation are much faster than the burn times in the flipped and horizontal orientations, which are much closer to each other. Because the third degree burns are predicted from the same heat flux data as the second degree burn it is expected that the results would have similar relative magnitudes. This is seen by the resemblance in shape of Figure 5.16 and 5.18.

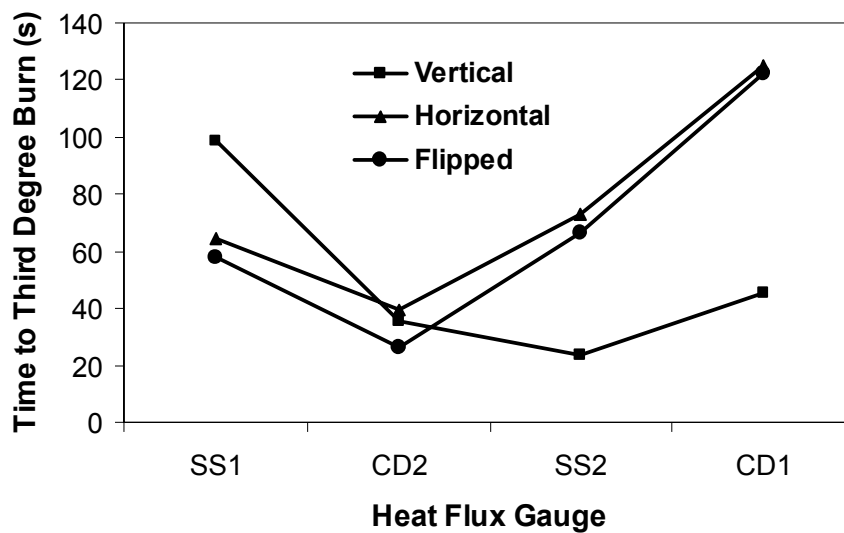


FIGURE 5.18 Predicted Third Degree Skin Burn Injury Times for the Lightweight Cotton at the 7 mm Air Gap for Various Orientations in 1-g

It is interesting to note that third degree burns were not predicted by all sensors at all tests. No third degree burn was predicted by the SS1 sensor for any fabric at the 13 mm air gap in the vertical configuration. This is not surprising because no second degree burn was predicted for these cases either, as the flame did not spread downward in the vertical orientation at the larger air gap. For the CD2 sensor, that over which ignition occurs, again no fabrics in the vertical orientation at the 13 mm air gap predicted a third degree burn time even though the heavyweight cotton and both blends

predicted a second degree burn for this condition. The reason third degree burns were not predicted is that the spread of flame upward on the specimen away from CD2 was too fast to allow a third degree burn to occur there. The next sensor above ignition, SS2, had predicted second degree burns for all vertical cases, but failed to predict a third degree burn at the 13 mm air gap for the two lightweight fabrics. The lightweight fabrics have the fastest flame spread rates in this vertical orientation at the 13 mm air gap. The spread rates are too fast to allow enough thermal dosage to the skin from the passing flame to cause a third degree burn. Finally, the top sensor, CD1, again does not predict a third degree burn time at the vertical 13 mm air gap condition for the lightweight blend, as this condition and fabric had the fastest flame spread rate of all the tests. Another explanation for why the third degree burns were less likely to be predicted at the larger air gap for the vertical tests is that the heat fluxes for the 13 mm air gap are significantly lower than those at the 7 mm air gap as shown in Table 5.6.

5.6.3 Second Degree Skin Burn Times in Microgravity

Burn times predicted from the microgravity data had a very large range. Some were found to be around 53 s while another took in excess of a few minutes. The burn prediction technique used was slightly different than that used for the 1-g tests, as outlined in Section 4.4.1. It involved obtaining a single average heat flux value from one sensor for the test, using this as a constant incident heat flux, and predicting the second degree burn time using the Stoll criterion. Another difference from the 1-g results is that for μ -g a single burn time is predicted from one test.

Table 5.11 shows the different burn times predicted for the different flight conditions. These were obtained from the highest heat flux value for each test condition,

indicated in bold in Table 5.9. It can be seen that the fastest burn times were obtained for the lightweight cotton at the 7 mm air gap and for the heavyweight cotton at both air gaps, all of these being 21% oxygen tests. The lightweight blend in the 21% oxygen experiences very long predicted burn times, however, in the 25% oxygen case results were similar to the cottons in the 25% oxygen. These burn times are a direct reflection of the microgravity heat fluxes used. A heat flux of 3.0 kW/m² predicted 53 s to second degree burn injury. A heat flux of 2.5 kW/m² corresponded to a predicted second degree burn time of 69 s, and 2.0 kW/m² predicted 94 s for a second degree burn to occur. The remaining times in Table 5.9 come from incident heat fluxes of 1.0 kW/m² or less, resulting in the longest predicted burn times. These are for the lightweight cotton at the 13 mm air gap and the lightweight blend at both the 7 mm and 13 mm air gaps, all for the lower oxygen concentration. With the heat flux being quite low for these tests, the method of predicting burn times ceases to be useful, as the error in the predicted times gets large, as was discussed at the beginning of section 5.6.

TABLE 5.11 Microgravity Predicted Skin Burn Injury Times

FABRIC TYPE	21% Oxygen		25% Oxygen	
	2° BURN TIME (s)		2° BURN TIME (s)	
	7 mm	13 mm	7 mm	13mm
Lightweight Cotton	53	>120	69	94
Heavyweight Cotton	53	53	94	94
Lightweight Blend	>120	>120	94	94

5.7 Implications on Test Development

One goal of this research was to provide insight on developing a test method to be used in 1-g that would be representative of μ -g behaviour and results. While the vertical orientation predicted more severe skin burns and measured faster flame spread rates than

the microgravity tests, results from the other two orientations (horizontal and flipped) more closely resembled microgravity. The three fabrics tested in microgravity were the lightweight cotton, the heavyweight cotton, and the lightweight blend.

In general, flame spread rates in μ -g were close to some of the rates observed in 1-g, especially for the cottons. At the 7 mm air gap, flame spread rates for all three fabrics in μ -g were closest to flame spread rates in 1-g in the horizontal orientation. This was again the case for the lightweight blend at the 13 mm air gap. However, for the cottons at the 13 mm air gap, the μ -g flame spread rates were closest to the 1-g flame spread rates in the flipped orientation.

Heat fluxes obtained during μ -g were generally significantly lower than those obtained in 1-g because of the diminished flame size and limited movement of hot gases, both due to the lack of buoyancy forces. For the cottons at both air gaps, the 1-g heat flux was lowest in the flipped orientation, and thus closest to the μ -g value. Contrary to this, the horizontal orientation provided the lowest 1-g heat fluxes for the lightweight blend at both air gaps, making this orientation most comparable to the μ -g results.

As no single 1-g orientation was found to be the closest to the microgravity results in all cases care must be taken when choosing an orientation to represent microgravity. Depending on the fabric type and whether flame spread rates or heat fluxes are being investigated, either the flipped or horizontal orientation should be used. For example, if looking for heat fluxes from cotton fabrics closest to the μ -g values, the flipped orientation in 1-g should be used. A caution is that this work is limited to the experimental variables tested, such as fabric type and air gap, and thus the findings may not extend to all cases in general.

5.8 Summary

In this chapter flame spread rates and heat fluxes determined for 1-g tests at horizontal, flipped and vertical orientations in 1-g were presented and discussed, along with flame spread rates and heat fluxes determined for μ -g. A look at 1-g flame spread rates for the heavyweight cotton fabric at various angle of inclination was also included. Once the flame spread rates and heat fluxes had been presented, the predicted skin burn injury times were discussed, as they are affected and determined by the previous two items of interest. Comparisons were then made between the skin burn injury predicted in 1-g and μ -g environments.

CHAPTER 6 CONCLUSIONS AND RECOMMENDATIONS

In this thesis flame spread rates, heat fluxes and predicted skin burn injury times were found for 100% cotton and 50% cotton/50% polyester blend textile fabrics that had been ignited. Variables in the tests included fabric type, apparatus orientation, air gap, gravity level, and oxygen concentration. Tests conducted under various different conditions were compared. Conclusions and recommendations from this work are presented below.

6.1 CONCLUSIONS

- Flame spread rates in 1-g are affected by the fabric type, air gap, and orientation of the apparatus. Tests in the vertical orientation had flame spread rates twice as fast as horizontal and flipped orientations, as there is naturally concurrent flow induced for the vertical situation. Flame spread rates are faster with a 13 mm air gap than with a 7 mm air gap, with this effect the most evident for the horizontal orientation. In both the vertical and horizontal orientations, flame spread rates for the lightweight fabrics were faster than the heavyweight fabrics. Out of the two lightweight and two heavyweight fabrics, the cotton/polyester blend was faster than the cotton. For the flipped orientation, both blends had faster flame spread times than the cottons. In general, fabrics of lower mass have faster flame spread rates and polyester/cotton blend fabrics have faster spread rates than cottons of comparable weight.

- Flame spread rates at various angles of inclination are slowest at 0° (horizontal) and fastest at 90° (vertical). For the heavyweight cotton blend with a 7 mm air gap, the flame spread rate is fairly constant up to an angle of about 22.5° after which point the flame spread rate begins to noticeably increase, indicating a change from counter-current to concurrent flow.

- Heat fluxes in 1-g are affected by all experimental variables. Heat fluxes in the vertical orientation are the highest, followed by the horizontal and flipped orientations. In the vertical orientation, the heat fluxes were most affected by air gap, as the heat fluxes at the 7 mm air gap were on average 62% higher than those found at the 13 mm air gap. In the flipped orientation, the heat fluxes were most affected by fabric type, as the blends had an average heat flux nearly twice as high as the cottons at both air gaps. The horizontal orientation saw the smallest range in heat flux values indicating tests in terms of heat flux, tests in this orientation are not as sensitive to changes in air gap and fabric type as tests in the other two orientations.

- Predicted second degree skin burn injury times were found to range between 1.4 and 165.8 seconds for 1-g tests. The heat flux gauge located directly across from the igniter wire predicted similar burn times for the various orientations. However, when comparisons were made using heat flux gauges further away from ignition, the predicted times to second degree skin burn injury were shortest for tests performed in the vertical orientation because of the faster flame spread and higher heat fluxes. Similar results were found for predicted third degree burn times in 1-g, with the times

just being a bit longer than those predicted for 2nd degree burns, ranging from 14.8 to 177.7 seconds.

- Flame spread rates in μ -g for the cotton fabrics were similar to those found for the horizontal and flipped 1-g cotton tests. Flame spread rates for the lightweight blend in μ -g were much slower than in 1-g. Heat fluxes measured in μ -g for all fabric types were significantly lower than those in 1-g. The largest heat flux value determined from a μ -g test was 3.0 kW/m², while 1-g maximum heat flux values ranged from 9.4 to 35.8 kW/m². The fastest predicted second degree burn time in μ -g was 53 seconds as opposed to 1.4 seconds in 1-g. Changing the weight of the cotton in μ -g had little effect on the results.

- Increasing the oxygen concentration for half of the μ -g tests caused more combustion to occur, as nearly the entire samples were being consumed, rather than the flame extinguishing with fabric still remaining, as was the case in 21% oxygen. Overall the average heat flux value obtained from the tests was slightly higher in 25% oxygen and hence the predicted second degree skin burn injury times were more severe in 25% oxygen than in 21% oxygen.

- Tests in the vertical orientation in 1-g had the fastest flame spread rates, the highest heat fluxes, and the shortest predicted times to skin burn injury.

6.2 RECOMMENDATIONS

The following recommendations for future work are made as a result of this research.

- Investigate the heat release rate from burning fabrics at the various orientations. This may give some insight as to why the measured heat fluxes are different at the different orientations.

- Develop a better technique to measure flame spread rates in microgravity. The flame spread rates presented in this research are rough estimates that only look at a small portion of the flame on the fabric and rely on visual observations. The new technique could involve using the temperature data for the surface of the fabric obtained from the IR camera during the flights.

- Use the temperature data on the surface of the fabrics from the IR camera during the microgravity flights as an input into a model that could predict heat fluxes and skin burn injury times. This would likely give a more accurate second degree burn prediction for each microgravity test than the Stoll criterion using only a single heat flux value from each test, and also allow third degree burn times to be predicted if the model were based on Henriques' burn integral.

- Create a new sensor board for tests using only skin simulant heat flux gauges. This would eliminate the effects of the different sensor types and sizes. The smaller surface area of the skin simulant is better suited for these tests because it takes less time for a moving flame to traverse across a shorter distance.

- Study the flow of hot gases in air gaps with one surface being a burning fabric specimen, as was the case in these experiments. Investigate how this will affect the flame spread rates along the fabric surface in the different orientations.

- Ensure that when ground tests are used to investigate flammability for use in zero-g applications they are indeed worst case. This may involve running more tests in the microgravity environment that could be more severe, such as 25-30% oxygen with induced air flow, and comparing these results to 1-g.

REFERENCES

1. NASA Glenn Research Center Microgravity Combustion Science “Candle Flames in Microgravity”, http://microgravity.grc.nasa.gov/combustion/cfm/cfm_index.htm, accessed June 2004.
2. American Society for Testing and Materials, ASTM D1230-94: Standard Test Method for Flammability of Apparel Textiles, West Conshohocken, PA, 2001
3. Canadian General Standards Board, CAN/CGSB-4.2 No.27.5: Flame Resistance - 45° Angle Test – One Second Flame Impingement, Ottawa, ON, 2000
4. Canadian General Standards Board, CAN/CGSB-4.2 No.27.4: Textile Fabrics – Burning Behaviour – Determination of Ease of Ignition of Vertically Oriented Specimens, Ottawa, ON, 2000
5. International Organization for Standardization, ISO 6940 Textile Fabrics – Burning Behaviour – Determination of Ease of Ignition of Vertically Oriented Specimens, Geneva, Switzerland, 2004
6. Canadian General Standards Board, CAN/CGSB-4.2 No.27.3: Textile Fabrics – Burning Behaviour – Measurement of Flame Spread Properties of Vertically Oriented Specimens, Ottawa, ON, 2000
7. International Organization for Standardization, ISO 6941 Textile Fabrics – Burning Behaviour – Measurement of Flame Spread Properties of Vertically Oriented Specimens, Geneva, Switzerland, 2003
8. American Society for Testing and Materials, ASTM D3659-80: Standard Test Method for Flammability of Apparel Fabrics by Semi-Restraint Method, West Conshohocken, PA, 1993
9. American Society for Testing and Materials, ASTM F501-93 Test Method for Aerospace Materials Response to Flame, with Vertical Test Specimen (For Aerospace Vehicles Standard Conditions), West Conshohocken, PA, 1993
10. Canadian General Standards Board, CAN/CGSB-4.2 No.27.10-2000: Flame Resistance – Vertically Oriented Textile Fabric or Fabric Assembly Test, Ottawa, ON, 2000
11. International Organization for Standardization, ISO 9151 Protective Clothing Against Heat and Flame – Determination of Heat Transmission on Exposure to Flame, Geneva, Switzerland, 1995
12. American Society for Testing and Materials, ASTM D4108-87 Standard Test Method for Thermal Protective Performance of Materials for Clothing By Open-Flame Method, West Conshohocken, PA, 1987

13. International Organization for Standardization, ISO 6942 Protective Clothing – Protection against Heat and Fire – Method of Test: Evaluation of Materials and Material Assemblies when Exposed to a Source of Radiant Heat, Geneva, Switzerland, 2002
14. American Society for Testing and Materials, ASTM F1939-99a Standard Test Method for Radiant Protective Performance of Flame Resistant Clothing Materials, West Conshohocken, PA, 1999
15. Tortora, Gerard J., Principles of Human Anatomy, 9th Ed., John Wiley & Sons, Inc., Toronto, 2002.
16. Diller, K., “Analysis of Skin Burns” in Heat Transfer in Medicine and Biology, Shitzer, A. and Eberhart, R.C., Eds., Plenum Press, New York, 1985, pp. 85-134
17. Stoll, A.M., and Greene, L.C., “Relationship Between Pain and Tissue Damage Due to Thermal Radiation”, Journal of Applied Physiology, Vol. 14, 1959, pp. 373-382
18. Stoll, A.M., and Chianta, M.A., “Method and Rating System for Evaluation of Thermal Protection” Aerospace Medicine, Vol. 40, 1969, pp. 1232-1238
19. Henriques, F.C., Jr. and Moritz, A.R., “Studies of Thermal Injuries II. The Relative Importance of Time and Surface Temperature in the Causation of Cutaneous Burns”, The American Journal of Pathology, Vol. 23, 1947, pp. 695-720
20. Henriques, F.C., Jr., “Studies of Thermal Injuries V. The Predictability and the Significance of Thermally Induced Rate Processes Leading to Irreversible Epidermal Injury”, Archives of Pathology, Vol. 43, 1947, pp. 489-502
21. Torvi, D.A., Dale, J.D., Ackerman, M.Y., and Crown, E.M., “A Study of New and Existing Bench Top Tests for Evaluating Fabric for Flash Fire Protective Clothing”, Performance of Protective Clothing: Sixth Volume, ASTM STP 1273, J.O. Stull and A.D. Schwope, eds., American Society of Testing and Materials, West Conshohocken, PA, 1997, pp. 108-125.
22. Dale, J.S., Crown, E.M., Ackerman, M.Y., Leung, E., and Rigakis, K.B., “Instrumented Mannequin Evaluation of Thermal Protective Clothing”, Performance of Protective Clothing: Fourth Volume, ASTM STP 1133, J.P. McBriarty and N.W. Henry, eds., American Society for Testing and Materials, West Conshohocken, PA, 1992, pp. 717-733
23. Ruff, G.A., “Microgravity Research in Spacecraft Fire Safety”, Halon Options Technical Working Conference, Albuquerque, NM, April 24-26 2001, pp. 13-22
24. National Aeronautics and Space Administration Marshall Space Flight Center, “Flammability, Odor, Offgassing, and Compatibility Requirements and Test

- Procedures for Materials in Environments That Support Combustion”, NASA-STD-6001, Huntsville, AL, 1998
25. Olson, S.L., “The Effect of Microgravity on Flame Spread Over a Thin Fuel”, NASA/TM-100195, Cleveland, OH, 1987
 26. Bhattacharjee, S., Altenkirch, R.A., and Sacksteder, K.R., “The Effect of Ambient Pressure on Flame Spread over Thin Cellulosic Fuel in a Quiescent Microgravity Environment”, Journal of Heat Transfer, Volume 118, 1996, pp. 181-190
 27. Kashiwagi, T. et al., “Ignition, Transition, Flame Spread in Multidimensional Configurations in Microgravity,” in K. Sacksteder, ed., Fifth International Microgravity Combustion Workshop, NASA/CP-1999-208917, Cleveland, OH, May 1999, pp. 333-336
 28. Ivanov, A.V. et al., “Experimental Verification of Material Flammability in Space”, NASA/CR – 1999-209405, Cleveland, OH, Nov. 1999
 29. T’ien, J. et al., “Solid Inflammability Boundary at Low-Speed (SIBAL)”, in K. Sacksteder, ed., Seventh International Workshop on Microgravity Combustion and Chemically Reacting Systems, NASA/CP-2003-212376, Cleveland, OH, June 2003, pp.121-124
 30. Kashiwagi, T. et al., “Localized Ignition and Subsequent Flame Spread Over Solid Fuels in Microgravity”, in K. Sacksteder, ed., Seventh International Workshop on Microgravity Combustion and Chemically Reacting Systems, NASA/CP-2003-212376, Cleveland, OH, June 2003, pp.125-128
 31. National Institute of Standards and Technology “NIST Fire Dynamics Simulator (FDS) and Smokeview”, <http://fire.nist.gov/fds>, accessed April 2004
 32. Sacksteder, K. et al., “Upward and Downward Flame Spreading and Extinction in Partial Gravity Environments”, in K. Sacksteder, ed., Seventh International Workshop on Microgravity Combustion and Chemically Reacting Systems, NASA/CP-2003-212376, Cleveland, OH, June 2003, pp.141-144
 33. Olson, S.L, Beeson, H., and Haas, J.P., “An Earth-Based Equivalent Low Stretch Apparatus to Assess Material Flammability for Microgravity & Extraterrestrial Fire-Safety Applications”, in K. Sacksteder, ed., Seventh International Workshop on Microgravity Combustion and Chemically Reacting Systems, NASA/CP-2003-212376, Cleveland, OH, June 2003, pp.213-216
 34. Microgravity Combustion Lab, Department of Mechanical Engineering, University of California Berkeley “Forced Ignition and Flame Spread Test (FIST)”, <http://www.me.berkeley.edu/mcl/fist>, accessed August 2003

35. American Society for Testing and Materials, ASTM E1354-04a Standard Test Method For Heat and Visible Smoke Release Rates for Materials and Products Using an Oxygen Consumption Calorimeter, West Conshohocken, PA, 2004
36. American Society for Testing Materials, ASTM E1321-97a(2002) Standard Test Method for Determining Material Ignition and Flame Spread Properties, West Conshohocken, PA, 2002
37. Fernandez-Pello, A.C. et al., “Piloted Ignition of Polypropylene/Glass Composites in a Forced Air Flow”, in K. Sacksteder, ed., Seventh International Workshop on Microgravity Combustion and Chemically Reacting Systems, NASA/CP-2003-212376, Cleveland, OH, June 2003, pp.209-212
38. Thomas, V.A., Prasad, N.S., and Ananda Mohan Reddy, C., “Microgravity Research Platforms – A Study”, Current Science, Vol. 79, No. 3, August 2000, pp. 336-340
39. Goldmeer, J., “A User’s Guide for the Spacecraft Fire Safety Facility”, NASA/TM-2000-210375, Cleveland, OH, August 2000
40. Backer, S., et al., Textile Fabric Flammability, The MIT Press, Cambridge, MA, 1976
41. Incropera and DeWitt, Fundamentals of Heat and Mass Transfer, 4th Ed., John Wiley & Sons, Inc., Toronto, 1996
42. American Society for Testing and Materials, ASTM F955-03 Standard Test Method for Evaluating Heat Transfer through Materials for Protective Clothing Upon Contact with Molten Substances, West Conshohocken, PA, 2003
43. Dale, J.D., Ackerman, M., Crown, B.M., Hess, D., Tucker, R., and Bitner, E., “A Study of Geometry Effects on Testing Single Layer Fabrics for Thermal Protection”, Performance of Protective Clothing: Issues and Priorities for the 21st Century: Seventh Volume, ASTM STP 1386, C.N. Nelson and N.W. Henry, Eds., American Society for Testing and Materials, West Conshohocken, PA, 2000
44. WireTronic, Inc. “Nichrome & Other Resistance Alloys – Technical Data & Properties”, <http://www.wiretron.com/nicrdat.html>, accessed June 2003
45. German Transport Information Service, “Cotton”, http://www.tis-gdv.de/tis_e/ware/fasern/baumwoll/baumwoll.htm, accessed June 2004
46. Canadian General Standards Board, CAN/CGSB-4.2 No.5.1-M90 Unit Mass of Fabrics, Ottawa, ON, 1997
47. Canadian General Standards Board, CAN/CGSB-4.2 No.37-2002 Fabric Thickness, Ottawa, ON, 2002

48. Torvi, D.A., "Heat Transfer in Thin Fibrous Materials under High Heat Flux Conditions", Ph.D. Thesis, University of Alberta, Edmonton, Alberta, 1997
49. "Space Station Policies, International Standards Addendum – Safety Policy Requirements for Payloads Using the International Space Station", NSTS 1700.7B (ISS Addendum), Houston, TX, December 1995
50. Beck, J.V., Blackwell, B., and St. Clair, C.R. Jr., Inverse Heat Conduction: Ill-posed Problems, John Wiley & Sons, Inc., New York, 1985
51. Diller, T.E., "Advances in Heat Flux Measurements", Advances in Heat Transfer, Vol. 23, pp. 279-283
52. Cook, W.J., and Felderman, E.J., "Reduction of Data from Thin-Film Heat-Transfer Gauges: A Concise Numerical Technique", American Institute of Aeronautics and Astronautics (A.I.A.A.) Journal, Vol. 4, 1966, pp. 561-562
53. Torvi, D.A., "A Finite Element Model of Heat Transfer in Skin Subjected to a Flash Fire", M.Sc. Thesis, University of Alberta, Edmonton, Alberta, 1992
54. Pennes, H.H., "Analysis of Tissue and Arterial Blood Temperatures in Resting Human Forearm", Journal of Applied Physiology, Vol. 1, 1948, pp. 93-122
55. Drysdale, D., An Introduction to Fire Dynamics, 2nd Ed., John Wiley & Sons, Inc., Toronto, 1998
56. Nazare, S., Kandola, B., and Horrocks, A.R., "Use of Cone Calorimetry to Quantify the Burning Hazard of Apparel Fabrics", Fire and Materials, Vol. 26, 2002, pp. 191-199.
57. Drysdale, D.D., and Macmillan, A.J.R., "Flame Spread on Inclined Surfaces", Fire Safety Journal, Vol. 18, 1992, pp. 245-254.
58. Sensors® Online "Quest for Fire Control: Using Heat Flux Sensors to Determine Fire Safety", <http://www.sensorsmag.com/articles/1003/37/main.shtml>, accessed October 2003
59. Government of Alberta Department of Human Resources and Employment "Workplace Health and Safety Bulletin – Appropriate Workwear for Flash Fire and Explosion Hazards", <http://www3.gov.ab.ca/hre/whs/publication/pdf/ppe005.pdf>, accessed June 2004
60. Cengel, Y.A., and Turner, R.H., Fundamentals of Thermal-Fluid Sciences, McGraw-Hill, Toronto, 2001

APPENDICES

APPENDIX A EXPERIMENTAL PROCEDURE FOR MICROGRAVITY TESTING

This Appendix contains the procedure developed and followed for the KC-135 low gravity flight to obtain the microgravity data for this experiment.

SKIN DAMAGE OPERATING PROCEDURE

The following pre-flight check is to be done prior to each flight.

PRE-FLIGHT CHECK

- a) Verify that the chamber is free of debris
- b) Verify that the vent openings are free of debris
- c) Verify that a sample card is installed in the chamber. If not, install a sample using the "INSTALL SAMPLE" procedure (Step 37).
- d) Pull the chamber release pin and close the chamber lid. Lift up on the lid and slide lid restraint to the right.
- e) Secure the V-band clamp
- f) Verify that the V-Band is torqued to 50-60 in-lbs
- g) Verify that the Pressure Equalization Valve (green handle) is closed
- h) Verify that the 28 VDC and 120 VAC cables are connected to the aircraft power lines
- i) Verify that the vent line is attached to the aircraft overboard vent
- j) Verify that the oxidizer gas is connected to MFC2.
- k) Verify that the gas bottles are connected tightly and the bottle valves are closed
- l) Verify that the black curtains are in place
- m) Verify that the main panel switches are all turned to the de-energized or off positions
- n) Verify that the settings on the time code generator is set to the pre-set positions as indicated by the "red dot".
- o) Verify that the time code generators are switched to the **OFF** position
- p) Verify that the Horita SCT-50 Titlers are **OFF**
- q) Verify that the AC power adapter cable is plugged into the laptop
- r) Verify that a new MiniDV tape is installed in the COLOR and IR DVCAM recorder and is labeled with the camera type and flight date
- s) Verify that the lens cap is on the IR camera
- t) Verify that the IR camera cable is connected to the IR control computer, the IR power cable is connected to a 120 VAC power source, and that the keyboard on the IR control computer is properly stowed
- u) Verify that the samples stowage box and stowage bag are aboard
- v) Verify that there are spare MiniDV tapes in the stowage bag

END OF PRE-FLIGHT CHECK

POWER UP THE FACILITY

- (1) **Power up the Facility**
 - a) Set the main power switch to the **ON** position
 - b) Set the 110 VAC Aux. switch to the **ON** position
 - c) Set the Computer power switch to the **ON** position
 - d) Set the 28 VDC switch to the **ON** position
 - e) Set the camera switch to the **ON** position
 - f) Set the SAMs power switch to the **ON** position
 - g) Verify that the PID controller is in Auto mode (displays the mnemonic "SP")
 - h) Turn right HORITA SCT-50 Titler switch to **ON** (as viewed from the front of the SFSF)
 - i) Turn **ON** the right three time code generators (as viewed from the front of the SFSF)
 - j) Turn **ON** the *COLOR* and IR DVCAM recorder
 - k) Turn the laptop power on and wait for the computer to boot to Windows
 - l) Turn on the IR camera by pressing the **ON** corner of the triangular toggle switch on the IR camera head.
 - m) Release the keyboard on the IR camera control computer by pressing the two green buttons on top of the computer. Secure it in the down position.
 - n) Turn **ON** the IR camera control computer (on back)
 - o) **Verify/Set** the time and date on the computer.
 - p) **Select** the "*SKIN*" shortcut on the desktop to open the DACS program
 - q) **Click** on the arrow symbol on the upper left of the laptop screen to start the DACS program.
 - r) **Change the name of the data file**, if desired.
 - s) Press "**Save**"
 - t) Set the igniter power switch to the **AUTO** (UP) position
 - u) Set the three solenoid control switches (Inlet, Vent 1, & Vent 2) to the **AUTO** (UP) position
 - v) Depress the BLACK reset button (*red LED will turn on*)
- (2) **Set** pressure regulator to zero and open the K-bottle
- (3) **Set** the pressure regulator on the K-bottle to 60 PSIG
- (4) Wait for a color image to appear on the IR DVCAM recorder
- (5) Select the **Tracer** shortcut icon on the Windows desktop.
- (6) Verify that camera serial number 550027 is selected.
- (7) Select the **Real Time** menu item and then **Display** in the drop down menu.
- (8) Select **Camera Control** and, in the window, select **Range 4** and verify that the "**Film filter**" is highlighted. Select **OK**.
- (9) **Change** the upper limit to 500 deg C and select **Apply**
- (10) On IR camera head, press **AUTO** button until **AUTO LVL and AUTO LVL** disappear from screen
- (11) Press **MENU**, Select **FILTER**, and press **ENTER**.
- (12) Toggle filter to display **F FLM** on DVCAM display. **R4** (Range 4) should be displayed.
- (13) On the IR camera head, use the Gain and Level toggles to get range of 150 to 500 deg C
- (14) Press NUC (Non-Uniform Compensation) button on the IR camera head and wait 1 minute
- (15) Remove the lens cap from the IR camera

POWER UP OF THE FACILITY IS COMPLETE

RUN TEST SEQUENCE

Start Flow Sequence

- (16) **Click** on the **Purge** button in the DAC program to purge the chamber.
- (17) **Enter** the oxidizer velocity in cm/second in the Oxidizer Flow Rate box on the computer.
- (18) **Enter** the scale factors for MFC2 (in percent of N₂ flow rate)
- (19) **Enter/Verify** the desired Flow and Vent pressures (in millibars) on the laptop
- (20) **Verify** that the heat flux gauge temperature is no greater than 25 deg C. If so, allow purge flow to continue until this temperature is reached.
- (21) Wait for the **Purge** sequence to complete before continuing

Prepare IR Camera

- (22) Click the **Real Time** menu item and select the **Record Sequence** item in the drop down menu.
- (23) Browse to the **SKIN** directory and enter the same file name as on the SFSF DAQ computer
- (24) Verify the settings are 1 frame/sec and 1 minute sequence duration. If ok, go to step (26).
- (25) Click on the **Load Settings** button and browse to the settings file in the **SKIN** menu.

Fill Chamber

- (26) **Click** on the **Fill** button on the DAC computer to vent and fill the chamber
- (27) Verify that the time displayed by the Time Code Generators is zero. If not, **cycle** power on all Time Code Generator.

Start Flow

- (28) Press the Time Code Generator **Start/Stop Switch** and then verify that the TCG is running. If not, press the switch again (be sure to only press it ONE time)
- (29) During zero-g before the test parabola, press **Start Recording** on the laptop DAC program.
- (30) **Click** on the **Flow Oxidizer** button to start the flow. Wait for flow to stabilize before continuing.

Sample Ignition

- (31) Thirty (30) seconds into the pull-up before the test parabola, click **Start Recording** on the IR camera control computer
- (32) On the laptop, press **ignite** to ignite the sample (*Verify the ignitor LED is lit.*)
- (33) When ignition is confirmed, press **ignite** a second time to turn off the igniter. (*Verify that the igniter LED goes out.*)
- (34) Allow sample to burn through the entire parabola.

Vent/Purge

- (35) At the end of the parabola, press the **Vent** button to vent the chamber
- (36) Press **Stop Recording** on the laptop
- (37) When the indicator shows that the venting process has completed, verify that the chamber is vented to atmospheric pressure (less than 1000 mbar)
- (38) For **sample change**, proceed to Step (39). For **shut down**, proceed to **Power Down** procedure.

RUN TEST SEQUENCE IS COMPLETE

INSTALL SAMPLE – If sample is already installed, skip to Step (16)

(39) Install sample:

- a) Turn igniter switch on control panel to “OFF” position.
- b) **Open** Pressure Equalization Valve (green handle)
- c) Wait for the pressure to equalize.
- d) Check chamber pressure on both PID controller and differential pressure gauge
- e) ***IF THE DIFFERENTIAL PRESSURE IS OTHER THAN ZERO, do not open the chamber – verify equalization valve (green handle) is open. If differential pressure does not get to ZERO, use the hardwired KILL sequence as described in the Emergency Procedures Section (Section A.1)***
- f) Release chamber V-band clamp.
- g) While lifting up on the lid, slide the chamber lid restraint to the right and open the lid. Verify the lid is secured.
- h) Unplug the thermocouple and igniter/heater connectors.
- i) Remove sample card
- j) Verify that sample is intact. If not, clean/check for debris in chamber vents
- k) Secure used sample card.
- l) Install new sample card in the chamber
- m) Reconnect the thermocouple connectors and the igniter/heater connector.
- n) Close the chamber lid.
- o) Secure lid restraint (*lift up on chamber lid when sliding into position*)
- p) Secure chamber lid with V-Band clamp.
- q) Close the pressure equalization valve (green handle).
- r) Turn igniter switch on control panel to “AUTO” position.
- s) Clean the sample card taken from the chamber and install a new sample tray
- t) Connect the igniter pins of the new sample and stow the sample card

INSTALL SAMPLE IS COMPLETE

A.1 EMERGENCY/ABORT PROCEDURES

The system has a hardwired fail safe KILL relay system activated by a (RED) Panic Button. If an emergency situation occurs, the operator should:

1 - PRESS THE (RED) PANIC BUTTON.

Note: The KILL relay system will automatically be initiated by any of the following other events:

- Loss of power to the relay
- Loss of power to the PID controller
- An over pressure alarm from the PID controller

2 – Press Abort on the laptop

3 – Power down the rig as in section A2

4 – Correct the problem encountered

5 – Restart this procedure from Step 1 – only if problem has been corrected.

A.1.1 Loss of Communication Error

In the event the laptop loses communication with the PID controller, the re-start procedure is as follows:

- (1) Press the (**RED**) Panic Button
 - (2) Set the three solenoid control switches (Inlet, Vent 1, and Vent 2) to the “**DE-ENERGIZE**” (Center) condition
 - (3) Set the igniter to the “**OFF**” position
 - (4) Click on the “Abort” button on the laptop
 - (5) Click on the arrow in the upper left-hand corner of the computer screen.
 - (6) Click “**Save**”
 - (7) Set the three solenoid control switches (Inlet, Vent 1, and Vent 2) to the “**AUTO**” (UP) position
 - (8) Verify that pressure, temperature, and accelerometer data are being read and properly displayed. If not, execute the **Emergency/Abort** procedure described above
-

A.2 - POWER DOWN SEQUENCE

- (1) Select **Exit** from the **File** menu in LabVIEW to exit the SKIN DAQ program
- (2) Set the switches to the DVCAM recorders to the “**OFF**” position.
- (3) Verify that the power to the sample heater controller is “**OFF**”
- (4) Set the Horita SCT-50 Titrator to the “**OFF**” position
- (5) Set the 3 solenoid control switches (Inlet, Vent 1, & Vent 2) to the “**DE-ENERGIZE**” (Center) position
- (6) Set the Igniter switch to the “**OFF**” (Center) position
- (7) Set the camera switch to the “**OFF**” position.
- (8) Set the 28 VDC switch to the “**OFF**” position
- (9) Set the SAMS Power switch to the “**OFF**” position
- (10) Set the Computer power switch to the “**OFF**” position
- (11) Set the 110 VAC Aux. switch to the “**OFF**” position
- (12) Close all open windows on the IR camera computer and shutdown Windows.
- (13) Press the **OFF** corner of the Toggle on the IR Camera.
- (14) Return any tools removed during flight to the stowage bag and return bag to stowage.
- (15) Secure the sample stowage box
- (16) Close the valves on both K-bottles
- (17) Vent the both K-bottle lines

- (18) On the laptop, copy data files from the **c:\FATE** to the USB Flash memory module, if desired
- (19) On the laptop, shutdown Windows
- (20) Turn off power on laptop
- (21) Set the main power switch to the **"OFF"** position

APPENDIX B ESTIMATED HEAT FLUX CALCULATIONS

This appendix shows the calculations used to estimate the radiation, conduction, and convection heat transfer from the burning fabric to the skin in the vertical, horizontal, and flipped orientations for various surface temperatures and both air gaps.

I. Radiation

Radiation heat transfer can be estimated using the following formula:

$$q'' = F_{ij}\sigma(T_i^4 - T_j^4)$$

where F_{ij} is the view factor. It will be different for the two air gaps, but will not change with a change in orientation. For this analysis, a view factor for two aligned parallel rectangles was determined. The rectangle sizes were 190 mm by 70 mm, corresponding to the area of fabric exposed to the heat flux gauges. The view factors were determined using a Figure based on the geometry of the enclosure.

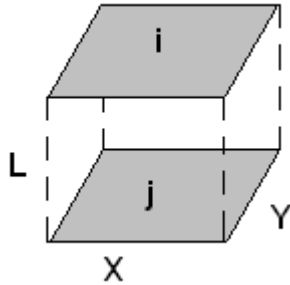


FIGURE B.1 Parallel Rectangles

Case 1 – 7 mm Air Gap

$$X = 190, Y = 70, L = 7$$

$$X/L = 27.1, Y/L = 10, \text{ giving } F_{ij} = 0.9$$

Case 2 – 13 mm Air Gap

$$X = 190, Y = 70, L = 13$$

$$X/L = 14.6, Y/L = 5.4, \text{ giving } F_{ij} = 0.8$$

Sample Calculation

Assuming a fabric surface temperature of 250°C and a sensor board temperature of 25°C, for the 7 mm air gap, the radiation heat flux can be calculated as follows:

$$q'' = F_{ij}\sigma(T_i^4 - T_j^4)$$

$$q'' = 0.9(5.67 \times 10^{-8})(523^4 - 298^4)$$

$$q'' = 3416 \text{ W/m}^2 = 3.42 \text{ kW/m}^2$$

Results

The estimated radiation heat transfer values for the various surface temperatures at both air gaps are listed in Table B.1.

TABLE B.1 Estimated Radiation Heat Flux

AIR GAP	Radiation Heat Flux (kW/m ²)			
	250°C	300°C	350°C	400°C
7 mm	3.42	5.10	7.28	10.1
13 mm	3.04	4.53	6.48	8.95

Radiation in Microgravity

In microgravity, the flame size decreases substantially, so a new view factor to better represent this was calculated. Parallel disks were used, with one disk 22 mm in diameter representing the flame size and the second disk being either 22 mm or 40 mm in diameter to represent either the skin simulant or the copper disk.

The view factor is calculated as follows:

$$F_{1 \rightarrow 2} = \frac{1}{2} \left\{ X - \left[X^2 - 4 \left(\frac{R_2}{R_1} \right)^2 \right]^{1/2} \right\}$$

where $R = \frac{r}{L}$ and $X = 1 + \frac{(1 + R_2^2)}{R_1^2}$

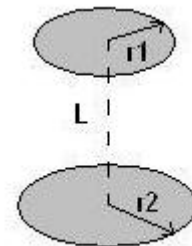


FIGURE B.2 Parallel Disks

The resulting view factors for the 7 mm air gap to disks of 22 mm and 40 mm respectively are 0.53 and 0.86 respectively. For the 13 mm air gaps the view factors are 0.33 and 0.65 to the 22 mm and 40 mm disks respectively. The resulting radiation heat transfer values are in Table B.2 below.

TABLE B.2 Radiation Heat Flux Estimated for Microgravity

Radius, r1 (mm)	Radius, r2 (mm)	Air Gap, L (mm)	Radiation Heat Flux (kW/m ²)			
			250°C	300°C	350°C	400°C
11	20	7	3.3	4.9	7.0	9.6
11	20	13	2.5	3.7	5.3	7.3
11	11	7	2.0	3.0	4.3	5.9
11	11	13	1.3	1.9	2.7	3.7

II. Conduction and Convection

By knowing the orientation, the dimensions of the enclosure, and the calculated Raleigh number, an appropriate correlation for the Nusselt number can be chosen. Once the Nusselt number is determined, the corresponding h value can be found. Knowing h, the heat transfer can be calculated. The correlations used for determining the Nusselt number were taken from Reference [60].

General Equations

Raleigh number:
$$Ra = \frac{g\beta\Delta T\delta^3}{\alpha\nu}$$

Nusselt number:
$$Nu = \frac{hL}{k}$$

Heat Flux:
$$q'' = h(T_1 - T_2)$$

Horizontal Orientation

In the horizontal orientation, the fabric is positioned above the heat flux gauges. This creates a stable situation in which the top surface is the hot surface and the bottom surface is the cold surface. In such a situation, no convection currents will develop in the enclosure since the lighter fluid will always be on top of the heavier fluid. Heat transfer is by pure conduction and $Nu=1$.

Flipped Orientation

In the flipped orientation, the fabric is positioned beneath the heat flux gauges. The hot surface is now on the bottom and the cold surface on top. This creates an unstable situation in which convection currents may possibly develop. For air in such an enclosure, convection currents are likely to develop if $Ra>1700$. At the 7 mm air gap, the Raleigh numbers were all less than the critical value of 1700, indicating that the heat transfer is by conduction as for the horizontal orientation and $Nu=1$. At the 13 mm air gap, Raleigh numbers were found to be between about 8300 and 11000. This range of Raleigh numbers calls for the following Nusselt number correlation:

$$Nu = 0.212Ra^{1/4}$$

Vertical Orientation

The vertical orientation also produces an unstable situation in which convection currents may develop. In this case the convection currents are likely to develop if $Ra>2000$. As Raleigh numbers are not dependant on orientation, again at the 7 mm air gap they are all less than the critical value of 2000, indicating no convective heat transfer and that $Nu=1$. At the 13 mm air gap, the Raleigh number range of 8300 to 11000 corresponds to the following correlation:

$$Nu = 0.197Ra^{1/4} \left(\frac{H}{\delta} \right)^{-1/9}$$

Note that the vertical correlation involves dimensions of the enclosure. H is the height of the enclosure and δ is the width, or in this case the air gap size.

Sample Calculations

The following calculations are done for a fabric surface temperature of 250°C at the 13 mm air gap. An ambient temperature of 25°C was assumed.

$$Ra = \frac{g\beta\Delta T\delta^3}{\alpha\nu}$$

$$Ra = \frac{9.81\left(\frac{1}{410.5}\right)(250-25)(0.013)^3}{(40.17\times 10^{-6})(27.67\times 10^{-6})}$$

$$Ra = 10628$$

Horizontal orientation:

$$Nu = 1$$

$$h = \frac{Nuk}{L}$$

$$h = \frac{(1)(34.54\times 10^{-3})}{0.013}$$

$$h = 2.66$$

$$q'' = h(T_1 - T_2)$$

$$q'' = 2.66(250 - 25)$$

$$q'' = 599 \text{ W/m}^2 = 0.60 \text{ kW/m}^2$$

Flipped orientation:

$$Nu = 0.212Ra^{1/4}$$

$$Nu = 0.212(10628)^{1/4}$$

$$Nu = 2.15$$

$$h = \frac{Nuk}{L}$$

$$h = \frac{(2.15)(34.54 \times 10^{-3})}{0.013}$$

$$h = 5.71$$

$$q'' = h(T_1 - T_2)$$

$$q'' = 5.71(250 - 25)$$

$$q'' = 1285 \text{ W/m}^2 = 1.29 \text{ kW/m}^2$$

Vertical orientation:

$$Nu = 0.197 Ra^{1/4} \left(\frac{H}{\delta} \right)^{-1/9}$$

$$Nu = 0.197(10628)^{1/4} \left(\frac{245}{13} \right)^{-1/9}$$

$$Nu = 1.44$$

$$h = \frac{Nuk}{L}$$

$$h = \frac{(1.44)(34.54 \times 10^{-3})}{0.013}$$

$$h = 3.83$$

$$q'' = h(T_1 - T_2)$$

$$q'' = 3.83(250 - 25)$$

$$q'' = 862 \text{ W/m}^2 = 0.86 \text{ kW/m}^2$$

Results

The following table summarizes the conduction and convection heat flux estimated for the various conditions.

TABLE B.3 Estimated Conduction and Convection Heat Transfer

AIR GAP & ORIENTATION	Heat Flux (kW/m ²)			
	250°C	300°C	350°C	400°C
7 mm – Flipped, Vertical, and Horizontal	1.11	1.43	1.76	2.13
13 mm FLIPPED	1.29	1.63	1.97	2.32
13 mm VERTICAL	0.86	1.09	1.32	1.56
13 mm HORIZONTAL	0.60	0.77	0.95	1.15

Critical Air Gap Size

The size of air gap that transition from conduction to convection is predicted to occur can be calculated by setting the Raleigh number equal to the critical value and solving for the spacing. The critical Raleigh numbers for the vertical and flipped orientations are 2000 and 1700 respectively. Again, the critical spacing will depend on the surface temperature of the fabric. A sample calculation is shown for the vertical orientation assuming a hot temperature of 300°C and a cold temperature of 25°C.

$$Ra = \frac{g\beta\Delta T\delta^3}{\alpha\nu}$$

$$2000 = \frac{9.81\left(\frac{1}{435.5}\right)(300-25)\delta^3}{(44.62 \times 10^{-6})(30.66 \times 10^{-6})}$$

$$\delta = 7.6 \text{ mm}$$

The following table shows the critical air gap for transition from conduction to convection to occur for the vertical and flipped orientation (recall the horizontal orientation only has conductive heat transfer). All values are just over 7 mm, indicating transition likely occurs between the 7 mm and 13 mm air gaps.

TABLE B.4 Critical Air Gap for Transition from Conduction to Convection

ORIENTATION	CRITICAL AIR GAP (mm)			
	250°C	300°C	350°C	400°C
Vertical	7.5	7.6	7.8	8.1
Flipped	7.1	7.2	7.4	7.6

APPENDIX C SKIN BURN INJURY PREDICTIONS

This Appendix contains Figures of average predicted times to second and third degree burns. The first group of plots shows predicted second degree burn times for each fabric at each air gap, with the data for vertical, horizontal and flipped orientations on each plot. The second group of plots is identical, but for predicted third degree burn times. The final group of plots shows second degree predicted burn times for each orientation at the 13 mm air gap. A word of caution when viewing these plots is that a predicted burn time plotted at zero seconds actually means no burn was predicted.

I. Second Degree Burn Times at the 7 mm Air Gap

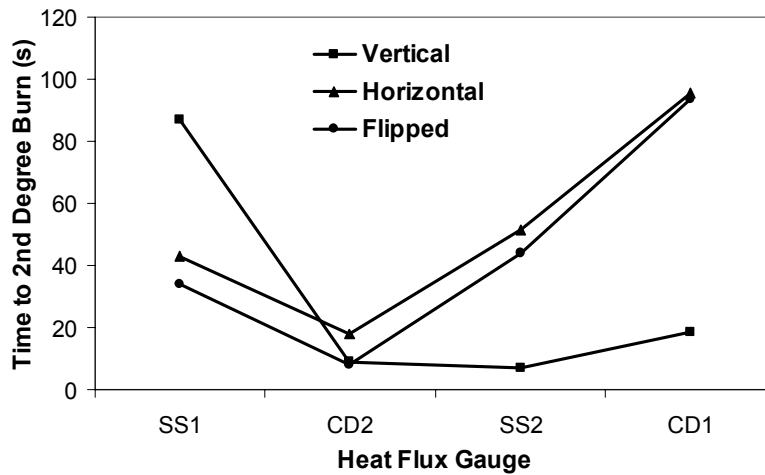


FIGURE C.1a Lightweight Cotton Second Degree Burn Times at the 7 mm Air Gap

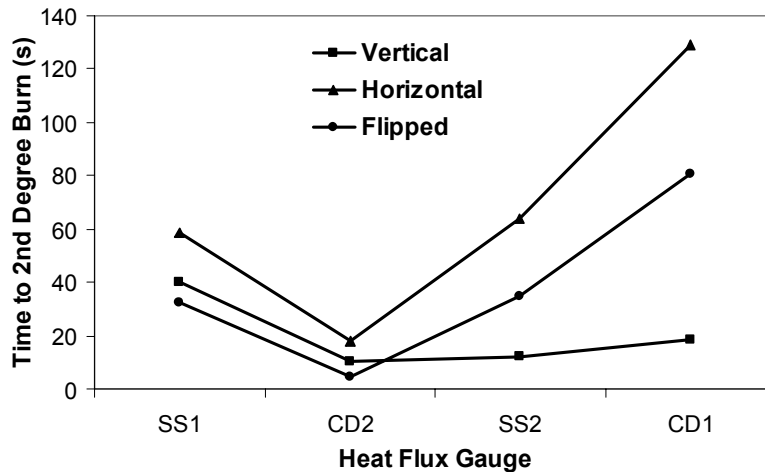


FIGURE C.1b Heavyweight Cotton Second Degree Burn Times at the 7 mm Air Gap

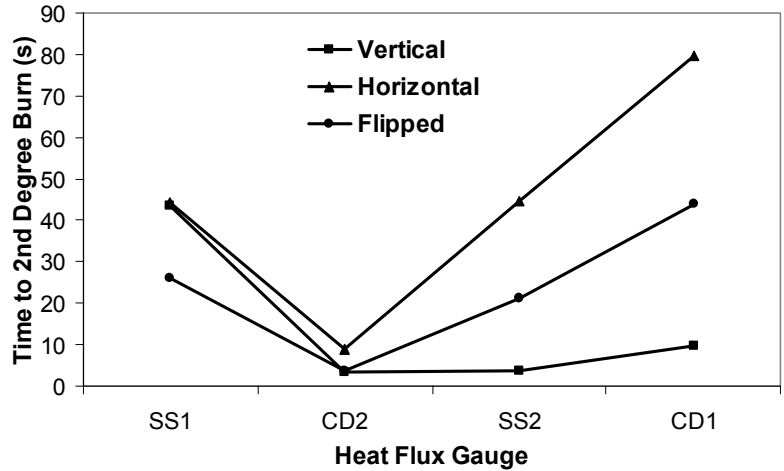


FIGURE C.1c Lightweight Blend Second Degree Burn Times at the 7 mm Air Gap

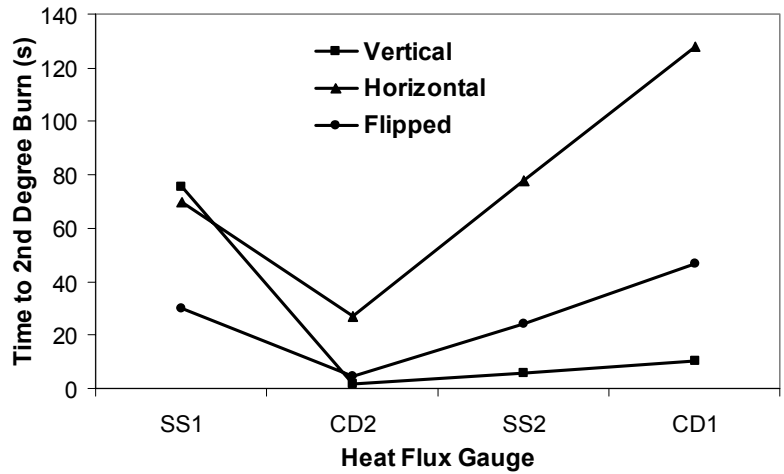


FIGURE C.1d Heavyweight Blend Second Degree Burn Times at the 7 mm Air Gap

II. Second Degree Burn Times at the 13 mm Air Gap

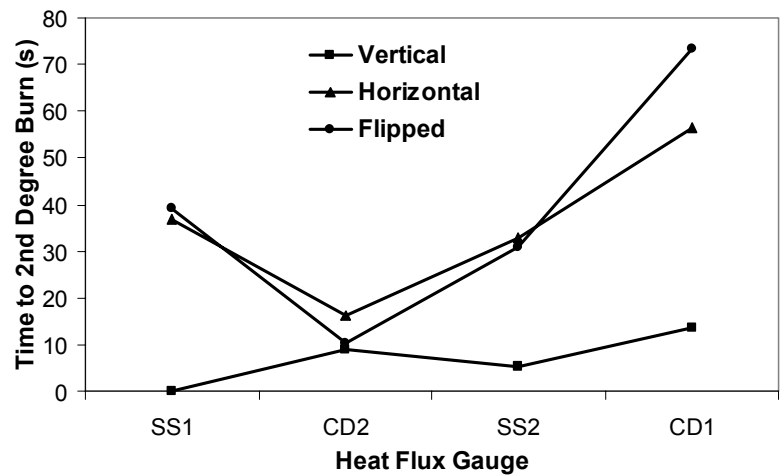


FIGURE C.2a Lightweight Cotton Second Degree Burn Times at the 13 mm Air Gap

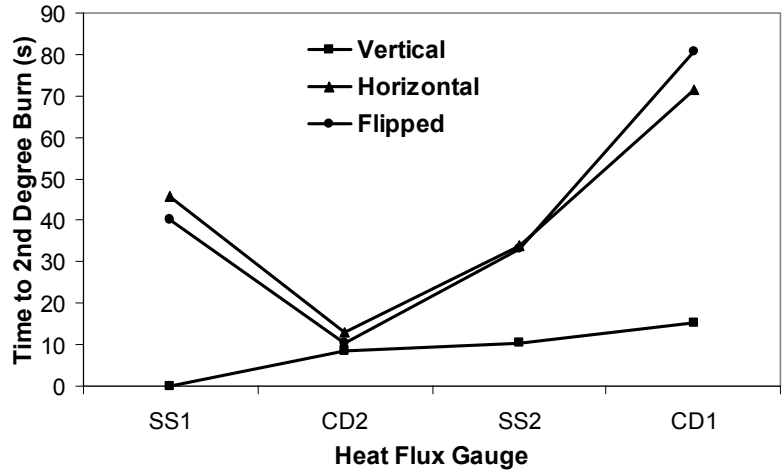


FIGURE C.2b Heavyweight Cotton Second Degree Burn Times at the 13 mm Air Gap

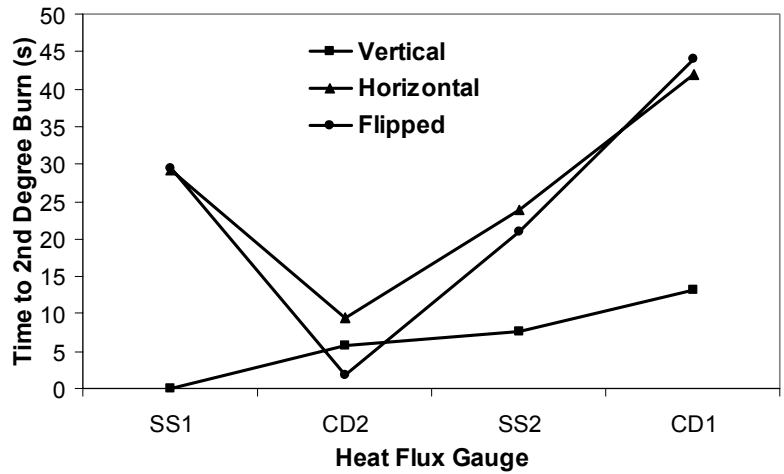


FIGURE C.2c Lightweight Blend Second Degree Burn Times at the 13 mm Air Gap

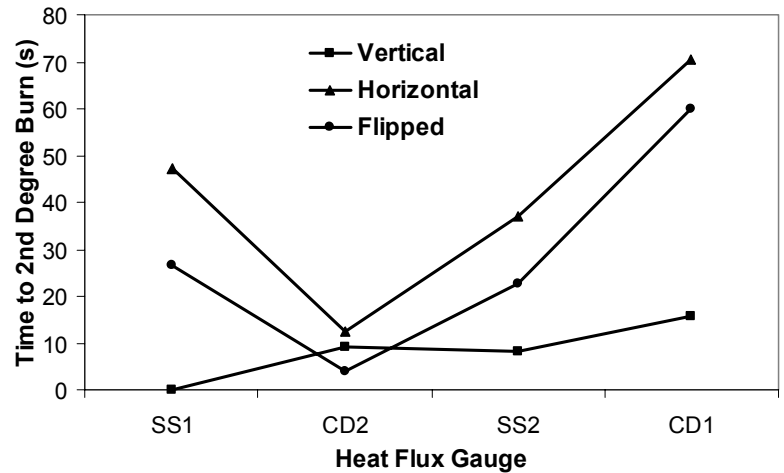


FIGURE C.2d Heavyweight Blend Second Degree Burn Times at the 13 mm Air Gap

III. Third Degree Burn Times at the 7 mm Air Gap

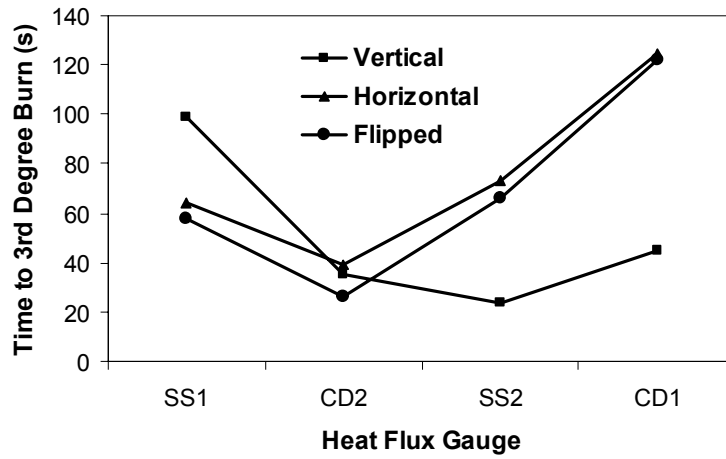


FIGURE C.3a Lightweight Cotton Third Degree Burn Times at the 7 mm Air Gap

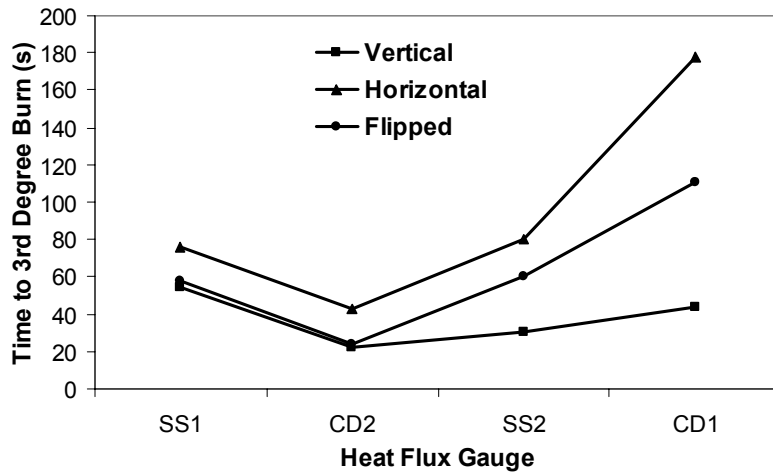


FIGURE C.3b Heavyweight Cotton Third Degree Burn Times at the 7 mm Air Gap

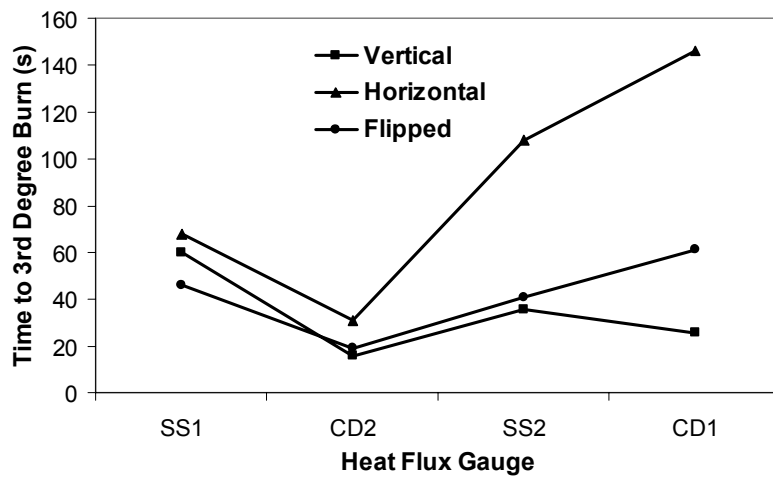


FIGURE C.3c Lightweight Blend Third Degree Burn Times at the 7 mm Air Gap

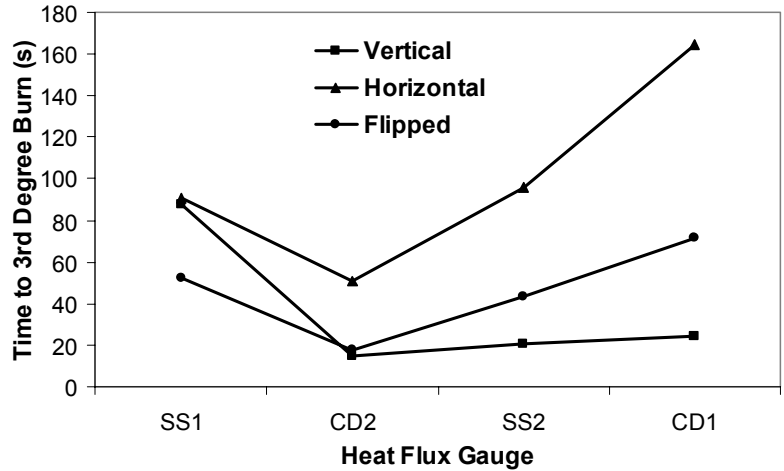


FIGURE C.3d Heavyweight Blend Third Degree Burn Times at the 7 mm Air Gap

IV. Third Degree Burn Times at the 13 mm Air Gap

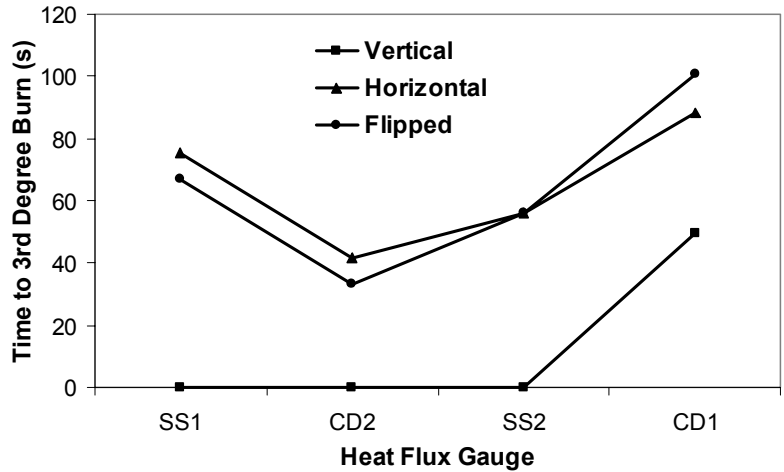


FIGURE C.4a Lightweight Cotton Third Degree Burn Times at the 13 mm Air Gap

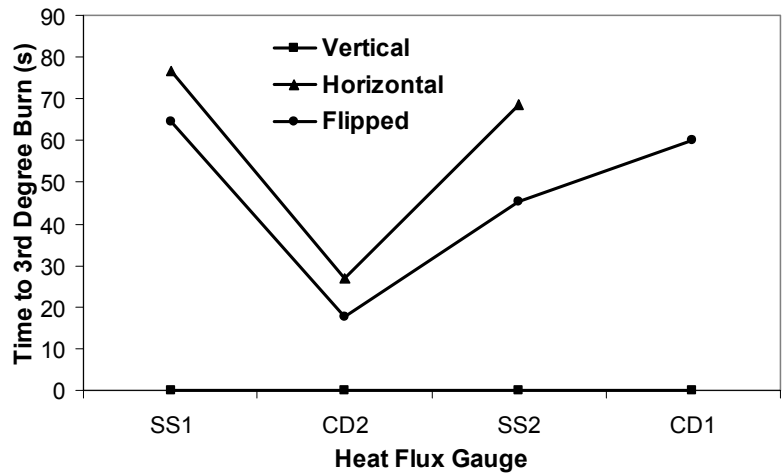


FIGURE C.4b Heavyweight Cotton Third Degree Burn Times at the 13 mm Air Gap

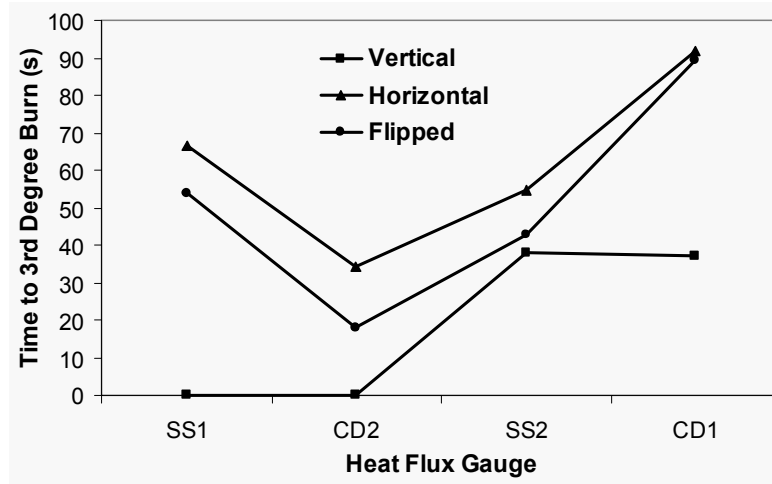


FIGURE C.4c Lightweight Blend Third Degree Burn Times at the 13 mm Air Gap

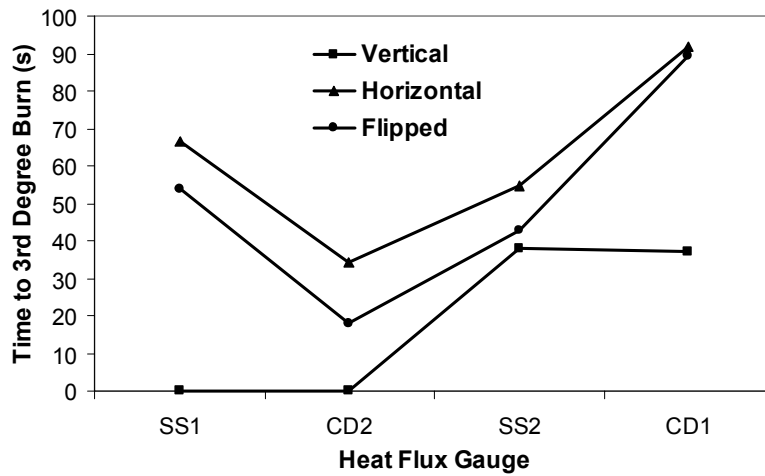


FIGURE C.4d Heavyweight Blend Third Degree Burn Times at the 13 mm Air Gap

V. Second Degree Burn Times at Each Orientation at the 13 mm Air Gap

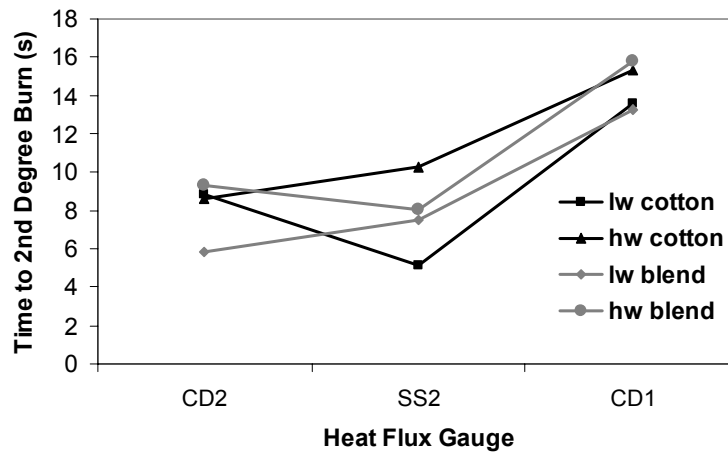


FIGURE C.5a Second Degree Burn Times for All Fabrics in the Vertical Orientation at the 13 mm Air Gap

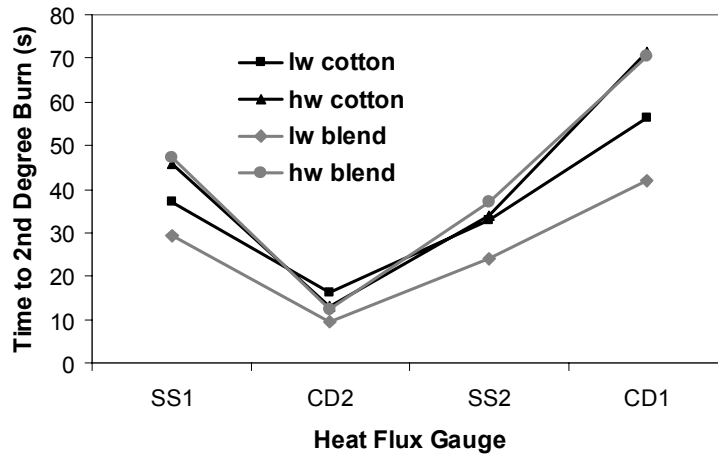


FIGURE C.5b Second Degree Burn Times for All Fabrics in the Horizontal Orientation at the 13 mm Air Gap

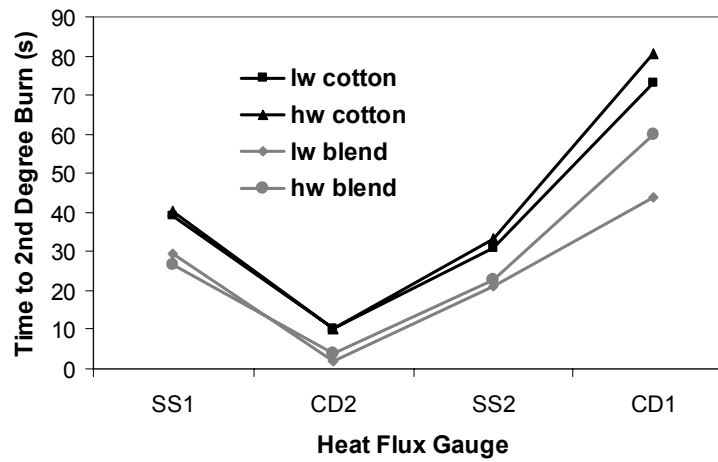


FIGURE C.5c Second Degree Burn Times for All Fabrics in the Flipped Orientation at the 13 mm Air Gap